Title

Dynamics of Satellites in Binary Near-Earth Asteroid Systems: A Study Based on Radar Observations

Permalink

https://escholarship.org/uc/item/7m63r23g

Author

Naidu, Shantanu

Publication Date

2015

Peer reviewed|Thesis/dissertation

UNIVERSITY OF CALIFORNIA

Los Angeles

Dynamics of Satellites in Binary Near-Earth Asteroid Systems: A Study Based on Radar Observations

A dissertation submitted in partial satisfaction

of the requirements for the degree

Doctor of Philosophy in Geophysics and Space Physics

by

Shantanu Naidu

2015

Abstract of the Dissertation

Dynamics of Satellites in Binary Near-Earth Asteroid Systems: A Study Based on Radar Observations

by

Shantanu Naidu

Doctor of Philosophy in Geophysics and Space Physics

University of California, Los Angeles, 2015

Professor Jean-Luc Margot, Chair

In the past 15 years, three previously unrecognized sub-populations of near-Earth asteroids (NEAs) have been discovered. About 15% of NEAs are binaries, at least 10% of NEAs are contact binaries, and dozens of asteroid pairs have been identified. Numerous science questions have arisen about the formation and evolution processes of these systems and about the inter-relationships between these groups. Addressing these questions informs us about a wide range of important solar system processes that shape small bodies and planetesimals. Here I have chosen to focus on providing one of the most complete characterizations of a binary system among all known asteroid binaries, and on studying the spin-orbit interactions in this and 8 additional binary systems. One hypothesis that has not been fully explored is the possibility of chaotic rotation of asteroid satellites and the impact that such a state has on the evolution of the binary systems. I examine this problem as well as the possibility of detecting librational motions in synchronous satellites. Because the Arecibo and Goldstone radar systems enable superb characterizations of binaries and NEAs in general, this dissertation makes abundant use of radar data. Radar observations provide images of asteroids at decameter resolution, and these images can be inverted to determine the 3D shapes of the components, which are essential to properly model the system dynamics. Radar data also enable precise determination of the mutual orbit, which is another crucial ingredient. In the first two chapters of the dissertation, I describe the observations and physical characterizations of asteroid 2000 ET70 and binary asteroid 2000 DP107. The characterization of 2000

DP107 includes size, shape, spin, mass, and density of each component, making this binary one of the best-characterized asteroid binary to date. In the last chapter of the dissertation, I describe a computationally efficient fourth-order numerical integrator that I used to investigate the coupled spin and orbital dynamics of the satellites of NEAs. The speed of the integrator enabled multi-year timescale simulations of 9 well-characterized binary near-Earth asteroids. The numerical simulations illuminate a range of rotational regimes for asteroid satellites and the conditions under which the various regimes prevail. One of the rotational regimes is chaotic, and I find that this rotation state can substantially delay the radiative evolution of binary systems.

The dissertation of Shantanu Naidu is approved.

Michael Fitzgerald

Jonathan Mitchell

David Jewitt

Jean-Luc Margot, Committee Chair

University of California, Los Angeles

2015

Dedicated to my parents, Poonam and Purushottam Naidu.

TABLE OF CONTENTS

List of Figures

Acknowledgments

I thank everyone who supported me during my PhD and made this work possible. First and foremost, I would like to express my deepest gratitude towards my PhD advisor, Jean-Luc Margot. He gave me the opportunity to work on these great projects, created a stress-free work environment, and provided excellent guidance throughout my PhD. I will always have fond memories from our numerous group activities which included hiking near Santa Barbara, a field trip in the Owens valley and Yosemite National Park, white water rafting in Oregon, and snorkeling (and stepping on sea urchins) in Puerto Rico.

Chapter 1 of this dissertation is a reprint of a peer-reviewed publication of which I am the lead author. It is reproduced under the terms of the Creative Commons Attribution License. Chapter 2 is in preparation to be submitted to a journal and Chapter 3 is a version

of a peer-reviewed paper accepted for publication in The Astronomical Journal. I am the first author of this paper and it has been reproduced by permission of the AAS. Authors and bibliographic information are provided at the beginning of each chapter.

Vita

2007	B.E. (Electronics), Mumbai University.
2009	M.S. (Telecommunications), University of Maryland, College Park.
2012	M.S. (Geophysics and Space Physics), University of California, Los Angeles

Publications

Naidu, S. P., Margot, J. L.,"Near-Earth asteroid satellite spins under spin-orbit coupling", 2015, Astronomical Journal, in press

Naidu, S. P., Margot, J. L., Busch, M. W., Taylor, P. A., Nolan, M. C., Brozovic, M., Benner, L. A. M., Giorgini, J. D., Magri, C., "Radar imaging and physical characterization of near-Earth asteroid (162421) 2000 ET70", 2013, Icarus, 226, 323

Mouawad, N., Burger, M. H., Killen, R. M., Potter, A. E., McClintock, W. E., Vervack, R. J., Bradley, E. T., Benna, M., Naidu, S. P., "Constraints on Mercury's Na exosphere: Combined MESSENGER and ground-based data", 2011, Icarus, 211, 21

Killen, R. M., Potter, A. E., Hurley, D. M., Plymate, C., Naidu, S. P., "Observations of the lunar impact plume from the LCROSS event", 2010, Geophysical Research Letter, 37, L23201.

INTRODUCTION

This dissertation includes three chapters. Each chapter is a reproduction of a peer-reviewed journal publication. The first and third chapters have been accepted for publication. The second chapter is still in preparation for future submission. The chapters describe, in order, how radar observations can be used to characterize the physical and dynamical properties of near-Earth asteroids (NEAs), how they can be used to study binary systems, and how the knowledge obtained with radar observations can be used to elucidate the spin-orbit dynamics and evolution of binary NEAs.

Chapter 1 describes in detail the process of radar observation and physical characterization of NEAs. This process is applied to a specific asteroid, 2000 ET70. We obtained continuous wave spectra and radar images with range resolutions as fine as 15 m using Arecibo and Goldstone over a period of 12 days during the asteroid's close approach to the Earth in February 2012. We inverted the radar images to obtain a detailed shape model with an effective spatial resolution of 100 m. The asteroid has overall dimension of $2.6 \times 2.2 \times 2.1$ km and spins with a period of 8.96 hours. It has two approximately parallel ridges ridges at the north pole that enclose a valley which may contain ponded fine-grained regolith material. The size, combined with the absolute magnitude measurement, yields an albedo of $\sim 2\%$. The methods described for physical characterization of 2000 ET70 are applicable to other asteroid radar datasets as well.

In Chapter 2, I describe radar observations and physical characterization of binary NEAs. The chapter focuses specifically on binary NEA 2000 DP107. The shapes of the two components were modeled using a method similar to that described in Chapter 1. The primary has a spheroidal shape with an equivalent radius of about 435 m. It has a mass of 5.1×10^{11} kg and a density of 1500 kg m^{-3}. It exhibits an equatorial ridge similar to other fast spinning asteroids such as the primary of 1999 KW4, however the equatorial ridge in this case is not as regular and has a large concavity (~ 300 m diameter) on one side. The mutual orbit has an eccentricity of about 0.015, a period of about 1.76 days, and a semi-major axis of 2.74 km. The secondary is slightly elongated and has overall dimensions of $377 \times 314 \times 268$ m. Its

mass is about 0.20×10^{11} kg and its density is about 1100 kg m^{-3}.

In Chapter 3, I investigate questions related to the spin-orbit dynamics and evolution of binary NEAs. The dynamics are dominated by exchange of angular momentum between the mutual orbit and the spins of the components, which can only be studied with knowledge of the shapes and masses of the components, as derived in Chapter 2 and other radar investigations. I describe our implementation of a fourth-order numerical integrator to simulate the coupled spin and orbital motions of two rigid bodies having arbitrary mass distributions. Using this integrator, I simulate the dynamics of components in well-characterized binary and triple near-Earth asteroid systems and use surface of section plots to map the possible spin configurations of the satellites. For asynchronous satellites, the analysis reveals large regions of phase space where the spin state of the satellite is chaotic. For synchronous satellites, I show that libration amplitudes can reach detectable values even for moderately elongated shapes. The presence of chaotic regions in the phase space has important consequences for the evolution of binary asteroids. It may substantially increase spin synchronization timescales, explain the observed fraction of asynchronous binaries, delay BYORP-type evolution, and extend the lifetime of binaries. The variations in spin rate due to large librations also affect the analysis and interpretation of lightcurve and radar observations.

CHAPTER 1

Radar Imaging and Physical Characterization of Near-Earth Asteroid (162421) 2000 ET70

1.1   Introduction

Radar astronomy is arguably the most powerful Earth-based technique for characterizing the physical properties of near-Earth asteroids (NEAs). Radar observations routinely provide images with decameter spatial resolution. These images can be used to obtain accurate astrometry, model shapes, measure near-surface radar scattering properties, and investigate many other physical properties (e.g. sizes, spin states, masses, densities). Radar observations have led to the discovery of asteroids exhibiting non-principal axis rotation (e.g., Ostro et al., 1995; Benner et al., 2002), binary and triple NEAs (e.g., Margot et al., 2002; Ostro et al., 2006; Shepard et al., 2006; Nolan et al., 2008; Brozović et al., 2011), and contact binary asteroids (e.g., Hudson and Ostro, 1994; Benner et al., 2006; Brozovic et al., 2010). Radar-derived shapes and spins have been used to investigate various physical processes (Yarkovsky, YORP, BYORP, tides, librations, precession, etc.) that are important to the evolution of NEAs (e.g., Chesley et al., 2003; Nugent et al., 2012; Lowry et al., 2007; Taylor et al., 2007; Ostro et al., 2006; Scheeres et al., 2006; Taylor and Margot, 2011; Fang et al., 2011; Fang and Margot, 2012).

Here we present the radar observations and detailed physical characterization of NEA

(162421) 2000 ET70. This Aten asteroid (a=0.947 AU, e=0.124, i=22.3°) was discovered on March 8, 2000 by the Lincoln Near-Earth Asteroid Research (LINEAR) program in Socorro, New Mexico. Its absolute magnitude was reported to be 18.2 (Whiteley, 2001) which, for typical optical albedos between 0.4 and 0.04, suggests a diameter between 0.5 and 1.5 km. Recent analysis of the astrophotometry yields absolute magnitude values that are comparable (Williams, 2012). Alvarez et al. (2012) obtained a lightcurve of the asteroid during its close approach to the Earth in February 2012. They reported a lightcurve period of 8.947 ± 0.001 hours and a lightcurve amplitude of 0.60 ± 0.07. Using visible photometry, Whiteley (2001) classified 2000 ET70 as an X-type asteroid in the Tholen (1984) taxonomy. The Tholen X class is a degenerate group of asteroids consisting of E, M, and P classes, which are distinguished by albedo. Mike Hicks (personal communication) used visible spectroscopy and indicated that his observations best matched a C-type or possibly an E-type. Using spectral observations covering a wavelength range of 0.8 to 2.5 μm in addition to the visible data, Ellen Howell (personal communication) classified it as Xk in the taxonomic system of Bus-DeMeo (DeMeo et al., 2009).

1.2 Observations and data processing

We observed 2000 ET70 from February 12, 2012 to February 17, 2012 using the Arecibo S-band (2380 MHz, 13 cm) radar and from February 15, 2012 to February 23, 2012 using the Goldstone X-band (8560 MHz, 3.5 cm) radar. The asteroid moved ∼74 degrees across the sky during this time and it came closest to Earth on February 19 at a distance of ∼0.045 Astronomical Units (AU). We observed it again in August 2012 when it made another close approach to Earth at a distance of ∼0.15 AU.

Radar observing involved transmitting a radio wave for approximately the round-trip light-time (RTT) to the asteroid, ∼46 seconds at closest approach, and then receiving the echo reflected back from the target for a comparable duration. Each transmit-receive cycle is called a *run*. On each day we carried out runs with a monochromatic continuous wave (CW) to obtain Doppler spectra, followed by runs with a modulated carrier to obtain range-Doppler

4

Table 1.1.   2000 ET70 Radar Observations Log

Tel	UT Date yyyy-mm-dd	MJD	Eph	RTT (s)	PTX (kW)	δr (m)	δf (Hz)	N	Start-Stop hh:mm:ss-hh:mm:ss	Runs	Fig. 1.8 key
A	2012-02-12	55969	s41	67	828	cw	0.167	none	08:27:51-08:37:55	5	
			s41			15	0.075	65535	08:42:47-10:29:47	48	1-7
			s41			15	0.075	8191	10:53:18-11:09:55	8	
A	2012-02-13	55970	s41	62	860	cw	0.182	none	08:11:06-08:23:08	6	
			s43			15	0.075	65535	08:30:34-10:53:26	54	8-14
A	2012-02-14	55971	s43	58	811	cw	0.196	none	07:59:56-08:04:43	3	
			s43			15	0.075	65535	08:06:40-10:19:45	59	15-22
A	2012-02-15	55972	s43	54	785	cw	0.213	none	07:43:02-07:47:29	3	
			s43			15	0.075	65535	08:03:01-08:09:18	4	
			s47			15	0.075	65535	08:16:38-10:09:46	60	23-29
G	2012-02-15	55972	s43	54	420	cw		none	08:55:15-09:03:27	5	
			s43			75	1.532	255	09:17:48-09:33:20	9	
			s45			37.5		255	09:46:24-11:59:24	73	
			s45			37.5		255	12:15:57-12:24:09	5	
A	2012-02-16	55973	s51	51	760	cw	0.227	none	07:34:18-07:38:30	3	
			s49			15	0.075	65535	07:40:56-07:46:52	4	
						cw		none	07:48:38-07:51:06	2	
			s49			15	0.075	65535	07:53:28-09:38:16	62	30-37
G	2012-02-16	55973	s49	51	420	cw		none	09:15:46-09:23:30	5	
			s49			75	1.532	255	09:56:39-10:02:39	4	
			s49			37.5	0.488	none	11:35:21-11:46:33	7*	
			s49			15	1.0	none	12:15:54-12:47:10	18*	43-44
			s49			15	1.0	none	13:10:01-13:28:09	11*	45

images. CW data are typically used to measure total echo power and frequency extent, whereas range-Doppler images are typically used to resolve the target in two dimensions. Table 1.1 summarizes the CW and range-Doppler imaging runs.

Table 1.1 (cont'd)

Tel	UT Date yyyy-mm-dd	MJD	Eph	RTT (s)	PTX (kW)	δr (m)	δf (Hz)	N	Start-Stop hh:mm:ss-hh:mm:ss	Runs	Fig. 1.8 key
			s49			15	1.0	none	13:29:04-15:29:31	70*	46-53
A	2012-02-17	55974	s53	48	775	cw	0.244	none	07:38:00-07:41:57	3	
			s53			15	0.075	65535	07:44:36-08:48:59	40	38-42
G	2012-02-17	55974	s53	48	420	cw		none	07:05:53-07:13:10	5	
			s53			75	1.532	255	07:42:55-08:00:01	11	
			s53			37.5	0.977	none	08:16:57-12:24:19	152*	54-65
G	2012-02-18	55975	s53	47	420	cw		none	07:05:51-07:12:50	5	
			s53			75	1.532	255	07:36:04-07:50:52	10	
			s53			37.5	0.977	none	08:01:15-08:31:44	20*	66
			s53			37.5	0.977	none	08:36:51-08:45:24	6*	67
G	2012-02-19	55976	s55	46	420	cw		none	07:05:51-07:12:41	5	
			s55			75	1.532	255	07:21:55-07:36:25	10	
			s55			37.5	0.977	none	07:46:12-11:13:58	136*	68-76
			s55			37.5	0.977	none	11:44:10-13:07:06	55*	77-80
G	2012-02-20	55977	s57	46	420	cw		none	07:10:51-07:17:42	5	
			s57			37.5	0.977	none	08:12:13-09:18:53	44*	81-84
			s57			37.5	0.977	none	10:31:49-11:33:59	41*	85-87
			s57			37.5	0.977	none	12:16:08-12:19:54	3*	
G	2012-02-22	55979	s59	48	420	cw		none	09:48:25-09:55:42	5	
			s59			75	0.957	255	10:02:53-10:21:35	12	
			s59			37.5	0.977	none	10:32:51-10:35:14	2*	
			s59			37.5	0.977	none	10:36:06-10:45:02	6*	

Table 1.1 (cont'd)

Tel	UT Date yyyy-mm-dd	MJD	Eph	RTT (s)	PTX (kW)	δr (m)	δf (Hz)	N	Start-Stop hh:mm:ss-hh:mm:ss	Runs	Fig. 1.8 key
G	2012-02-23	55980	s59	51	420	cw		none	08:33:10-08:40:53	5	
			s59			75	0.957	255	08:49:48-09:09:41	12	
			s59			75	0.977	none	09:20:46-10:55:20	55*	88-90
A	2012-08-24	56163	s72	153	721	cw		none	15:10:51-15:18:25	2	
						cw		none	15:46:51-16:31:17	9	
						150	0.954	8191	16:36:59-17:41:01	13	
A	2012-08-26	56165	s72	157	722	cw		none	15:04:24-16:20:38	15	

Note. — The first column indicates the telescope: Arecibo Planetary Radar (A) or Goldstone Solar System Radar at DSS-14 (G). MJD is the modified Julian date of the observation. Eph is the ephemeris solution number used (Section 1.3). RTT is the round-trip light-time to the target. PTX is the transmitter power. δr and δf are the range and Doppler resolutions, respectively, of the processed data. N is the number of bauds or the length of the pseudo-random code used. The timespan of the received data is listed by their UT start and stop times. Runs is the number of transmit-receive cycles during the timespan. An asterisk (*) indicates chirp runs. Last column indicates the key to the image numbers shown in Fig. 1.8.

For CW runs a carrier wave at a fixed frequency was transmitted for the RTT to the asteroid. The received echo from the asteroid was demodulated, sampled, and recorded. A fast Fourier transform (FFT) was applied to each echo timeseries to obtain the CW spectra. The total frequency extent (Δf) or bandwidth (BW) of the CW spectra is equal to the sampling frequency (f_s) or the reciprocal of the sampling period (P_s):

$$\Delta f = f_s = \frac{1}{P_s}. \tag{1.1}$$

The spectral resolution (δf) is given by:

$$\delta f = \frac{\Delta f}{n}, \tag{1.2}$$

where n is the FFT length. Finer spectral resolution can be achieved by increasing n, however the signal-to-noise ratio (SNR) in each frequency bin decreases as $1/\sqrt{n}$. The finest possible resolution that can be achieved is limited by the number of samples obtained in one run. If we were recording for the full duration of the RTT, the number of samples obtained in one run would be $n = \text{RTT} \times f_s$, and the resolution would be $\delta f = 1/\text{RTT}$. In reality we cannot transmit for a full RTT as it takes several seconds to switch between transmission
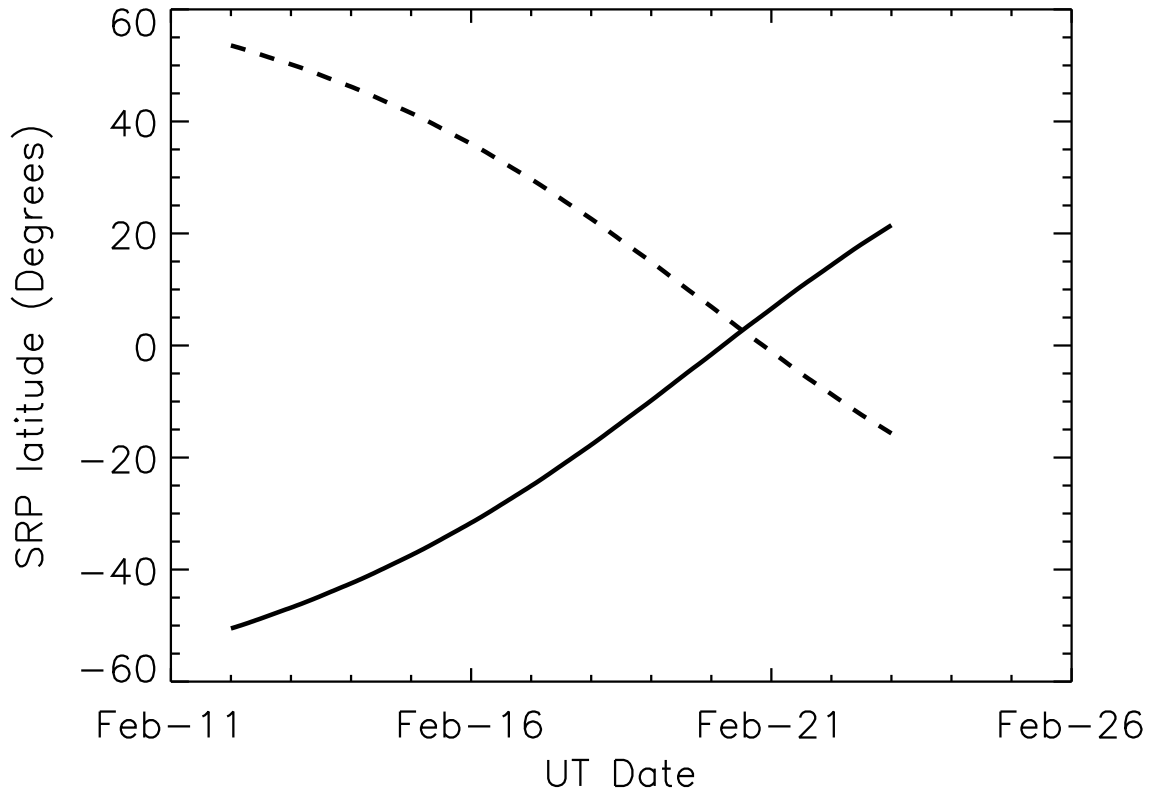
Figure 1.1: Sub-radar point (SRP) latitude during the primary observing period. Solid and dashed lines show SRP latitude for the prograde and retrograde spin vectors, respectively (Section 1.6).

and reception, so the finest possible resolution is $\delta f = 1/(\text{RTT} - t_{\text{switch}})$, where t_{switch} is the switching time.

For range-Doppler imaging two different *pulse compression* techniques were used to achieve fine range resolution while maintaining adequate SNR (Peebles, 2007). Pulse compression is a signal conditioning and processing technique used in radar systems to achieve a high range resolution without severely compromising the ability to detect or image the target. The range resolution achievable by a radar is proportional to the pulse duration, or, equivalently, inversely proportional to the effective bandwidth of the transmitted signal. However, decreasing the pulse duration reduces the total transmitted energy per pulse and hence it negatively affects the ability to detect the radar target. Pulse compression techniques allow for the transmission of a long pulse while still achieving the resolution of a short pulse.

1.2.1 Pulse compression using binary phase coding (BPC)

We used binary codes to produce range-Doppler images of the asteroid at both Arecibo and Goldstone. In this technique we modulated the transmitted carrier with a repeating pseudo-random code using binary phase shift keying (BPSK). The code contains N elements or *bauds* and the duration of each baud is T_{baud}. The duration of the code is called the pulse repetition period (PRP=$N \times T_{\text{baud}}$). The effective bandwidth of the transmitted signal (B_{eff}) is given by $1/T_{\text{baud}}$. For each run we transmitted for approximately the RTT to the asteroid, followed by reception for a similar duration. The received signal was demodulated and then decoded by cross-correlating it with a replica of the transmitted code. The images span a range (Δr) given by:

$$\Delta r = \frac{c}{2}\text{PRP}, \tag{1.3}$$

and their range resolution (δr) is given by:

$$\delta r = \frac{c}{2}T_{\text{baud}} = \frac{c}{2}\frac{1}{B_{\text{eff}}}, \tag{1.4}$$

9

where c is the speed of light. Each baud within the code eventually maps into to a particular range bin in the image. Resolution in the frequency or Doppler dimension was obtained in each range bin by performing a FFT on the sequence of returns corresponding to that bin. The total frequency extent (Δf) or bandwidth (BW) of the image is equal to the pulse repetition frequency (PRF) or the reciprocal of the PRP:

$$\Delta f = \text{PRF} = \frac{1}{\text{PRP}}. \tag{1.5}$$

The frequency resolution (δf) of the image depends on the FFT length (n) as follows:

$$\delta f = \frac{\Delta f}{n}. \tag{1.6}$$

The RTT dictates the finest frequency resolution achievable, similar to the situation with CW spectra.

1.2.2 Pulse compression using linear frequency modulation (Chirp)

We also used a linear frequency modulation technique (Margot, 2001; Peebles, 2007) to produce range-Doppler images of the asteroid at Goldstone. Only a fraction of the images were obtained in this mode because this new capability is still in the commissioning phase. Chirp waveforms allow us to maximize the bandwidth of the transmitted signal and to obtain better range resolution than that available with BPC waveforms. They are also less susceptible to degradation due to the Doppler spread of the targets. Finally, they are more amenable to the application of windowing functions that can be used to trade between range resolution and range sidelobe level (Margot, 2001).

In this technique the carrier was frequency modulated with a linear ramp signal. The resultant signal had a frequency that varied linearly with time from $\omega_0 - \omega$ to $\omega_0 + \omega$, where ω_0 is the carrier frequency and $B_{\text{eff}} = 2\omega$ is the effective bandwidth of the signal. The resultant signal is called a chirp. A repeating chirp was transmitted with 100% duty cycle for the duration of the round-trip light-time to the asteroid. The time interval between the

transmission of two consecutive chirps is the PRP. For our observations we used PRPs of 125 μs and 50 μs for chirps with B_{eff}=2 MHz and B_{eff}=5 MHz, respectively. The received signal was demodulated and range compression was achieved by cross-correlating the echo with a replica of the transmitted signal. The range extent and the range resolution of the chirp images are given by Eq. (1.3) and Eq. (1.4), respectively. Resolution in the frequency or Doppler dimension was obtained as in the binary coding technique. The bandwidth of the image is given by Eq. (1.5) and the frequency resolution is given by Eq. (1.6).

1.3   Astrometry and orbit

A radar astrometric measurement consists of a range or Doppler estimate of hypothetical echoes from the center of mass (COM) of the object at a specified coordinated universal time (UTC). In practice we used our measurements of the position of the leading edge of the echoes and our estimates of the object's size to report preliminary COM range estimates and uncertainties. We refined those estimates after we obtained a detailed shape model (Section 1.7). We measured Doppler astrometry from the CW spectra. We reported 9 range estimates and 1 Doppler estimate during the course of the observing run and computed the heliocentric orbit using the JPL on-site orbit determination software (OSOD). The ephemeris solution was updated each time new astrometric measurements were incorporated (Table 1.1). Using the best ephemeris solution at any given time minimizes smearing of the images.

At the end of our February observing campaign, we were using ephemeris solution 59. A final range measurement, obtained during the asteroid's close approach in August 2012, was incorporated to generate orbit solution 74. After the shape model was finalized, we updated the orbit to solution 76 by replacing the preliminary February astrometric measurements with more accurate shape-based estimates of the range to the center of mass (Table 1.2).

Table 1.3 lists the best fit orbital parameters (solution 76) generated using 18 range measurements and 316 optical measurements. The optical measurements span February 1977 to December 2012. However we assigned 20 arcsecond uncertainties to the two precovery observations from the 1977 La Silla-DSS plates, effectively removing their contribution to the

11

fit and reducing the optical arc to the interval 2000-2012. The 1977 observations were from a single, hour-long, trailed exposure, and appear to have been reported with a ∼45 s timing error, consistent with the measurers' cautionary note "Start time and exposure length are uncertain" (MPEC 2000-L19).

The orbit computation is reliable over a period from the year 460 to 2813. Beyond this interval either the 3σ uncertainty of the Earth close approach time (evaluated whenever the close approach distance is less than 0.1 AU) exceeds 10 days or the 3σ uncertainty of the Earth close approach distance exceeds 0.1 AU. The current *Minimum Orbit Intersection Distance* (MOID) with respect to Earth is 0.03154 AU, making 2000 ET70 a potentially hazardous asteroid (PHA).

1.4   Radar scattering properties

We transmitted circularly polarized waves and used two separate channels to receive echoes having the same circular (SC) and the opposite circular (OC) polarization as that of the transmitted wave (Ostro, 1993). Reflections from a plane surface reverse the polarization of the incident waves and most of the echo power is expected in the OC polarization. Echo power in the SC polarization is due to multiple reflections or reflections from structures with wavelength-scale roughness at the surface or sub-surface. A higher ratio of SC to OC power therefore indicates a greater degree of near-surface wavelength-scale roughness or multiple scattering. It is worth noting that while a larger SC to OC ratio implies a rougher surface, there is a compositional component at well (Benner et al., 2008). This *circular polarization ratio* is often denoted by μ_C. We measured μ_C for all the Arecibo spectra shown in Fig. 1.2 and computed an average value of $\mu_C = 0.21 \pm 0.02$, where the uncertainty is the standard deviation of the individual estimates. Observed ratios for individual spectra deviate no more than 0.03 from the average. This ratio is lower than that for the majority of NEAs with known circular polarization ratios (Mean = 0.34 ± 0.25, Median = 0.26) (Benner et al., 2008) suggesting that 2000 ET70 has a lower than average near-surface roughness at 10 cm scales.

Table 1.2. 2000 ET70 range measurements

Date (UTC) yyyy-mm-dd hh:mm:ss	Range μs	1-σ Uncertainty μs	Observatory
2012-02-12 08:50:00	67220894.76	0.5	A
2012-02-12 10:03:00	66974197.50	0.5	A
2012-02-13 09:11:00	62452848.06	0.5	A
2012-02-13 10:00:00	62298918.42	0.5	A
2012-02-14 09:28:00	58061903.74	0.5	A
2012-02-14 10:06:00	57953990.18	0.5	A
2012-02-14 10:16:00	57925824.25	0.5	A
2012-02-15 08:30:00	54319877.92	0.5	A
2012-02-15 09:20:00	54206358.81	3.0	G
2012-02-15 09:47:00	54126135.16	0.5	A
2012-02-16 08:23:00	50979848.61	0.5	A
2012-02-16 09:30:00	50840187.02	0.5	A
2012-02-17 08:05:00	48327621.88	0.5	A
2012-02-17 08:43:00	48267222.55	0.5	A
2012-02-18 07:40:00	46481930.28	2.0	G
2012-02-19 07:30:00	45481292.56	2.0	G
2012-02-20 10:10:00	45483470.81	2.0	G
2012-08-24 17:08:00	153139162.28	3.0	A

Note. — This table lists shape-based estimates of the range to the asteroid COM. The first column indicates the coordinated universal time (UTC) of the measurement epoch. The second column gives the ranges expressed as the RTT to the asteroid in microseconds (μs). The third column lists the 1σ range uncertainty. The fourth column indicates the radar used to make the measurement (A stands for the Arecibo Planetary Radar and G stands for the Goldstone Solar System Radar at DSS-14).

Table 1.3.   2000 ET70 heliocentric orbital elements (solution 76)

Element	Value	1-σ Uncertainty
eccentricity	0.123620379	6.3×10^{-8}
semi-major axis (AU)	0.9466347364	1.2×10^{-9}
inclination (degrees)	22.3232174	1.2×10^{-6}
longitude of ascending node (degrees)	331.16730395	9.8×10^{-7}
argument of perihelion (degrees)	46.106698	1.1×10^{-5}
Mean anomaly (degrees)	84.37370818	4.2×10^{-7}

Note. — All orbital elements are specified at epoch 2012 Dec 15.0 barycentric dynamical time (TDB) in the heliocentric ecliptic reference frame of J2000. The corresponding orbital period is $(336.41246710 \pm 5.5 \times 10^{-7})$ days.
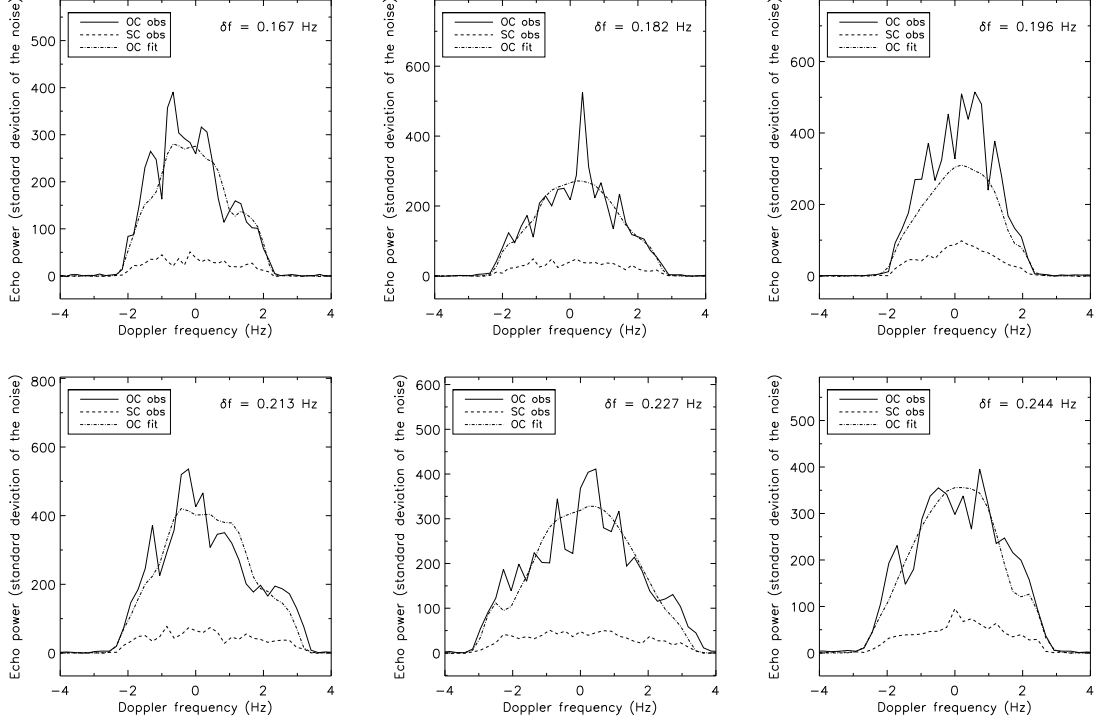
Figure 1.2: Arecibo CW spectra of 2000 ET70 arranged in chronological order from left to right and top to bottom. They were obtained on February 12-17 (MJDs 55969.35, 55970.34, 55971.33, 55972.32, 55973.32, 55974.32, respectively). The frequency resolution of each spectrum is given at the top right of the corresponding panel. Each spectrum was produced by choosing a frequency resolution that allowed for the incoherent sum of 10 independent spectra, or *looks*, per run, and by summing over 3 runs, resulting in a total number of 30 looks. The solid and dashed lines are observed OC and SC spectra, respectively. The dot-dashed line shows the corresponding synthetic OC spectra generated using our shape model (Section 1.7). The circular polarization ratio (μ_C) values in chronological order are 0.18, 0.20, 0.24, 0.21, 0.21, and 0.24 all of which have uncertainties of 5%, where the uncertainty is computed according to Ostro et al. (1983). The OC radar albedo values in chronological order are 0.091, 0.063, 0.073, 0.056, 0.051, and 0.044 all of which have uncertainties of 25%. The reduced chi-squares of the fits to the OC spectra vary between 0.69 to 0.72.

The average radar albedo computed for the OC CW spectra shown in Fig. 1.2 is 0.063 ± 0.017, where the uncertainty is the standard deviation of individual estimates. The radar albedo is the ratio of the radar cross-section to the geometric cross-sectional area of the target. The radar cross-section is the projected area of a perfectly reflective isotropic scatterer that would return the same power at the receiver as the target.

In our modeling of the shape of the asteroid (Sections 1.6 and 1.7), we used a cosine law to represent the radar scattering properties of 2000 ET70:

$$\frac{d\sigma}{dA} = R(C+1)(\cos \alpha)^{2C}. \tag{1.7}$$

Here σ is the radar cross section, A is the target surface area, R is the Fresnel reflectivity, C is a parameter describing the wavelength-scale roughness, and α is the incidence angle. Values of C close to 1 represent diffuse scattering, whereas larger values represent more specular scattering (Mitchell et al., 1996). For specular scattering, C is related to the wavelength-scale adirectional root-mean-square (RMS) slope S_0 and angle $\theta_{\rm rms}$ of the surface by $S_0 = \tan(\theta_{\rm rms}) = C^{-1/2}$.

1.5 Range and Doppler extents

The range extent of the object in the radar images varies between $\sim$600 m and $\sim$1700 m (Fig. 1.8), suggesting that the asteroid is significantly elongated. In most of the images two distinct ridges that surround a concavity are clearly visible (e.g., Fig. 1.8, images 8-12 and images 30-37). In images where the ridges are aligned with the Doppler axis, they span almost the entire bandwidth extent of the asteroid (e.g., Fig. 1.8, images 11 and 34). If the concavity is a crater then these ridges could mark its rim. At particular viewing geometries, the trailing end of the asteroid exhibits a large outcrop with a range extent of $\sim$250 m (e.g., Fig. 1.8, image 11). These features suggest that the overall surface of the asteroid is highly irregular at scales of hundreds of meters.

For a spherical object, the bandwidth (B) of the radar echo is given by:

$$B = \frac{4\pi D}{\lambda P} \cos \delta. \tag{1.8}$$

Here D is the diameter of the object, P is its apparent spin period, λ is the radar wavelength, and δ is the sub-radar latitude. As δ increases, B decreases. In images obtained at similar rotational phases, the bandwidth extent of the asteroid increased from February 12 to 20, indicating that our view was more equatorial towards the end of the observing campaign (Fig. 1.1). For example in Fig. 1.8, images 10, 33, and 68 are at similar rotational phases and their bandwidths (based on a 2380 MHz carrier) are $\sim$3.7 Hz, $\sim$4.9 Hz, and $\sim$6.3 Hz, respectively.

1.6   Spin vector

We used the SHAPE software (Hudson, 1993; Magri et al., 2007) to fit a shape model to the radar images and to estimate the spin vector of 2000 ET70. Since SHAPE is not particularly effective at fitting the spin axis orientation and spin period of the shape model, we carried out an extensive search for these parameters in an iterative manner. We performed two iterations each in our search for the spin axis orientation and spin period, where the result of each step provides initial conditions for the next optimization step. This approach leads to increased confidence that a global minimum is reached.

Our initial estimate of the spin period came from the time interval between repeating rotational phases of the object captured in the images. Fig. 1.3 shows the object at similar orientations in images taken on different days. The time interval in two of those cases is $\sim$72 hours and in the third case is $\sim$45 hours. This indicates that the spin period of the object is close to a common factor of the two, that is, 9 hours or a sub-multiple of 9 hours. Fig. 1.4 shows two images taken 22.5 hours apart and the object is not close to similar orientations in these two images, ruling out all periods that are factors of 22.5 hours. Thus we are left with a period close to 3 hours or 9 hours. Images obtained over observing runs longer than

3 hours do not show a full rotation of the asteroid, ruling out a spin period of 3 hours.

Using an initially fixed spin period of 9 hours, we performed an extensive search for the spin axis orientation. The search consisted of fitting shape models to the images under various assumptions for the spin axis orientation. We covered the entire celestial sphere with uniform angular separations of 15° between neighboring trial poles. At this stage we used a subset of the images in order to decrease the computational burden. We chose images showing sharp features that repeated on different days because they provide good constraints on the spin state. Images obtained on February 12 and 15 satisfied these criteria and we used images with receive times spanning MJDs 55969.426 to 55969.463 and 55972.335 to 55972.423 for this search. We started with triaxial ellipsoid shapes and allowed the least-squares fitting procedure to adjust all three ellipsoid dimensions in order to provide the best match between model and images. We then used shapes defined by a vertex model with 500 vertices and 996 triangular facets. The fitting procedure was allowed to adjust the positions of the vertices to minimize the misfit. In all of these fits the spin axis orientation and the spin rate were held constant. Radar scattering parameters R and C described in Eq. (1.7) were allowed to float. We found the best shape model fit with the spin pole at ecliptic longitude (λ) = 60° and ecliptic latitude (β) = -60°.

Using the best fit spin pole from the previous step, we proceeded to estimate the spin period with greater precision. We tried spin rates in increments of 2°/day from 960°/day (P = 9 hours) to 970°/day (P = 8.91 hours) to fit vertex shape models with 500 vertices to the images. This time we used a more extensive dataset consisting of all images obtained from Arecibo. As in the previous step, only the radar scattering parameters and the shape parameters were allowed to float in addition to the parameter of interest. We found the best agreement between model and observations with a spin rate of 964°/day (Period = 8.963 hours).

The second iteration of the spin-axis orientation search was similar to the first one except that we used a spin period of 8.963 hours and used the complete dataset consisting of all the Arecibo and Goldstone images from February. The Arecibo images from August were not used because of their low SNR and resolution. This procedure was very effective in
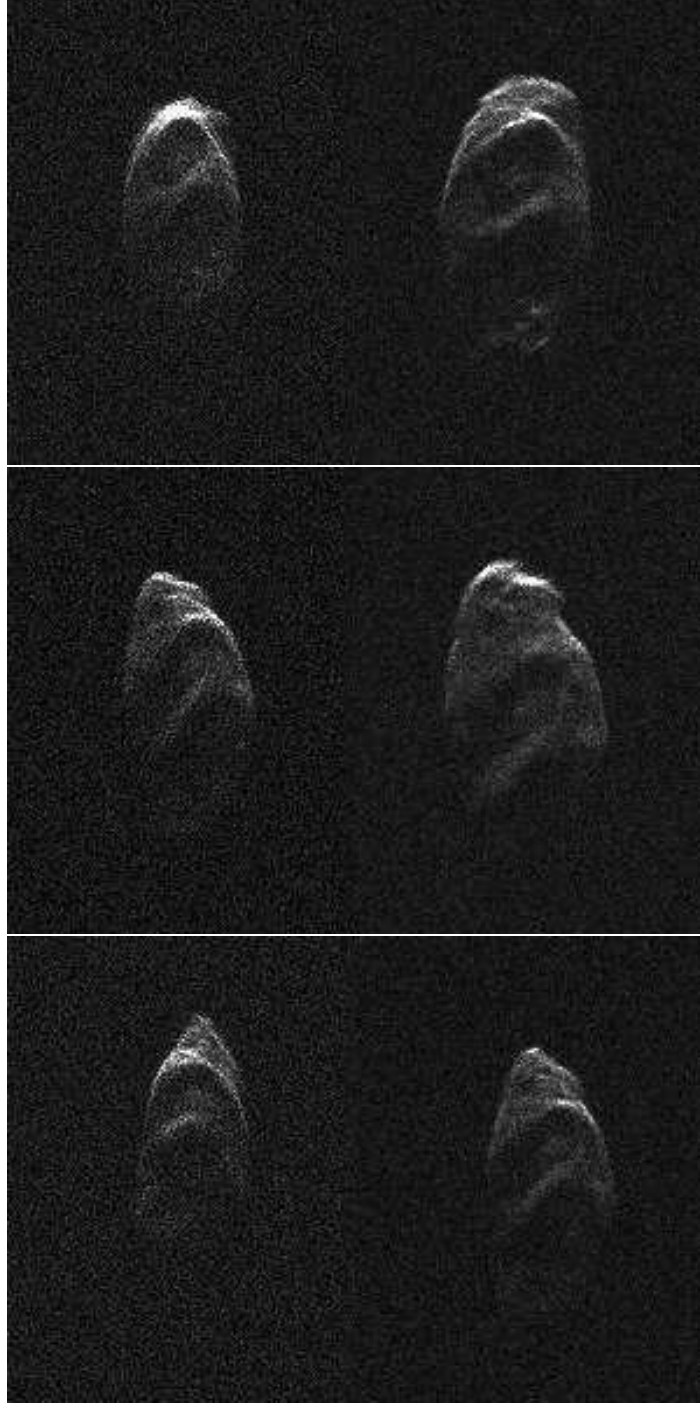
Figure 1.3: 2000 ET70 range-Doppler images showing the asteroid at similar rotational phases on different days. The images were obtained at MJDs 55970.40 and 55973.38 (∼72 hours apart) (top), 55971.35 and 55974.33 (∼72 hours apart) (center), 55969.46 and 55971.34 (∼45 hours apart) (bottom), suggesting a spin period of ∼9 hours or a sub-multiple of ∼9 hours. In these images radar illumination is from the top, range increases towards the bottom, Doppler frequency increases to the right, and the asteroid spin results in counter-clockwise rotation.

19

Figure 1.4: 2000 ET70 images obtained at MJDs 55970.40 and 55971.34, or 22.5 hours apart. The asteroid is not close to similar rotational phases in these images, ruling out spin periods that are sub-multiples of ∼22.5 hours. A ∼4.5-hour spin period is therefore ruled out, leaving ∼9 hours as the only plausible value.

constraining the possible spin axis orientations to a small region (around $\lambda = 79°$ and $\beta = -42°$) of the celestial sphere (Fig. 1.5). We performed a higher resolution search within this region with spin poles ranging in λ from 64° to 104° and β from -60° to -30° with step sizes of 4° in λ and 5° in β. For this step we performed triaxial ellipsoid fits followed by spherical harmonics model fits, adjusting spherical harmonic coefficients up to degree and order 10. Our best estimate of the spin axis orientation is $\lambda = 80°$ and $\beta = -50°$, with 10° uncertainties. Shape models with spin axis orientations within this region have similar appearance upon visual inspection. We also attempted shape model fits with the best-fit prograde pole at $\lambda = 232°$ and $\beta = 75°$. We found that we were unable to match the observed bandwidths and ruled out the prograde solution. 2000 ET70 is a retrograde spinner, just like the majority of NEAs (La Spina et al., 2004). Our adopted spin pole ($\lambda = 80°$, $\beta = -50°$) is at an angle of ∼160° from the heliocentric orbit pole ($\lambda = 241°$, $\beta = 68°$).

We used the best spherical harmonics shape model from the previous search to perform a second iteration of the spin period search. This time we fit spherical harmonics shape models using spin periods in increments of 0.001 hours from 8.940 hours to 8.980 hours. This final step was performed in part to quantify error bars on the spin period. The reduced chi-squares of the shape models, computed according to the method described in (Magri
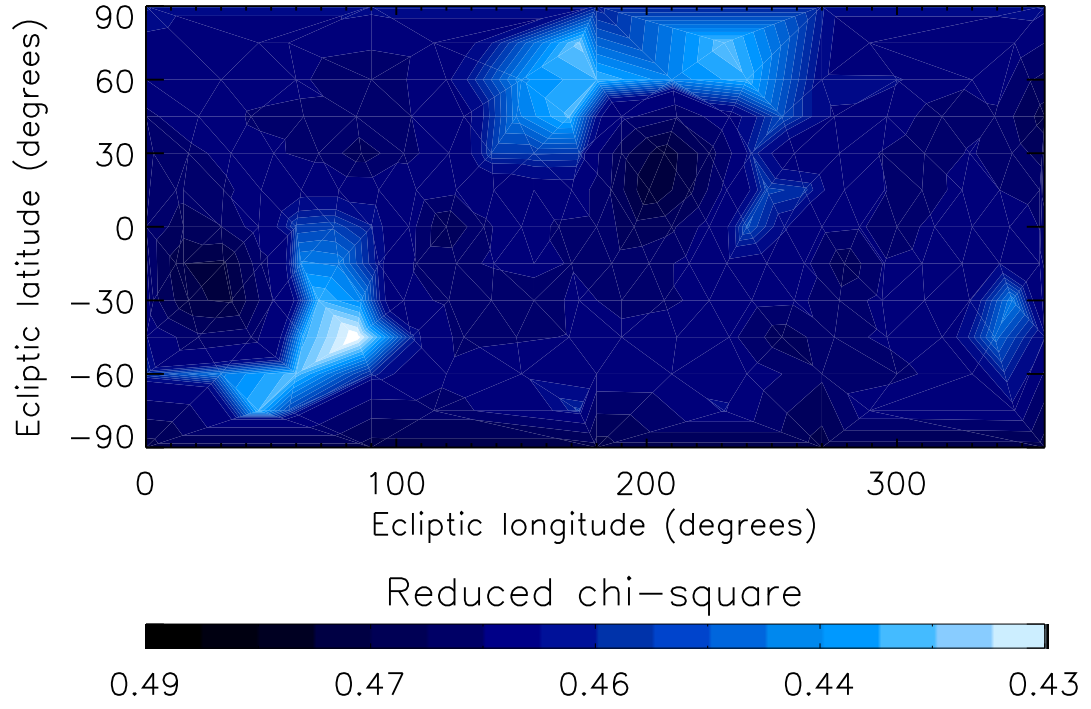
Figure 1.5: Contour plot showing goodness of fit (reduced chi-square) of shape model fits under various assumptions for the ecliptic longitude (λ) and ecliptic latitude (β) of the spin axis. The spin period was fixed at 8.963 hours for the fits. We adopted a best fit spin axis orientation of $\lambda = 80°$ and $\beta = -50°$ with a 10° uncertainty.
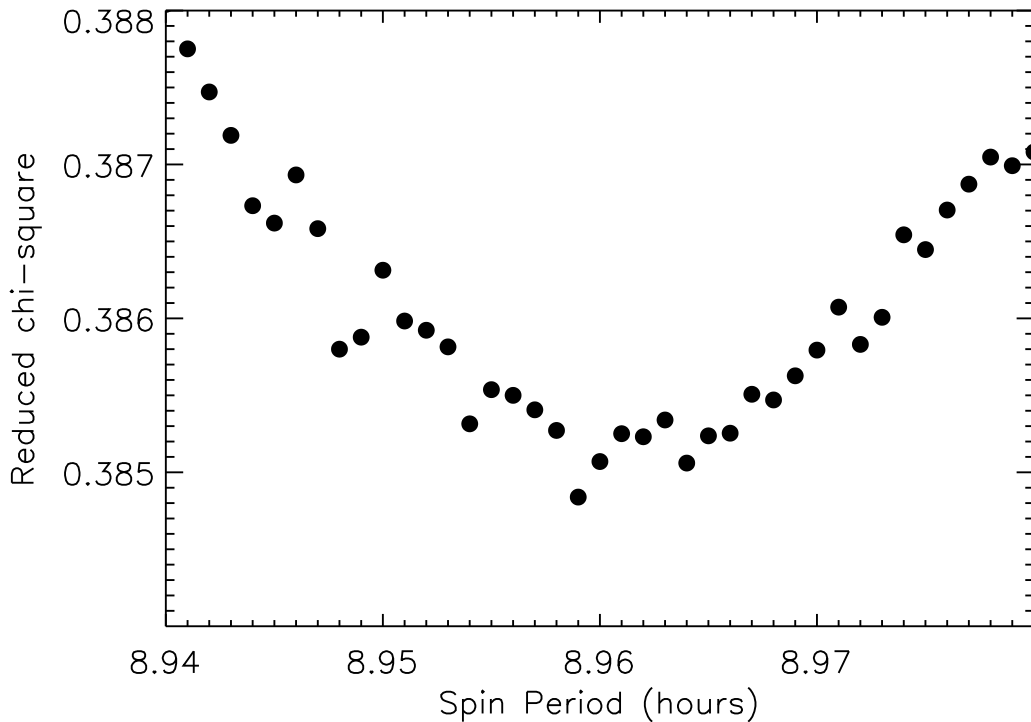
Figure 1.6: Goodness of fit (reduced chi-square) of degree-and-order 10 spherical harmonics shape models of 2000 ET70 as a function of assumed spin period. The spin pole was fixed at $\lambda = 80°$ and $\beta = -50°$ for the fits. We adopted a best fit spin period of 8.960±0.01 hours.

et al., 2007), are shown in Fig. 1.6. We visually verified the quality of the fits and adopted a spin period of 8.960 ± 0.01 hours. A 0.01 hour difference in spin period amounts to a $\sim 13°$ offset in rotational phase over the primary observing window which is detectable.

1.7 Shape model

As a starting point for our final shape modeling efforts we used the results of the spin state determination (Section 1.6), specifically the best-fit spherical harmonics shape model with a spin period of 8.960 hours and a spin pole at $\lambda = 80°$ and $\beta = -50°$. We proceeded to fit all the radar images obtained in February and OC CW spectra from Fig. 1.2 with a vertex model having 2000 vertices and 3996 facets. The number of vertices is based on experience and the desire to reproduce detectable features without over-interpretation. At this step

the vertex locations and the radar scattering parameters were fit for, but the spin vector was held fixed. Observed images were summed to improve their SNR. At Arecibo, 8 images were typically combined. At Goldstone, 14, 9, 13, 13, 14, 12, 6, and 12 images were typically combined on February 15, 16, 17, 18, 19, 20, 22, and 23, respectively. We cropped the images so that sufficient sky background remained for the computation of noise statistics, but the optimization procedure is robust against the amount of sky background. We minimized an objective function that consists of the sum of squares of residuals between model and actual images, plus a number of weighted penalty functions designed to favor models with uniform density, principal axis rotation, and a reasonably smooth surface (Hudson, 1993; Magri et al., 2007). The choice of weights in the penalty function is subjective, so the shape model solution is not unique. We tried to restrict the weights to the minimum value at which the penalty functions were effective. The minimization procedure with our choice of penalty functions produced a detailed shape model for 2000 ET70 (Fig. 1.7 and Table 2.3). The agreement between model and data is generally excellent but minor disagreements are observed (Fig. 1.8 and Fig. 1.2). The overall shape is roughly a triaxial ellipsoid with extents along the principal axes of $\sim$2.61 km, $\sim$2.22 km, and $\sim$2.04 km, which are roughly the same as the *dynamically equivalent equal volume ellipsoid* (DEEVE) dimensions listed in table 2.3.

The region around the north pole has two ridges that are 1-1.5 km in length and almost 100 m higher than their surroundings. These ridges enclose a concavity that seems more asymmetric than most impact craters. Along the negative x-axis a large protrusion is visible. Such a feature could arise if the asteroid were made up of multiple large components resting on each other.

NEAs in this size range for which radar shape models exist commonly exhibit irregular features such as concavities and ridges. A few examples include Golevka (Hudson et al., 2000), 1992 SK (Busch et al., 2006), and 1998 WT24 (Busch et al., 2008). The concavities observed on these NEAs can not be adequately captured by convex-only shape modeling techniques.

For this shape model, the best fit values for the radar scattering parameters, R and C, were 1.9 and 1.4, respectively (section 1.4). This value of C indicates that 2000 ET70 is
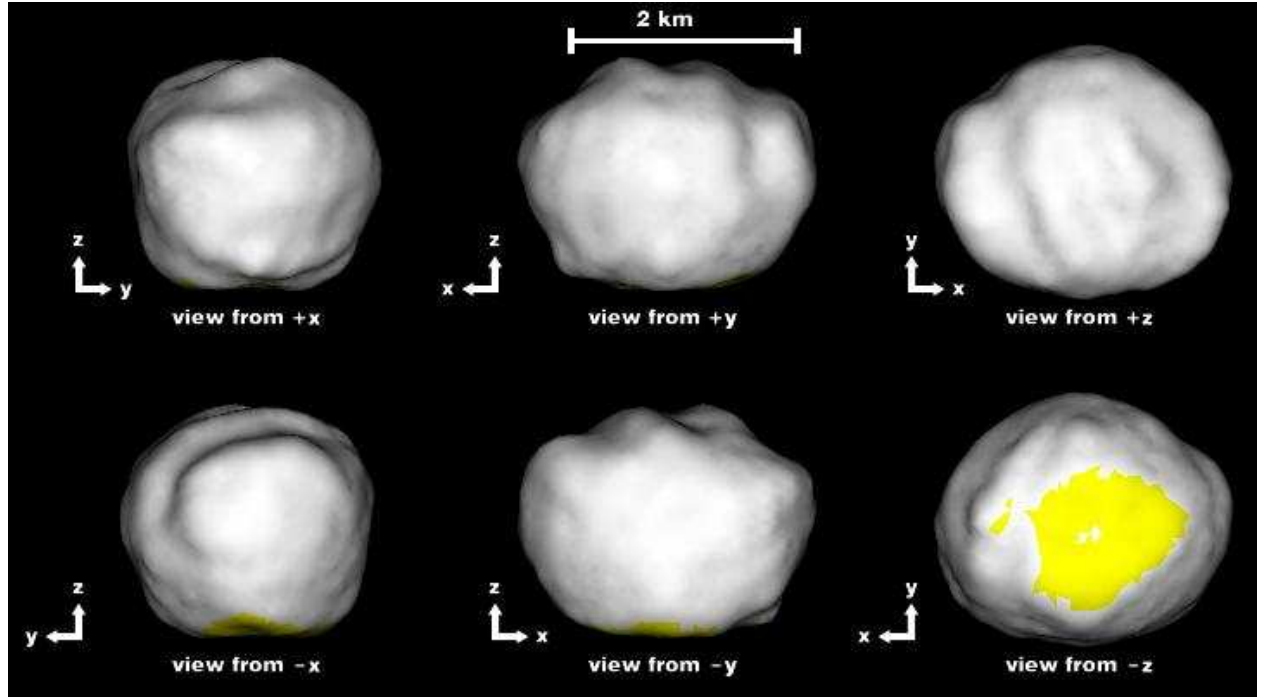
Figure 1.7: Best-fit vertex shape model of 2000 ET70 as seen along the three principal axes x, y, and z. For principal axis rotation the spin axis is aligned with the z axis. Yellow regions at the south pole have radar incidence angles $> 60°$ and hence are not well constrained. The shape model has 2000 vertices and 3996 triangular facets giving an effective surface resolution of ~ 100 m.

a diffuse scatterer, simlar to other NEAs such as Geographos (Hudson and Ostro, 1999), Golevka (Hudson et al., 2000), and 1998 ML14 (Ostro et al., 2001). NEAs are generally expected to be diffuse scatterers at radar wavelengths because of their small sizes and rough surfaces. Attempts to fit the echoes with a two-component scattering law (diffuse plus specular) did not yield significantly better results.

1.8 Gravitational environment

We used our best-fit shape model and a uniform density assumption of 2000 kg m^{-3}, a reasonable density for rubble-pile NEAs, (e.g., Ostro et al., 2006), to compute the gravity field at the surface of the asteroid (Werner and Scheeres, 1997). The acceleration on the surface is the sum of the gravitational acceleration due to the asteroid's mass and the centrifugal acceleration due to the asteroid's spin. An acceleration vector was computed at the center of each

24
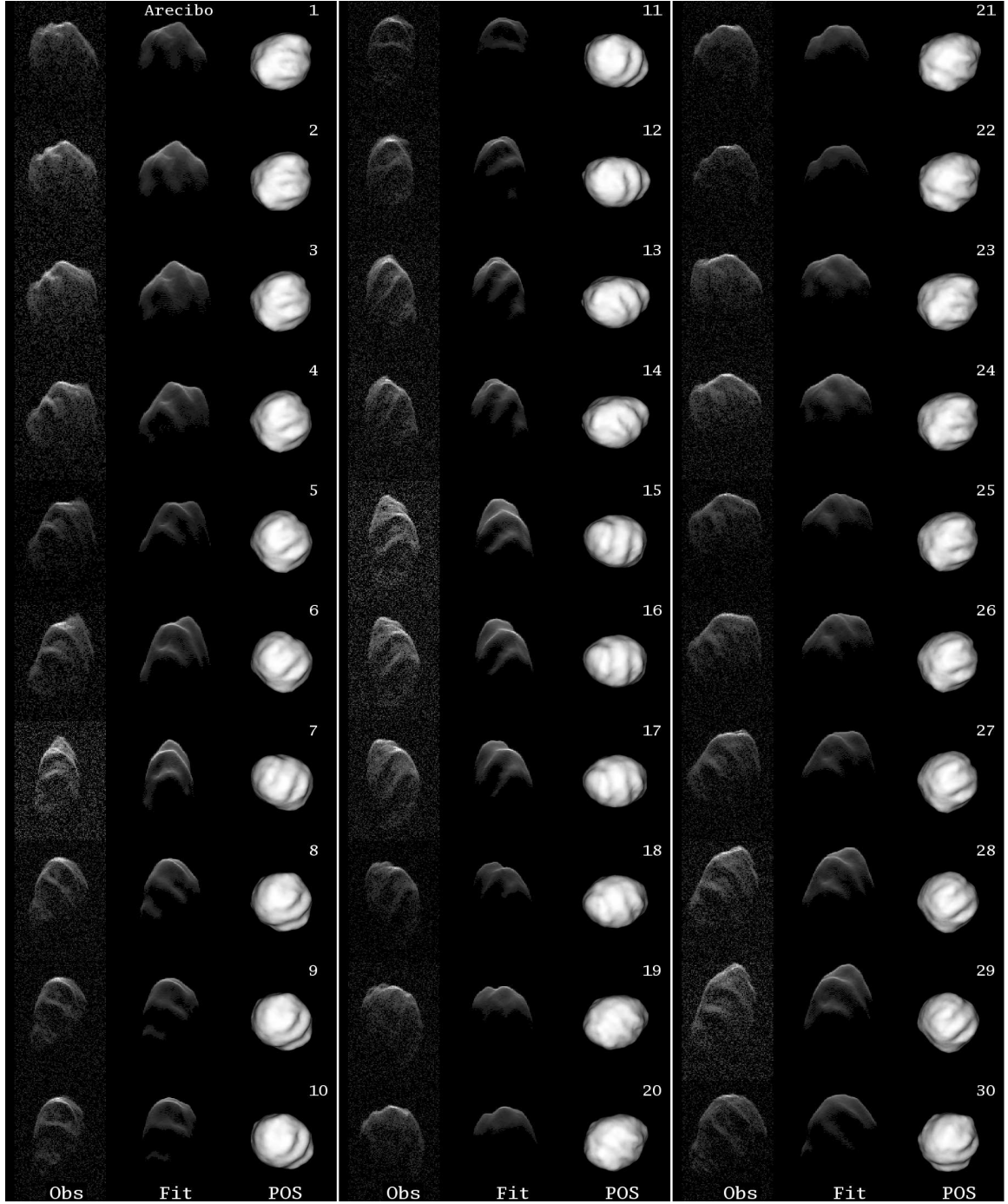
Figure 1.8: Comparison between radar range-Doppler images, corresponding synthetic radar images generated using our best-fit shape model, and plane-of-sky (POS) projections of the shape model. Range-Doppler images are oriented such that radar illumination is from the top, range increases towards the bottom, Doppler frequency increases to the right, and the asteroid spin results in counter-clockwise rotation. The POS projections are oriented north-up and east-left. Time increases from top to bottom within each panel and from left to right. The range and frequency resolutions of the images are given in Table 1.1. The reduced chi-square of the fit to the images is 0.27.
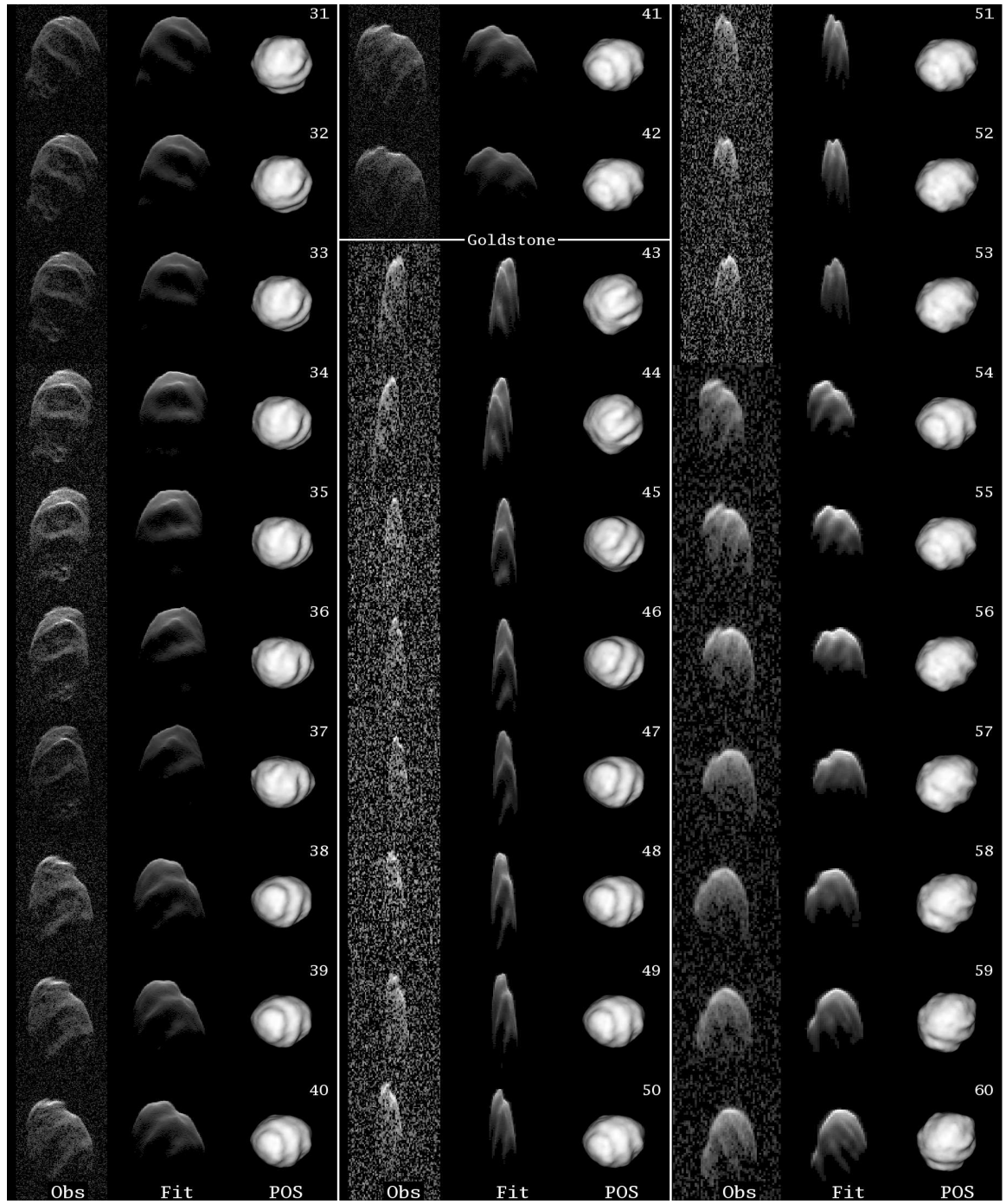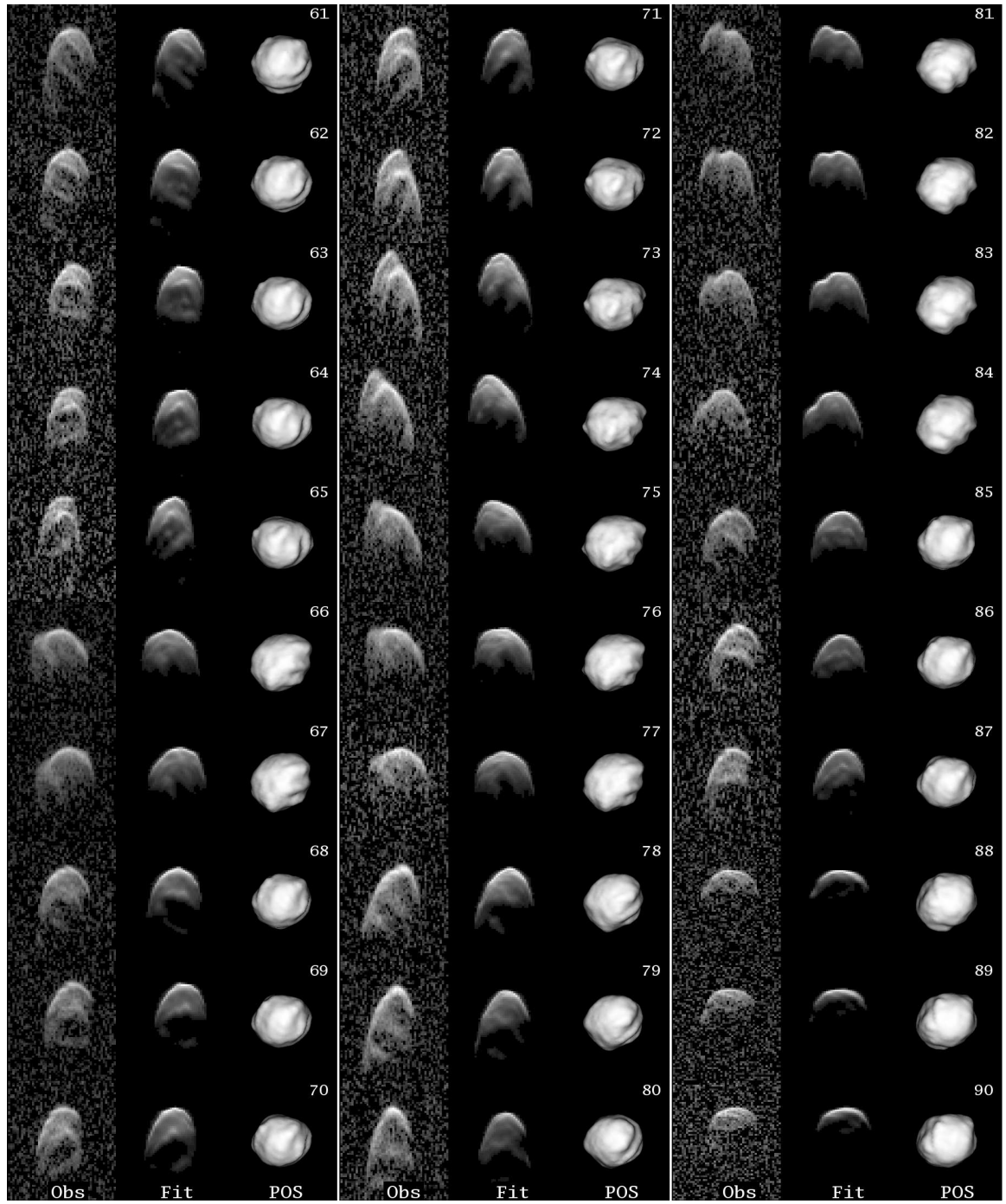
Table 1.4.   2000 ET70 shape model parameters

Parameters		Value
Extents along	x	2.61 ± 5%
principal axes (km)	y	2.22 ± 5%
	z	2.04 ± 5%
Surface Area (km^2)		16.7 ± 10%
Volume (km^3)		6.07 ± 15%
Moment of inertia ratios	A/C	0.800 ± 10%
	B/C	0.956 ± 10%
Equivalent diameter (km)		2.26 ± 5%
DEEVE extents (km)	x	2.56 ± 5%
	y	2.19 ± 5%
	z	2.07 ± 5%
Spin pole (λ, β) (°)		(80, -50) ± 10
Sidereal spin period (hours)		8.96 ± 0.01

Note. — The shape model consists of 2000 vertices and 3996 triangular facets, corresponding to an effective surface resolution of ∼100 m. The moment of inertia ratios were calculated assuming homogeneous density. Here A, B, and C are the principal moments of inertia, such that $A < B < C$. Equivalent diameter is the diameter of a sphere having the same volume as that of the shape model. A *dynamically equivalent equal volume ellipsoid* (DEEVE) is an ellipsoid with uniform density having the same volume and moment of inertia ratios as the shape model.

facet. Figure 1.9 shows the variation of the magnitude of this acceleration over the surface of the asteroid. The acceleration on the surface varies between 0.54 mm s^{-2} to 0.64 mm s^{-2}, which is 4 orders of magnitude smaller than that experienced on Earth and 2 orders of magnitude smaller than that on Vesta. Centrifugal acceleration makes a significant contribution to the total acceleration and varies from zero at the poles to $\sim$0.049 mm s^{-2} (about 10% of the total acceleration) on the most protruding regions of the equator. For comparison, on Earth, centrifugal acceleration contributes less than 0.5% to the total acceleration at the equator.

Fig. 1.10 shows the gravitational slope variation over the asteroid's surface. The gravitational slope is the angle that the local gravitational acceleration vector makes with the inward pointing surface-normal vector. The average slope is 9.5°. Less than 1% of the surface has slopes greater than 30°, the approximate angle of repose of sand, indicating a relaxed surface. Slopes on the sides of the ridges near the north pole reach up to $\sim$33°, and the sides facing the north pole are steeper than the opposite sides. As a result of the high slopes, along-the-surface accelerations are a substantial fraction of the total acceleration, reaching values as high as 0.34 mm s^{-2}. One might expect mass wasting to result from this gravitational environment: the sides of the ridges may have competent rocks exposed at the surface, and the valley between the two ridges may be overlain by a pond of accumulated regolith. A similar mass wasting process is hypothesized to have occurred on Eros (Zuber et al., 2000). The accumulation of fine-grained regolith could lower the wavelength-scale surface roughness locally and perhaps explain the lower values of μ_c observed at higher SRP latitudes (Fig. 1.2). A similar trend in μ_c was observed in the Goldstone CW spectra.

1.9   Discussion

Whiteley (2001) and Williams (2012) estimated 2000 ET70's absolute magnitude (H) to be near 18.2. The geometric albedo (p_V) of an asteroid is related to its effective diameter (D)
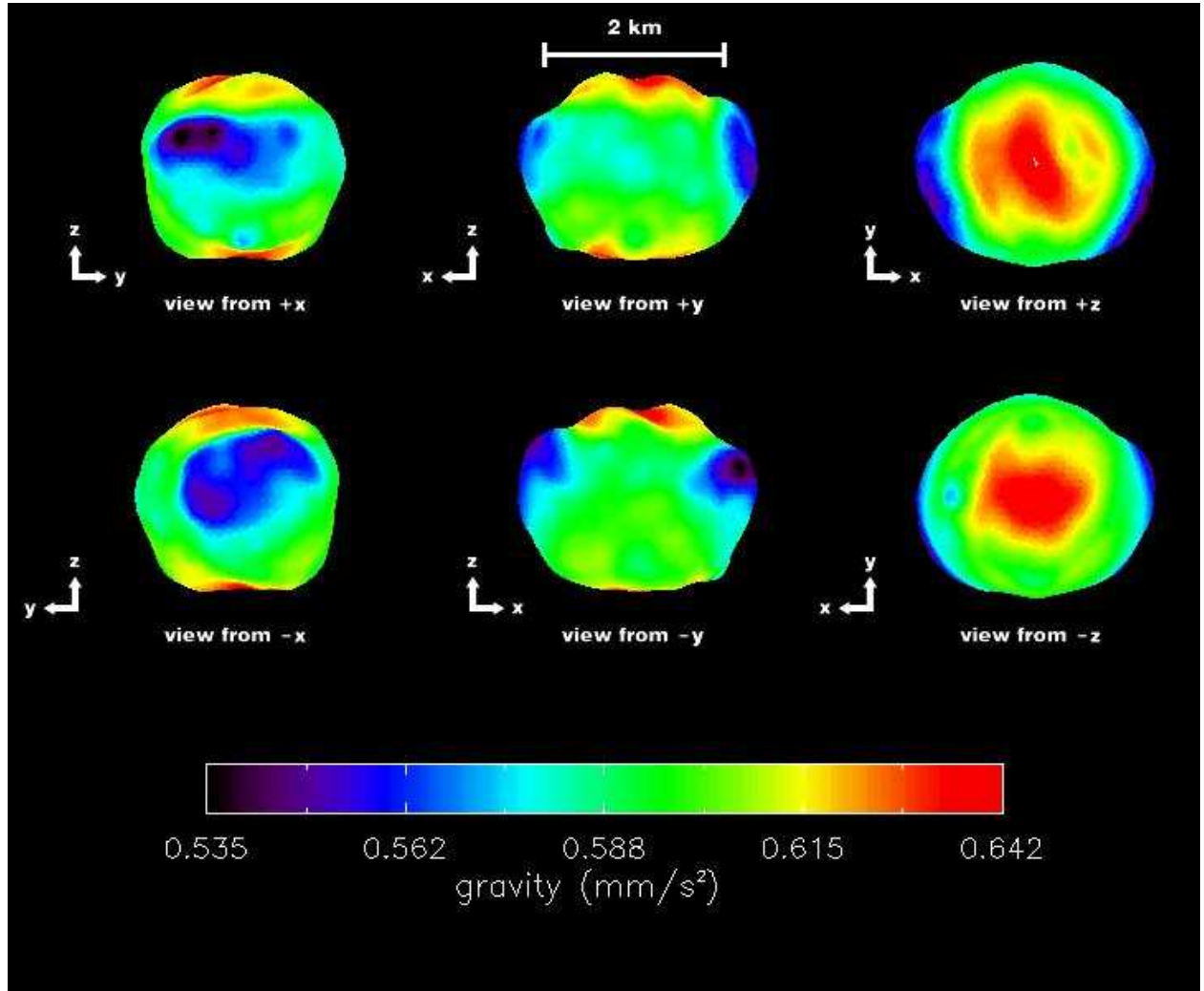
Figure 1.9: This figure shows the magnitude of the vector sum of acceleration due to gravity and centrifugal acceleration computed at the center of each facet of the shape model. We assumed a uniform density of 2000 kg m^{-3} and used our measured spin period value of 8.96 hours. Centrifugal acceleration makes a significant contribution to the total acceleration; at the most protruding regions of the equator it accounts for about 10%.
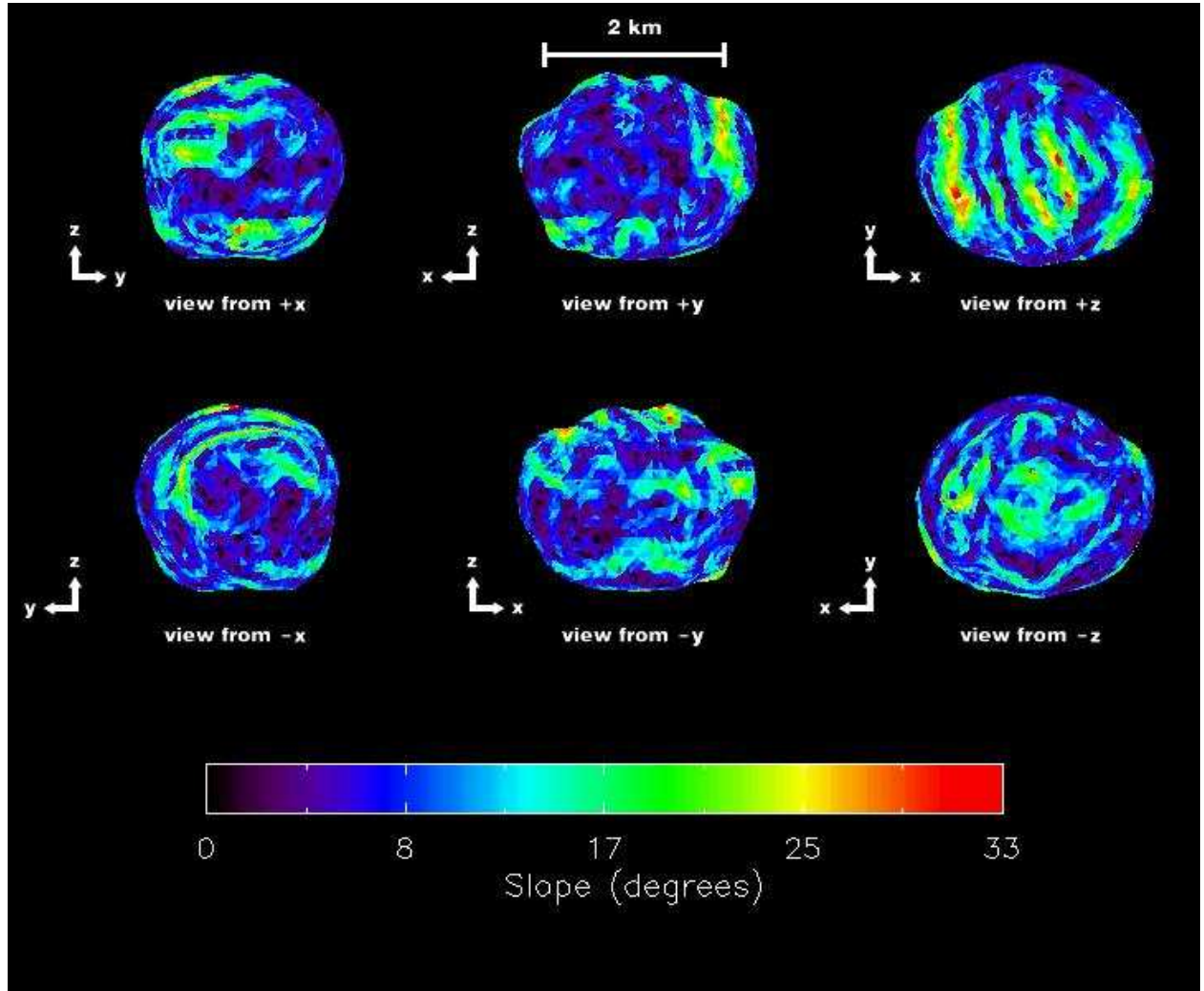
Figure 1.10: This figure shows the gravitational slopes computed at the center of each facet of the shape model. The gravitational slope is the angle that the local gravitational acceleration vector makes with the inward pointing surface-normal vector. We assumed a uniform density of 2000 kg m^{-3} and used our measured spin period value of 8.96 hours. Sides of the ridges near the north pole have slopes exceeding 30°, the approximate angle of repose of sand.

and its H value by (Pravec and Harris, 2007, and references therein):

$$p_V = \left[\frac{1329 \text{ km} \times 10^{-0.2H}}{D} \right]^2. \tag{1.9}$$

Using Whiteley (2001)'s H=18.2, the above equation yields p_V=0.018±0.002 for an asteroid with an effective diameter of 2.26 km ± 5% (Fig. 1.11). This uncertainty on p_V is due to the diameter uncertainty only. A geometric albedo near 2% is extremely low compared to the albedos of other NEAs (Thomas et al., 2011; Stuart and Binzel, 2004). More common values of p_V would require lower values of the absolute magnitude (e.g., p_V=0.04 requires H=17.5). The range of possible H and p_V values that are consistent with the radar size estimates is shown in Fig. 1.11. We conclude that 2000 ET70 has either an extremely low albedo or unusual phase function.

Alvarez et al. (2012) observed the asteroid between February 19 to 24, when the view was close to the equator, and reported a lightcurve amplitude of 0.60 ± 0.07 mag. If the asteroid was approximated by a triaxial ellipsoid with uniform albedo, this amplitude would suggest an elongation (ratio of equatorial axes) approximately between 1.28 and 1.36. Our shape model indicates that this ratio is ~1.18, suggesting that either the ellipsoid approximation is poor, the lightcurve amplitude is on the lower end of the range above, shadowing due to the terrain is playing an important role, there are albedo variations over the surface of the asteroid, or a combination of these factors.

Alvarez et al. (2012) also report a lightcurve period of 8.947 ± 0.001 hours. Their reported period is a function of the intrinsic spin state of the asteroid and of the relative motion between the asteroid, the observer, and the Sun. Therefore, it is close to but not exactly equivalent to the *synodic period*, which combines the (fixed) intrinsic rotation and the (variable) apparent rotation due to sky motion, but is independent of the position of the Sun. If we assume that the reported lightcurve period is equivalent to the synodic period, we can compute the corresponding sidereal periods. This transformation depends on the spin axis orientation. In the absence of information about the spin axis orientation, a synodic period of 8.947 maps into sidereal periods between 8.902 h and 8.992 h, i.e., a range that

is about 100 times larger than the precision reported for the lightcurve period. This range includes the sidereal period that we derived from the shape modeling process (8.960 ± 0.01 h). If we use our value and our best-fit spin axis orientation we can evaluate corresponding synodic periods at various epochs. On Feb 19.0, the nominal synodic period was 8.937 hours, whereas on Feb 25.0, the nominal synodic period was 8.943 hours. These synodic periods are close to the reported lightcurve period, but cannot be directly compared to it as they measure slightly different phenomena.

Arecibo and Goldstone radar observations of 2000 ET70 allowed us to provide a detailed characterization of a potentially hazardous asteroid, including its size, shape, spin state, scattering properties, and gravitational environment. These techniques are applicable to a substantial fraction of known NEAs that make close approaches to Earth within ∼0.1 AU. Radar-based physical properties for this and other asteroids are available at http://radarastronomy.org

Figure 1.11: Absolute magnitude vs. geometric albedo for an effective diameter of 2.26 km (dark line) and a diameter uncertainty of 5% (light lines). The horizontal dashed line corresponds to the absolute magnitude (H=18.2) reported by Whiteley (2001), and the vertical dashed lines indicate the corresponding geometric albedos. These albedo values are unusually low, suggesting an extraordinarily dark object or an object having an unusual phase function.

Bibliography

E. M. Alvarez, J. Oey, X. L. Han, O. R. Heffner, A. W. Kidd, B. J. Magnetta, and F. W. Rastede. Period Determination for NEA (162421) 2000 ET70. *Minor Planet Bulletin*, 39: 170, July 2012.

L. A. M. Benner, S. J. Ostro, M. C. Nolan, J. L. Margot, J. D. Giorgini, R. S. Hudson, R. F. Jurgens, M. A. Slade, E. S. Howell, D. B. Campbell, and D. K. Yeomans. Radar observations of asteroid 1999 JM8. *Meteoritics and Planetary Science*, 37:779–792, June 2002.

L. A. M. Benner, M. C. Nolan, S. J. Ostro, J. D. Giorgini, D. P. Pray, A. W. Harris, C. Magri, and J. L. Margot. Near-Earth Asteroid 2005 CR37: Radar images and photometry of a candidate contact binary. *Icarus*, 182:474–481, June 2006.

L. A. M. Benner, S. J. Ostro, C. Magri, M. C. Nolan, E. S. Howell, J. D. Giorgini, R. F. Jurgens, J. L. Margot, P. A. Taylor, M. W. Busch, and M. K. Shepard. Near-Earth asteroid surface roughness depends on compositional class. *Icarus*, 198:294–304, December 2008. doi: 10.1016/j.icarus.2008.06.010.

M. Brozovic, L. A. M. Benner, C. Magri, S. J. Ostro, D. J. Scheeres, J. D. Giorgini, M. C. Nolan, J. L. Margot, R. F. Jurgens, and R. Rose. Radar observations and a physical model of contact binary Asteroid 4486 Mithra. *Icarus*, 208:207–220, July 2010.

M. Brozović, L. A. M. Benner, P. A. Taylor, M. C. Nolan, E. S. Howell, C. Magri, D. J. Scheeres, J. D. Giorgini, J. T. Pollock, P. Pravec, A. Galád, J. Fang, J. L. Margot, M. W. Busch, M. K. Shepard, D. E. Reichart, K. M. Ivarsen, J. B. Haislip, A. P. Lacluyze, J. Jao, M. A. Slade, K. J. Lawrence, and M. D. Hicks. Radar and optical observations and physical modeling of triple near-Earth Asteroid (136617) 1994 CC. *Icarus*, 216:241–256, November 2011.

M. W. Busch, S. J. Ostro, L. A. M. Benner, J. D. Giorgini, R. F. Jurgens, R. Rose, C. Magri, P. Pravec, D. J. Scheeres, and S. B. Broschart. Radar and optical observations and physical

modeling of near-Earth Asteroid 10115 (1992 SK). *Icarus*, 181:145–155, March 2006. doi: 10.1016/j.icarus.2005.10.024.

M. W. Busch, L. A. M. Benner, S. J. Ostro, J. D. Giorgini, R. F. Jurgens, R. Rose, D. J. Scheeres, C. Magri, J. L. Margot, M. C. Nolan, and A. A. Hine. Physical properties of near-Earth Asteroid (33342) 1998 WT24. *Icarus*, 195:614–621, June 2008. doi: 10.1016/j.icarus.2008.01.020.

S. R. Chesley, S. J. Ostro, D. Vokrouhlický, D. Čapek, J. D. Giorgini, M. C. Nolan, J. L. Margot, A. A. Hine, L. A. M. Benner, and A. B. Chamberlin. Direct Detection of the Yarkovsky Effect by Radar Ranging to Asteroid 6489 Golevka. *Science*, 302:1739–1742, December 2003.

F. E. DeMeo, R. P. Binzel, S. M. Slivan, and S. J. Bus. An extension of the Bus asteroid taxonomy into the near-infrared. *Icarus*, 202:160–180, July 2009. doi: 10.1016/j.icarus.2009.02.005.

J. Fang and J. L. Margot. Near-Earth Binaries and Triples: Origin and Evolution of Spin-Orbital Properties. *AJ*, 143:24, January 2012. doi: 10.1088/0004-6256/143/1/24.

J. Fang, J. L. Margot, M. Brozovic, M. C. Nolan, L. A. M. Benner, and P. A. Taylor. Orbits of Near-Earth Asteroid Triples 2001 SN263 and 1994 CC: Properties, Origin, and Evolution. *AJ*, 141:154–+, May 2011.

R. S. Hudson and S. J. Ostro. Physical Model of Asteroid 1620 Geographos from Radar and Optical Data. *Icarus*, 140:369–378, August 1999. doi: 10.1006/icar.1999.6142.

R. S. Hudson, S. J. Ostro, R. F. Jurgens, K. D. Rosema, J. D. Giorgini, R. Winkler, R. Rose, D. Choate, R. A. Cormier, C. R. Franck, R. Frye, D. Howard, D. Kelley, R. Littlefair, M. A. Slade, L. A. M. Benner, M. L. Thomas, D. L. Mitchell, P. W. Chodas, D. K. Yeomans, D. J. Scheeres, P. Palmer, A. Zaitsev, Y. Koyama, A. Nakamura, A. W. Harris, and M. N. Meshkov. Radar Observations and Physical Model of Asteroid 6489 Golevka. *Icarus*, 148:37–51, November 2000. doi: 10.1006/icar.2000.6483.

R.S. Hudson and S.J. Ostro. Shape of asteroid 4769 Castalia (1989 PB) from inversion of radar images. *Science*, 263:940–943, February 1994.

S. Hudson. Three-dimensional reconstruction of asteroids from radar observations. *Remote Sensing Reviews*, 8:195–203, 1993.

A. La Spina, P. Paolicchi, A. Kryszczyńska, and P. Pravec. Retrograde spins of near-Earth asteroids from the Yarkovsky effect. *Nature*, 428:400–401, March 2004. doi: 10.1038/nature02411.

S. C. Lowry, A. Fitzsimmons, P. Pravec, D. Vokrouhlický, H. Boehnhardt, P. A. Taylor, J. L. Margot, A. Galád, M. Irwin, J. Irwin, and P. Kusnirák. Direct Detection of the Asteroidal YORP Effect. *Science*, 316:272–, April 2007.

C. Magri, S. J. Ostro, D. J. Scheeres, M. C. Nolan, J. D. Giorgini, L. A. M. Benner, and J. L. Margot. Radar observations and a physical model of Asteroid 1580 Betulia. *Icarus*, 186:152–177, January 2007. doi: 10.1016/j.icarus.2006.08.004.

J. L. Margot. Planetary Radar Astronomy with Linear FM (chirp) Waveforms. Arecibo technical and operations memo series 2001-09, Arecibo Observatory, 2001.

J. L. Margot, M. C. Nolan, L. A. M. Benner, S. J. Ostro, R. F. Jurgens, J. D. Giorgini, M. A. Slade, and D. B. Campbell. Binary Asteroids in the Near-Earth Object Population. *Science*, 296:1445–1448, May 2002. doi: 10.1126/science.1072094.

D. L. Mitchell, S. J. Ostro, R. S. Hudson, K. D. Rosema, D. B. Campbell, R. Velez, J. F. Chandler, I. I. Shapiro, J. D. Giorgini, and D. K. Yeomans. Radar Observations of Asteroids 1 Ceres, 2 Pallas, and 4 Vesta. *Icarus*, 124:113–133, November 1996. doi: 10.1006/icar.1996.0193.

M. C. Nolan, E. S. Howell, T. M. Becker, C. Magri, J. D. Giorgini, and J. L. Margot. Arecibo Radar Observations of 2001 SN263: A Near-Earth Triple Asteroid System. In *Bulletin of the American Astronomical Society*, volume 40, 2008.

C. R. Nugent, J. L. Margot, S. R. Chesley, and D. Vokrouhlický. Detection of semi-major axis drifts in 54 near-earth asteroids: New measurements of the yarkovsky effect. *Astronomical Journal*, 144:60, 2012. Arxiv eprint 1204.5990.

S. J. Ostro. Planetary radar astronomy. *Reviews of Modern Physics*, 65:1235–1279, October 1993. doi: 10.1103/RevModPhys.65.1235.

S. J. Ostro, D. B. Campbell, and I. I. Shapiro. Radar observations of asteroid 1685 Toro. *AJ*, 88:565–576, April 1983. doi: 10.1086/113345.

S. J. Ostro, R. S. Hudson, R. F. Jurgens, K. D. Rosema, D. B. Campbell, D. K. Yeomans, J. F. Chandler, J. D. Giorgini, R. Winkler, R. Rose, S. D. Howard, M. A. Slade, P. Perillat, and I. I. Shapiro. Radar Images of Asteroid 4179 Toutatis. *Science*, 270:80–83, October 1995. doi: 10.1126/science.270.5233.80.

S. J. Ostro, R. S. Hudson, L. A. M. Benner, M. C. Nolan, J. D. Giorgini, D. J. Scheeres, R. F. Jurgens, and R. Rose. Radar observations of asteroid 1998 ML14. *Meteoritics and Planetary Science*, 36:1225–1236, September 2001. doi: 10.1111/j.1945-5100.2001.tb01956.x.

S. J. Ostro, J. L. Margot, L. A. M. Benner, J. D. Giorgini, D. J. Scheeres, E. G. Fahnestock, S. B. Broschart, J. Bellerose, M. C. Nolan, C. Magri, P. Pravec, P. Scheirich, R. Rose, R. F. Jurgens, E. M. De Jong, and S. Suzuki. Radar Imaging of Binary Near-Earth Asteroid (66391) 1999 KW4. *Science*, 314:1276–1280, November 2006. doi: 10.1126/science.1133622.

P.Z. Peebles. *Radar Principles*. Wiley India Pvt. Limited, 2007. ISBN 9788126515271. URL http://books.google.com/books?id=rnX21aAMKCIC.

P. Pravec and A. W. Harris. Binary asteroid population. 1. Angular momentum content. *Icarus*, 190:250–259, September 2007. doi: 10.1016/j.icarus.2007.02.023.

D. J. Scheeres, E. G. Fahnestock, S. J. Ostro, J. L. Margot, L. A. M. Benner, S. B. Broschart, J. Bellerose, J. D. Giorgini, M. C. Nolan, C. Magri, P. Pravec, P. Scheirich, R. Rose, R. F. Jurgens, E. M. De Jong, and S. Suzuki. Dynamical Configuration of Binary Near-Earth

Asteroid (66391) 1999 KW4. *Science*, 314:1280–1283, November 2006. doi: 10.1126/science.1133599.

M. K. Shepard, J. L. Margot, C. Magri, M. C. Nolan, J. Schlieder, B. Estes, S. J. Bus, E. L. Volquardsen, A. S. Rivkin, L. A. M. Benner, J. D. Giorgini, S. J. Ostro, and M. W. Busch. Radar and infrared observations of binary near-Earth Asteroid 2002 CE26. *Icarus*, 184: 198–210, September 2006. doi: 10.1016/j.icarus.2006.04.019.

J. S. Stuart and R. P. Binzel. Bias-corrected population, size distribution, and impact hazard for the near-Earth objects. *Icarus*, 170:295–311, August 2004. doi: 10.1016/j.icarus.2004.03.018.

P. A. Taylor and J. L. Margot. Binary asteroid systems: Tidal end states and estimates of material properties. *Icarus*, 212:661–676, April 2011.

P. A. Taylor, J. L. Margot, D. Vokrouhlický, D. J. Scheeres, P. Pravec, S. C. Lowry, A. Fitzsimmons, M. C. Nolan, S. J. Ostro, L. A. M. Benner, J. D. Giorgini, and C. Magri. Spin Rate of Asteroid (54509) 2000 PH5 Increasing Due to the YORP Effect. *Science*, 316:274–, April 2007. doi: 10.1126/science.1139038.

D. J. Tholen. *Asteroid taxonomy from cluster analysis of Photometry*. PhD thesis, Arizona Univ., Tucson., September 1984.

C. A. Thomas, D. E. Trilling, J. P. Emery, M. Mueller, J. L. Hora, L. A. M. Benner, B. Bhattacharya, W. F. Bottke, S. Chesley, M. Delbó, G. Fazio, A. W. Harris, A. Mainzer, M. Mommert, A. Morbidelli, B. Penprase, H. A. Smith, T. B. Spahr, and J. A. Stansberry. ExploreNEOs. V. Average Albedo by Taxonomic Complex in the Near-Earth Asteroid Population. *AJ*, 142:85, September 2011. doi: 10.1088/0004-6256/142/3/85.

R. A. Werner and D. J. Scheeres. Exterior Gravitation of a Polyhedron Derived and Compared with Harmonic and Mascon Gravitation Representations of Asteroid 4769 Castalia. *Celestial Mechanics and Dynamical Astronomy*, 65:313–344, 1997.

R. J. Whiteley, Jr. *A compositional and dynamical survey of the near-Earth asteroids.* PhD thesis, University of Hawai'i at Manoa, 2001.

G. V. Williams. *Minor Planet Astrophotometry.* PhD thesis, Smithsonian Astrophysical Observatory, September 2012. gwilliams@cfa.harvard.edu.

M. T. Zuber, D. E. Smith, A. F. Cheng, J. B. Garvin, O. Aharonson, T. D. Cole, P. J. Dunn, Y. Guo, F. G. Lemoine, G. A. Neumann, D. D. Rowlands, and M. H. Torrence. The Shape of 433 Eros from the NEAR-Shoemaker Laser Rangefinder. *Science*, 289: 2097–2101, September 2000. doi: 10.1126/science.289.5487.2097.

CHAPTER 2

Radar imaging and characterization of Binary

Near-Earth Asteroid (185851) 2000 DP107

(S. P. Naidu, J. L. Margot, M. W. Busch, P. A. Taylor, M. C. Nolan, M. Brozovic, L. A. M.
Benner, J. D. Giorgini, C. Magri, in preparation)

2.1 Introduction

2000 DP107 was discovered on 2000 February 29 by the Lincoln Near-Earth Asteroid Re-
search (LINEAR) program at Socorro, New Mexico. Radar observations in October that
year revealed the asteroid to be a binary system (Margot et al., 2002), the first such system
to be imaged in the near-Earth asteroid (NEA) population. Additional radar and photomet-
ric studies showed that $\sim 15\%$ of all NEAs bigger than $200\,\mathrm{m}$ are binary in nature (Pravec
et al., 1999; Margot et al., 2002; Pravec et al., 2006).

The presence of a satellite around the primary gives us an opportunity to secure direct
measurements of several quantities that are not normally measurable. Radar observations
enable measurements of the orbital period and orbital separation, which reveal the total
mass of the binary system through Kepler's third law. In addition, radar observations
enable measurements of the masses of individual components by measuring the distances of
the component centers of mass (COMs) from the system COM. Using this information along
with the shape models of the two components derived from radar images, we can estimate
their densities. These are important constraints for testing models of formation and evolution
of NEAs. Radar observations of 2000 DP107 in 2000 October yielded rough estimates of
masses, sizes, and densities of the 2 components as well as their mutual orbit (Margot et al.,

2002). In 2008 September, the asteroid made another close approach to the Earth and was observed at ~ 0.05 astronomical units (au) or about 20 lunar distances. Because this was about half the distance of the 2000 encounter (~ 0.11 au), it resulted in data sets with signal-to-noise ratio (SNR) ~ 20 times higher than in 2000. The high SNRs enabled us to derive component shapes with effective resolutions of ~ 50 m on the surface, and estimate the component masses, volumes, and densities more accurately.

In this paper we present detailed component shape models, improved estimates of component masses and densities, and estimates of the mutual orbit parameters using the 2000 and the 2008 radar data. This detailed characterization of 2000 DP107 and its favorable accessibility ($\Delta v \approx 5.9$ km s^{-1}) make it a good candidate for spacecraft rendezvous missions (e.g., Funase et al., 2014).

2.2 Methods

2.2.1 Observing and Data Processing

We observed 2000 DP107 using the Arecibo S-band (2380 MHz, 13 cm) radar and the Goldstone X-band (8560 MHz, 3.5 cm) radar on 10 days between 2008 September 9 and 24, during which the asteroid moved $\sim 60°$ across the sky. It came closest to Earth on September 11 at a distance of 0.057 au. Most of the observing time was dedicated to imaging, with the remainder dedicated to securing continuous wave (CW) spectra. We obtained 335 range-Doppler images and 65 continuous wave (CW) spectra using Arecibo and 534 range-Doppler images and 67 CW spectra using Goldstone.

Radar observations were carried out according to the methods described in Naidu et al. (2013). Briefly, radar imaging was carried out by transmitting a repeating pseudo-random code modulated over a circularly polarized carrier wave, using a binary phase shift keying scheme (Proakis and Salehi, 2007). In each *run*, the waveform was transmitted for approximately the round-trip light-time before switching over to the receiver. The received signal was demodulated and then decoded by cross-correlating it with a replica of the transmitted

Table 2.1.   Radar Observations of (185851) 2000 DP107

Tel	UT Date yyyy-mm-dd	MJD	Eph	RTT s	PTX kW	SNR	Baud μs	Prim. res. Hz	Sec. res. Hz	Code	Start-Stop hhmmss-hhmmss	Runs
G	2008-09-09	54718	85	59	445		1.0			127	114323-114719	3
			87				1.0			127	121534-152227	96
							cw	1.0		none	153128-154316	7
G	2008-09-10	54719	89	58	445		cw	1.0		none	100115-100907	5
							0.5			8191	102915-152812	153
							cw	1.0		none	153412-154908	7
A	2008-09-10	54719	89	58	628	2243	cw	0.2		none	101757-102635	5
					611			0.2	0.08	0.04	65535	102829-114008	37
					561	2569	cw	0.2		none	114159-115234	6
A	2008-09-11	54720	89	58	630	1800	cw	0.2		none	094357-095235	5
					616			0.2	0.08	0.04	65535	095452-112810	48
					580	2283	cw	0.2		none	113030-114115	6
G	2008-09-12	54721	89	58	430		cw	1.0		none	095102-100843	10
							0.5		0.04	8191	101952-142936	128
							cw	1.0		none	143725-145705	11
A	2008-09-13	54722	89	59	603	1728	cw	0.2		none	084405-085301	5
							0.2	0.08	0.04	65535	085548-105703	57
					570	1656	cw	0.2		none	105927-110823	5
G	2008-09-13	54722	89	59	432		cw	1.0		none	091304-092304	5
							1.0			8191	103240-124441	67
							cw	1.0		none	125127-131326	12

code, yielding a range resolution equal to the baud length of the transmitted code. In each range bin, consecutive returns were fast Fourier transformed (FFT) to obtain the received signal power as a function of Doppler frequency. The end product is a two-dimensional array or image showing the echo power as a function of range and Doppler frequency. Table 2.1 summarizes our observations. Because of the smaller antenna size and transmitter power, the Goldstone data have much lower SNRs ($\sim 1/20$) compared to the Arecibo data. Six to eight consecutive Goldstone runs were summed incoherently in order to improve the SNR.

43

Table 2.1 (cont'd)

Tel	UT Date yyyy-mm-dd	MJD	Eph	RTT s	PTX kW	SNR	Baud μs	Prim. res. Hz	Sec. res. Hz	Code	Start-Stop hhmmss-hhmmss	Runs
G	2008-09-14	54723	89	60	432		cw	1.0		none	092211-094047	10
							1.0			8191	095318-112614	47
							1.0			8191	114209-130244	40
A	2008-09-15	54724	89	63	~604	1320	cw	0.2		none	075347-080310	5
							0.2	0.08	0.04	65535	080616-102000	56
					585	1444	cw	0.2		none	102236-102952	4
A	2008-09-18	54727	89	70	595	813	cw	0.2		none	065646-070944	6
							0.5	0.24	0.08	8191	071531-092200	54
						828	cw	0.2		none	092751-093340	3
A	2008-09-21	54730	89	81	590	530	cw	0.2		none	060205-061410	5
					624			0.5	0.24	0.08	8191	062313-082654	45
A	2008-09-24	54733	89	93	660	434	cw	0.2		none	052205-053607	5
					680			1.0		8191	053910-073632	38
					605	383	cw	0.2		none	073910-075312	5

Note. — The first column indicates the telescope: Arecibo (A) or Goldstone (G). MJD is the modified Julian date of the observation. Eph is the ephemeris solution number used. RTT is the round-trip light-time to the target. PTX is the transmitter power. SNR is the predicted signal-to-noise ratio per run. Baud and Res are the delay (i.e., range) and frequency (i.e., Doppler) resolutions, respectively, of the processed data. Code is the length of the pseudo-random code used. The time-span of the received data are listed by their UT start and stop times. The last column indicates the number of runs acquired in each configuration.

2.2.2 Mutual Orbit

We used a least squares procedure to fit Keplerian orbits to the positions of the secondary COM with respect to the primary COM, using data from 2000 October and 2008 September. We obtained range-Doppler separations between the primary and secondary COMs using two different techniques. In the first approach we estimated the COM locations in the images by measuring the positions of the leading and trailing edges of the components. In the second approach we relied on shape models obtained with the SHAPE software (Hudson, 1993; Magri et al., 2007) to locate the component COMs. If the shape models are accurate, the second technique can yield superior estimates of the COM positions, and therefore of the mutual orbit parameters. Sections 2.2.3 and 2.2.4 describe shape modeling details.

For the first, edge-based approach, we defined leading edges (LE) and trailing edges (TE)

in the images on the basis of a 3σ signal threshold, where σ is the standard deviation of the background noise. The LE was defined as the first range bin where the object had a signal higher than 3σ whereas the TE was defined as the last range bin where at least half of the pixels along the Doppler extent exceeded the 3σ threshold. The primary and secondary were assumed to be roughly spherical and their radii were estimated from radar images to be roughly 450 m and 150 m respectively. With these assumptions the range coordinates of the component COMs were taken to be 450 m and 150 m behind their respective leading edges. The Doppler coordinates of the COMs were assumed to be located in the middle of the Doppler extent on the trailing edge. Conservative uncertainties of 2-3 times the range and Doppler resolutions were assigned to the range-Doppler separations. The observational basis from the 2000 data for our estimate of the mutual orbit included 2-4 images on each day from September 30 to October 7, or 20 measurement epochs spanning 8 days, yielding 20 range separations and 20 Doppler separations. For the 2008 data set, we measured the component COM separations in 10 Arecibo images on each day of Arecibo observations, and in 6, 3, 6, 2, and 8 Goldstone images on September 9, 10, 11, 12, and 13 respectively, giving us a total of 95 measurement epochs spanning 16 days, or 190 measurements (range and Doppler separations).

For the second, SHAPE-based approach, we used the shape modeling software to locate the component COMs under a uniform density assumption. SHAPE aligns the synthetic radar images derived from the shape models with the observed radar images, and outputs the COM positions used for the alignment with sub-pixel precision. Uncertainties on the order of the image resolution were assigned to the SHAPE-based range and Doppler separations. We computed the COM separations at the same epochs as those used in the edge-based approach.

Since the observed images from 2000 had to be summed over ~ 30 minutes to get sufficient SNR for SHAPE to perform a reliable alignment, there is some smearing in the summed images, mostly due to the rotation of the primary and to small errors in the ephemeris. Errors in the ephemeris used for data acquisition in 2000 cause the COM to drift by ~ 100 m in a 30-minute period, resulting in some range smear in the summed images. This smearing causes

errors in the alignment of the synthetic images with the summed images since the synthetic radar images were generated only at the mid-point of the time interval corresponding to the summed images. Larger uncertainties, on the order of 150 m, were assigned to these separation measurements in order to account for this smearing.

We fit the mutual orbit and component shapes in an iterative manner. Each iteration started with mutual orbit fitting followed by component shape modeling. In the first iteration, we used the edge-based approach to determine preliminary mutual orbits and used the orbit solutions to inform our component shape modeling (Sections 2.2.3 and 2.2.4). For the second iteration, the best-fit component shapes from the first iteration were used to refine the COM separation estimates using the SHAPE-based approach. These improved primary-secondary separation estimates were used to refine the mutual orbit fit.

2.2.3   Primary Shape

We used the SHAPE software (Hudson, 1993; Magri et al., 2007) to invert the sequence of range-Doppler images and CW spectra from 2008 to obtain a 3D shape model for the primary. Our data set consisted of 278 Arecibo range-Doppler images and 95 CW spectra from both Arecibo and Goldstone covering a 16-day period between 2008 September 9 and 24. We left out the low-resolution Goldstone and Arecibo images as they did not improve the quality of the fit and slowed down the shape modeling process. Because we modeled the primary and secondary separately, we vignetted the images and spectra to exclude the contribution of the other component to the echoes.

Shape modeling was generally carried out in three steps. First we fit a triaxial ellipsoid model to the data to get the overall extents of the object. We then moved on to a spherical harmonics model with 8 degrees to fit for the long-wavelength features seen in the images. Finally, in order to fit for the small-scale features, we used a vertex model with 1000 vertices and 1996 triangular facets. In each step weighted penalty functions were used to favor models having uniform density, principal axis rotation, and a reasonably smooth surface. We used

a cosine law to model the radar scattering from the surface of the asteroid:

$$\frac{d\sigma}{dA} = R(C+1)(\cos\alpha)^{2C}. \qquad (2.1)$$

Here σ is the radar cross section, A is the target surface area, R is the Fresnel reflectivity, C is a parameter related to the near-surface roughness of the asteroid at the radar wavelength scales, and α is the incidence angle of the wave. Values of C close to 1 represent diffuse scattering, whereas larger values represent more specular scattering (Mitchell et al., 1996).

Because the minimization procedure in SHAPE is not particularly effective at fitting the spin axis orientation of the shape models, we carried out an extensive grid search for the best-fit spin axis orientation during the ellipsoid and spherical harmonics shape modeling stages. We assumed that the lightcurve period of 2.775 hours (Pravec et al., 2006) provided a good approximation to the sidereal spin period and we fit shape models to the data using spin axis orientations in increments of 15° in ecliptic longitude (λ) and 15° in ecliptic latitude (β). For each case, we performed an ellipsoid model fit followed by a 8-degree spherical harmonics model fit. Only the shape parameters, semi-axes in the ellipsoid fit and spherical harmonic coefficients in the spherical harmonic fit, the initial rotational phase of the object, and the radar scattering parameter R were allowed to change. The spin rate, the spin axis orientation, and the radar scattering parameter C were kept fixed. The grid search was repeated for C=0.6, 0.8, 1.0, and 1.2. We defined a somewhat arbitrary threshold separating acceptable fits from poorer solutions by visually comparing the synthetic and observed images and using a χ^2_ν threshold of 0.6655.

Our mutual orbit pole estimates lie in the region where spin axis orientations were considered acceptable on the basis of the shape model fits. Because we did not obtain a tight constraint on our spin pole using the shape model search, we used the best-fit mutual orbit pole as the preferred spin pole for shape modeling. For a binary formed by a spin-up process one would expect the primary spin pole to be roughly aligned with the mutual orbit pole, and tidal processes are expected to damp any residual inclination. With this spin pole assumption we fit 8-degree spherical harmonics models to the data in the same way as we

did in the grid search. Here we tried values of C ranging from 0.5 to 1.5 in steps of 0.1. As explained in section 2.2.2, the shape modeling was done in tandem with the mutual orbit fits: Mutual orbit fits were followed by shape model fits. In the second/final iteration, we performed the spherical harmonics shape model fit followed by a vertex model fit. At each step, we verified the quality of the fit by visually comparing the synthetic data generated by SHAPE with the corresponding observed data.

For the vertex model fit we used as initial conditions the best-fit spin state and spherical harmonics shape model determined at the previous step. Once again, only the shape parameters (location of the vertices), the initial rotational phase, and the radar scattering parameter R were allowed to change and all the other parameters were kept fixed.

2.2.4 Secondary Shape

Shape modeling of the secondary component was performed using a method similar to the one described in section 2.2.3. The data set for modeling the shape and rotation of the secondary consisted of 180 Arecibo images taken between 2008 September 10 and 15. The images from September 18 and 21 with range resolutions of 75 m, were left out. Although the primary was resolved in these images with 5-6 pixels along the range axis, the secondary was barely resolved and had only about 2 pixels along the range axis. These images did not improve the quality of the secondary shape model fits however they slowed down the shape modeling process significantly. This time it was the primary that was vignetted out of the images. The CW spectra were not used because it is not possible to completely remove the contribution of the primary from the total echo power. We fit an ovoid shape model[1], followed by a 5-degree spherical harmonic model. We then fit a vertex model with 150 vertices and 296 facets.

Periodicities detected in photometric data suggest that the secondary spin period may be close to 1.76 days (Pravec et al., 2006). This can be used as a guide in our shape modeling process, being mindful that lightcurve periods are neither sidereal nor synodic, whereas the

---

[1]An ovoid is a distorted triaxial ellipsoid such that it has a wide and a narrow end.

48

SHAPE software relies on sidereal spin periods. This periodicity is close to the 1.75 day orbital period (Table 2.2), confirming the finding that the secondary is locked in a 1:1 spin-orbit resonance (Margot et al., 2002). We used the radar-derived, sidereal orbital period as the nominal spin period of the secondary for the purpose of shape modeling. Because of the small size and lack of good rotational phase coverage of the secondary, a grid search does not lead to a conclusive result about the spin axis orientation. However for a tidally evolved secondary, one would expect the spin pole to be closely aligned with the mutual orbit pole, so we used the mutual orbit pole as the spin pole of the secondary. This can be verified by computing the obliquity of the Cassini state 1 (Peale, 1969), which is the state towards which tides drive the satellite spin pole. The other cassini states are either unstable or the spin of satellite is unstable at those cassini states (Gladman et al., 1996). The obliquity can be computed by using the following equation derived from (Gladman et al., 1996) for a synchronous secondary:

$$\frac{3}{2}\left(\frac{C - \frac{A+B}{2}}{C}\right)\left[\frac{\sin\theta\cos\theta}{\sin(\theta \pm i)}\right] = \left(\frac{\dot{\Omega}}{\omega}\right). \tag{2.2}$$

Here $A < B < C$ are the the principal moments of inertia of the secondary, θ is the obliquity of the secondary spin pole with respect to the mutual orbit pole, i is the inclination of the mutual orbit with respect to the invariable plane (in this case it is approximately the equatorial plane of the primary), $\dot{\Omega}$ is the precession rate of the mutual orbit, and ω is the spin rate of the secondary. Once the mutual orbit and the primary and the secondary shapes were fit (Sections 2.3.1, 2.3.2, and 2.3.3), we plugged in the relevant values and found that $\theta < 1°$.

The initial rotation phase was set to a value such that the secondary was oriented with its minimum Moment of Inertia (MOI) principal axis pointing towards the primary at pericenter. The same radar scattering law as the one used for the primary was used. We allowed the shape parameters and the radar scattering parameter R to change. The spin rate, the spin axis orientation, and the radar scattering parameter C were kept fixed.

An elongated and synchronous secondary in an eccentric orbit about the primary exhibits librations, which are oscillations about uniform rotation (e.g., Murray and Dermott, 1999).

49

A tidally evolved satellite is expected to exhibit a relaxed-mode libration (Naidu and Margot, 2014), which is equivalent to a forced libration (Murray and Dermott, 1999) when the spin-orbit coupling is negligible. This libration is roughly sinusoidal for small eccentricities and its amplitude as a function of the satellite elongation was estimated by Naidu and Margot (2014) using numerical simulations.

Because the mutual orbit is eccentric and the secondary is elongated, we allowed for the possibility of relaxed-mode libration in longitude in the rotational model. The description of our implementation of the librational model is given in the Appendix (p. 67). We repeated the ovoid and spherical harmonics shape model fits with libration amplitudes ranging from $0°$ to $10°$ in steps of $1°$. We tried all possible libration phases in steps of $4°$ in order to cover the libration phase uncertainty which arises due to an almost circular orbit. The libration amplitudes and phases were held at fixed values in each of these fits.

2.2.5   Mass Ratio, Component Masses, and Densities

The COMs of the two components follow roughly Keplerian orbits around the system COM, while the system COM or barycenter orbits the Sun. The motion of the primary COM relative to the system COM is called the reflex motion of the primary. We estimated the mass ratio of the components and the reflex motion of the primary by quantifying the goodness of fit of heliocentric orbit fits using astrometry of the system COM under various mass ratio assumptions.

The system COM lies on the line joining the component COMs at a distance of d_p from the primary and a distance of d_s from the secondary. The ratio of these distances (d_s/d_p) is equal to the primary-to-secondary mass ratio (M_p/M_s). For a given mass ratio assumption, we calculated the ratio d_s/d_p and estimated the system COM location along the line joining the component COMs in each of the 278 images that were used for shape modeling. This provided a precise estimate of the two-way range to the system COM, where we once again used the SHAPE-based component COMs determined to sub-pixel accuracy. We explored mass ratio assumptions from $M_p/M_s=15$ to 30 in steps of 0.1 to determine the

corresponding two-way ranges to the system COM and assigned uncertainties equal to the range resolution. For each mass ratio assumption we then performed a fit for the heliocentric orbit to all available optical astrometry and the sytem COM ranges. The best overall fit, as indicated by the lowest sum of squares of residuals, yielded an estimate of the actual mass ratio of the system.

We used the mass ratio to apportion the total mass of the system, estimated from the mutual orbit, to the primary and the secondary. These mass estimates were divided by the corresponding component volume estimates, obtained from shape models, to yield component density estimates.

2.2.6 Gravitational Environment

We used the primary shape model and density estimate to compute the gravity field on the surface of the primary. The acceleration on the surface is the vector sum of the gravitational acceleration due to the primary's mass and the centrifugal acceleration due to its spin. An acceleration vector was computed at the center of each facet using the method described in Werner and Scheeres (1997). The angle that the acceleration vector makes with the local inward-pointing surface-normal vector is called the gravitational slope. The gravitational slope corresponding to each acceleration vector was also computed.

2.3 Results

2.3.1 Mutual Orbit

The mutual orbit has a semi-major axis $a = 2.741 \pm 0.08$ km and a sidereal orbital period $P = 1.7565 \pm 0.005$ days. Kepler's third law yields $GM_T = 35.33 \pm 3.00$ m^3 s^{-2}, where G is the gravitational constant and M_T is the total mass of the system. Substituting $G = 6.67 \times 10^{-11}$ m^3 kg^{-1} s^{-2}, we find $M_T = 5.296 \pm 0.45 \times 10^{11}$ kg. Table 2.2 lists the best-fit orbital parameters obtained using the combined 2000 and 2008 data and compares it to the values published in Margot et al. (2002). The values from both works are consistent with

Table 2.2. Mutual orbit parameters for 2000 DP107

Parameter	Value from Margot et al. (2002)	Value from this work
Semi-major axis (km)	2.62 ± 0.16	2.742 ± 0.08
Period (days)	1.755 ± 0.007	1.7565 ± 0.005
Eccentricity	0.01 ± 0.01	0.015 ± 0.01
System mass ($\times 10^{11}$kg)	4.6 ± 0.5	5.296 ± 0.45
Longitude of pericenter ($°$)	10 ± 27	188.4 ± 5
Inclination ($°$)	17 ± 7	-34.3 ± 5
Argument of Pericenter ($°$)	7 ± 39	-39.3 ± 5
Pericenter passage (MJD)	51820.475 ± 0.3	51810.598 ± 0.3
Reduced χ^2	0.32	0.208

each other.

2.3.2 Primary Shape and Spin State

The result of our grid search for the best-fit spin pole is illustrated in Figure 2.1, which shows a contour plot of the χ^2_ν values of the shape model fits for various orientations of the spin pole. Figure 2.1 shows the result for $C = 0.8$, which gave lower overall χ^2_ν values than the other values of C that we tried. However the general χ^2_ν patterns are similar irrespective of the value of C.

As explained in section 2.2.3, we assumed the spin pole to be aligned with the mutual orbit pole at $\lambda = 294°$ and $\beta = 78°$. At this stage, $C = 0.7$ yielded the shape model with the lowest χ^2_ν. Figure 2.2 shows the vertex shape model produced under this assumption, Table 2.3 lists the associated parameters, and Figure 2.3 shows examples of the observed images and the fits using this model. The model shows very good agreement with the data, however minor disagreements are observed. The primary is roughly spheroidal and is assumed to be spinning in principal axis mode (spin axis aligned with the highest moment of inertia axis). A penalty function was used to impose this assumption on the shape model. The χ^2_ν's of the shape model with and without this penalty function are identical (0.66083 and 0.66075 respectively), indicating that they are equally good fits. If the primary spin deviated significantly from the principal axis, imposing the penalty function would have led to a significantly higher χ^2_ν.
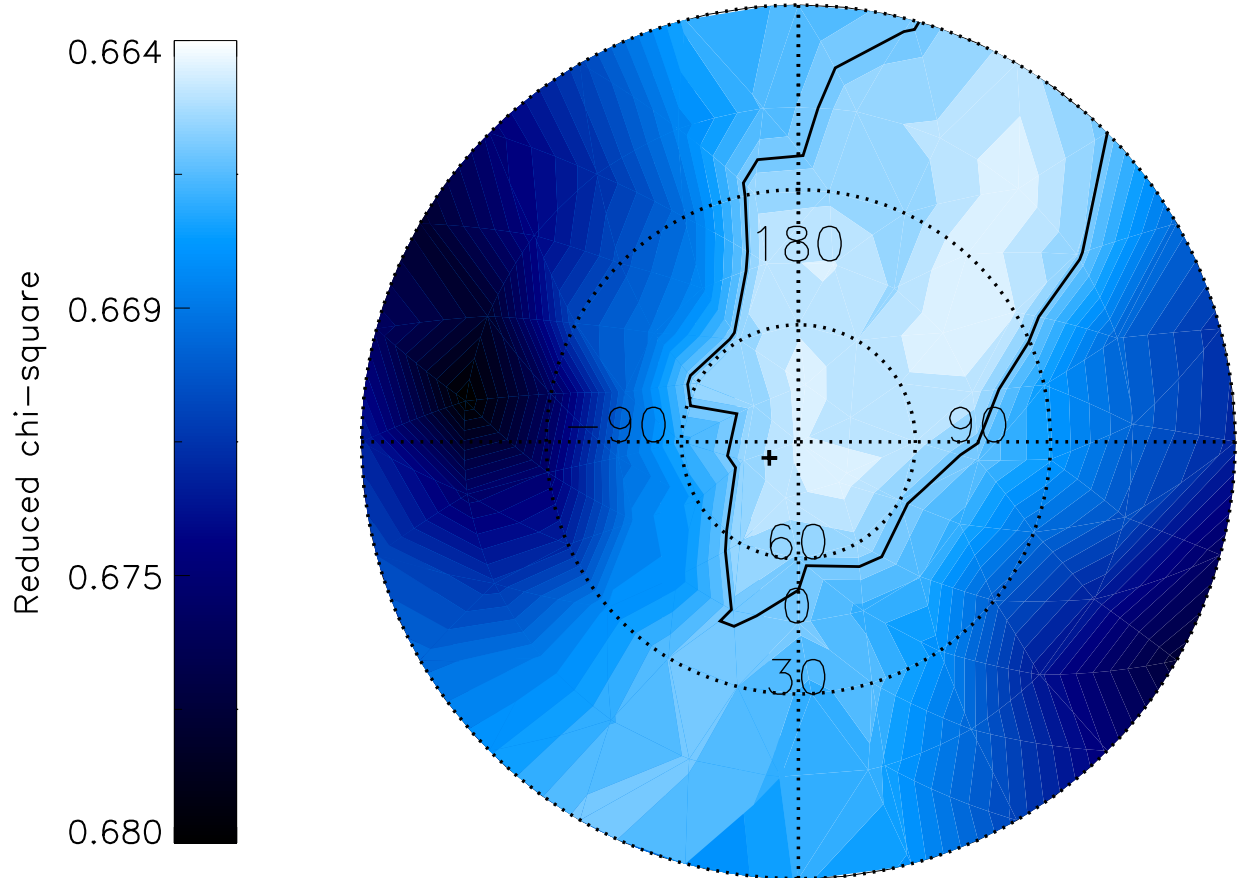
Figure 2.1: Contour plot of goodness of fit (χ^2_ν) of shape models with different spin axis orientations on a polar stereographic projection of the celestial sphere, looking down the ecliptic North. Numbers indicate ecliptic longitudes (λ) and latitudes (β). Region enclosed by solid black contour line ($\chi^2_\nu = 0.6655$) shows acceptable shape model fits. Plus sign shows our mutual orbit pole estimate.
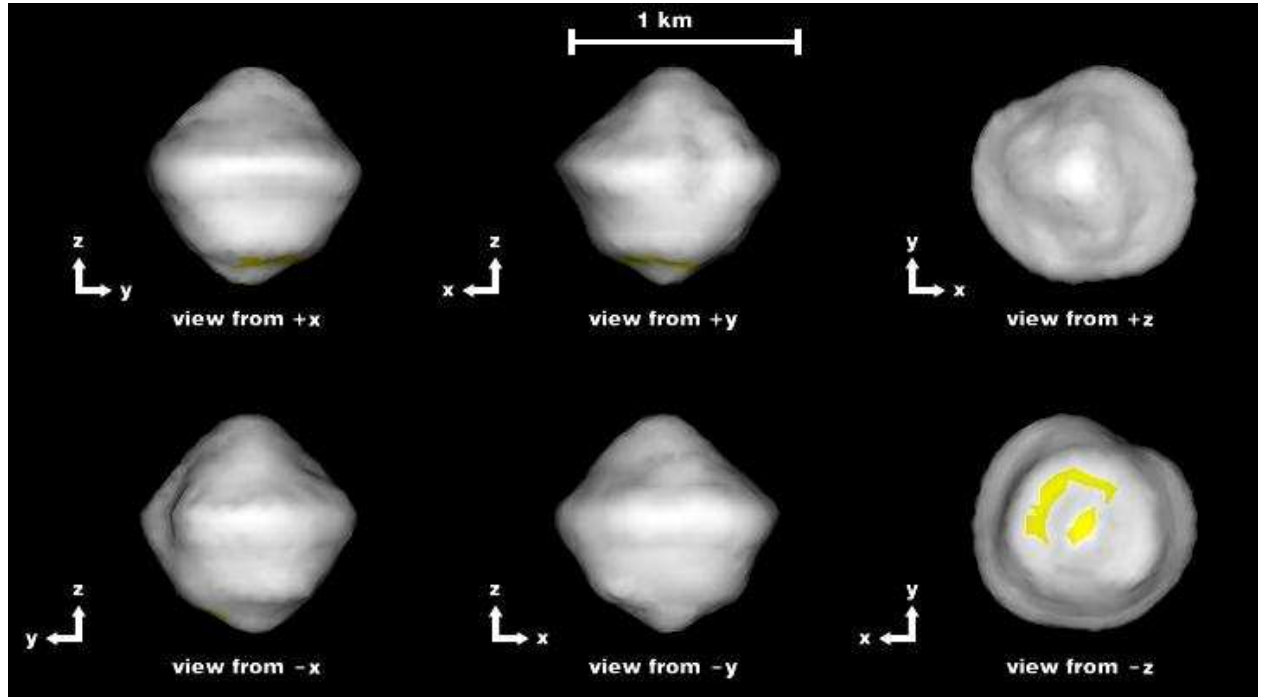
Figure 2.2: Vertex shape model of the primary as seen along the three principal axes x, y, and z. For principal axis rotation the spin axis is aligned with the z axis. Yellow regions have radar incidence angles $> 60°$ and hence are not well constrained. The shape model has 1000 vertices and 1996 triangular facets. The effective surface resolution is ~ 55 m.

The lightcurve period of 2.775 hours (Pravec et al., 2006) is consistent with the rotational phases observed in images of the primary. An equatorial ridge similar to the one found on the 1999 KW4 primary (Ostro et al., 2006) is clearly seen. However, the ridge is not as regular and has a ~ 300 meter concavity on one side.

The shape model shows another ridge-like structure forming a ring around the south pole. This feature produces some of bright features seen behind the leading edge of the object in the radar images (e.g., Figure 2.3 images 5, 6, 7).

2.3.3 Secondary Shape

We found that including longitudinal libration in the secondary spin model did not improve the shape model fits significantly, so we adopted the shape model fit with no libration as the nominal shape model. The lack of a detection may be due to: 1) The amplitude of libration may be too small to be detectable. The relaxed-mode libration amplitude estimated by

Table 2.3. Primary and secondary shape model parameters

Parameters		Primary	Secondary
Extents along	x	$0.992 \pm 6\%$	$0.379 \pm 6\%$
principal axes (km)	y	$0.950 \pm 6\%$	$0.334 \pm 6\%$
	z	$0.951 \pm 6\%$	$0.270 \pm 6\%$
Surface area (km^2)		$2.496 \pm 12\%$	$0.329 \pm 12\%$
Volume (km^3)		$0.342 \pm 18\%$	$0.017 \pm 18\%$
Moment of inertia ratios	A/C	$0.915 \pm 10\%$	$0.708 \pm 10\%$
	B/C	$0.950 \pm 10\%$	$0.888 \pm 10\%$
Equivalent diameter (km)		$0.867 \pm 6\%$	$0.316 \pm 6\%$
DEEVE extents (km)	x	$0.904 \pm 6\%$	$0.377 \pm 6\%$
	y	$0.874 \pm 6\%$	$0.314 \pm 6\%$
	z	$0.827 \pm 6\%$	$0.268 \pm 6\%$
Spin pole (λ, β) (°)		$(294, 78) \pm 10$	$(294, 78) \pm 10$

Note. — The shape model of the primary consists of 1000 vertices and 1996 triangular facets, corresponding to an effective surface resolution of ~ 57 m. The shape model of the secondary consists of 150 vertices and 296 facets; it has an effective surface resolution of ~ 52 m. The moment of inertia ratios were calculated assuming homogeneous density. A, B, and C are the principal moments of inertia, such that $A < B < C$. Equivalent diameter is the diameter of a sphere having the same volume as that of the shape model. A dynamically equivalent equal volume ellipsoid (DEEVE) is an ellipsoid with uniform density having the same volume and moment of inertia ratios as the shape model. The spin poles are assumed to be aligned with the mutual orbit pole. Surface area is the surface area of the shape model.
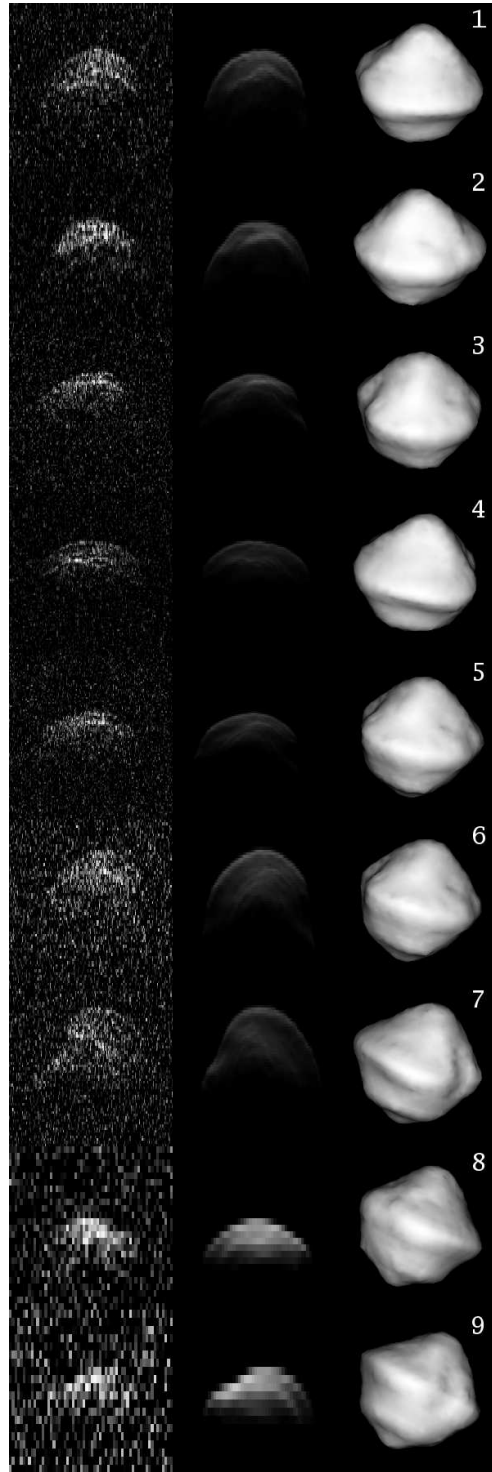
Figure 2.3: Examples of images and fits for the primary. Each row (from left to right) shows the observed image, the corresponding synthetic image generated using the shape model, and the corresponding plane of sky (POS) view of the shape model. The images were obtained on (from top to bottom) September 10, 10, 11, 11, 13, 15, 15, 18, 21.

Naidu and Margot (2014) corresponds to a surface displacement of ~ 15 m, which is the finest range resolution of the dataset. 2) The temporal coverage of the secondary may not be sufficient to enable the detection of librations. Radar images are available only on 4 epochs and they do not cover all sub-observer longitudes.

Figure 2.5 shows the best-fit secondary vertex shape model, Table 2.3 lists the shape model parameters, and Figure 2.4 shows some examples of the observed images and the fits using this model. There is good agreement between the model and the data but minor differences are seen. The secondary has a triangular pole-on-silhouette with Dynamically Equivalent Equal Volume Ellipsoid (DEEVE) dimensions of $377 \times 314 \times 268$ m. A spin rate that is equal to the mutual orbit mean motion and an orientation such that the longest principal-axis of the secondary points towards the primary on average are consistent with the radar data. The spin pole of the secondary is assumed to be aligned with the mutual orbit pole.

2.3.4 Mass Ratio, Component Masses and Densities

Direct estimation of the mass ratio using the method described in section 2.2.5 yielded a mass ratio (M_p/M_s) of 26.2 ± 2. This mass ratio corresponds to a reflex motion of the primary of 101 ± 8 m, consistent with the estimate of 140 ± 40 m of Margot et al. (2002), and with the apparent motion observed directly in the images. Figure 2.6 shows a plot of the χ^2 values of the heliocentric orbit fits to the optical and radar astrometry. The latter uses two-way ranges to the system COM as determined under various mass ratio assumptions. Using this mass ratio we can apportion the total mass of the system (M_T) to the two components. We find the mass of the primary and the secondary to be $5.101 \pm 0.44 \times 10^{11}$ kg and $0.195 \pm 0.024 \times 10^{11}$ kg, respectively. Dividing the masses by the volumes of the corresponding shape models, we find densities for the primary and secondary to be 1491 ± 268 kg m^{-3} and 1147 ± 235 kg m^{-3}, respectively. The densities are similar, pointing towards a similar composition and porosity.
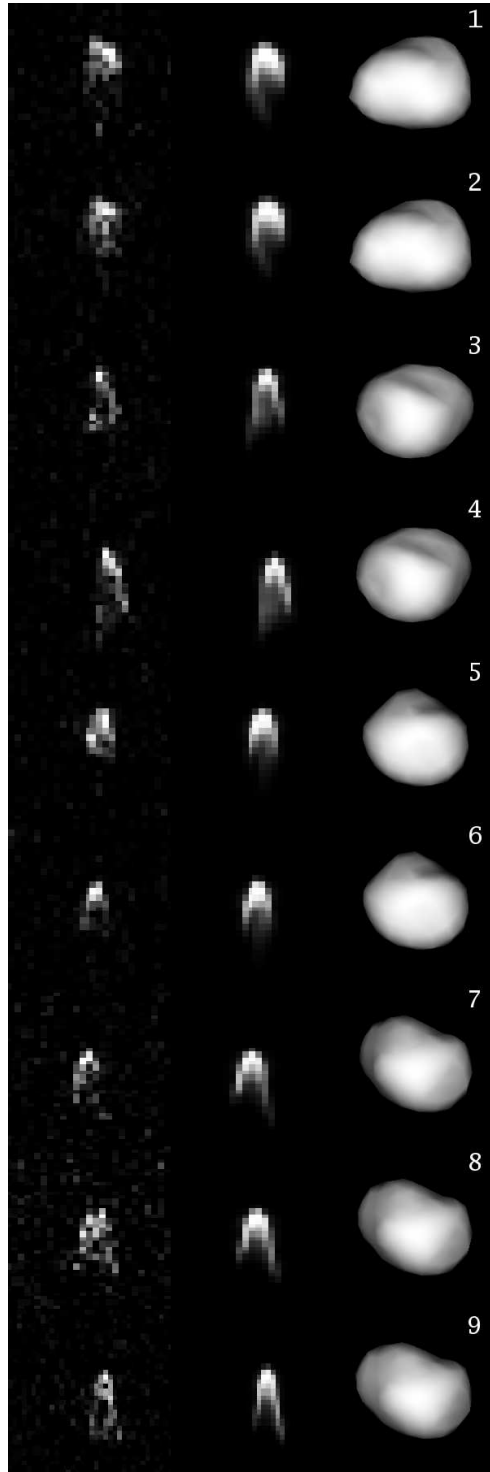
Figure 2.4: Examples of images and fits for the secondary. Each row (from left to right) shows the observed image, the corresponding synthetic image generated using the shape model, and the corresponding plane of sky (POS) view of the shape model. The images were obtained on (from top to bottom) September 10, 10, 11, 11, 13, 13, 15, 15, and 15.
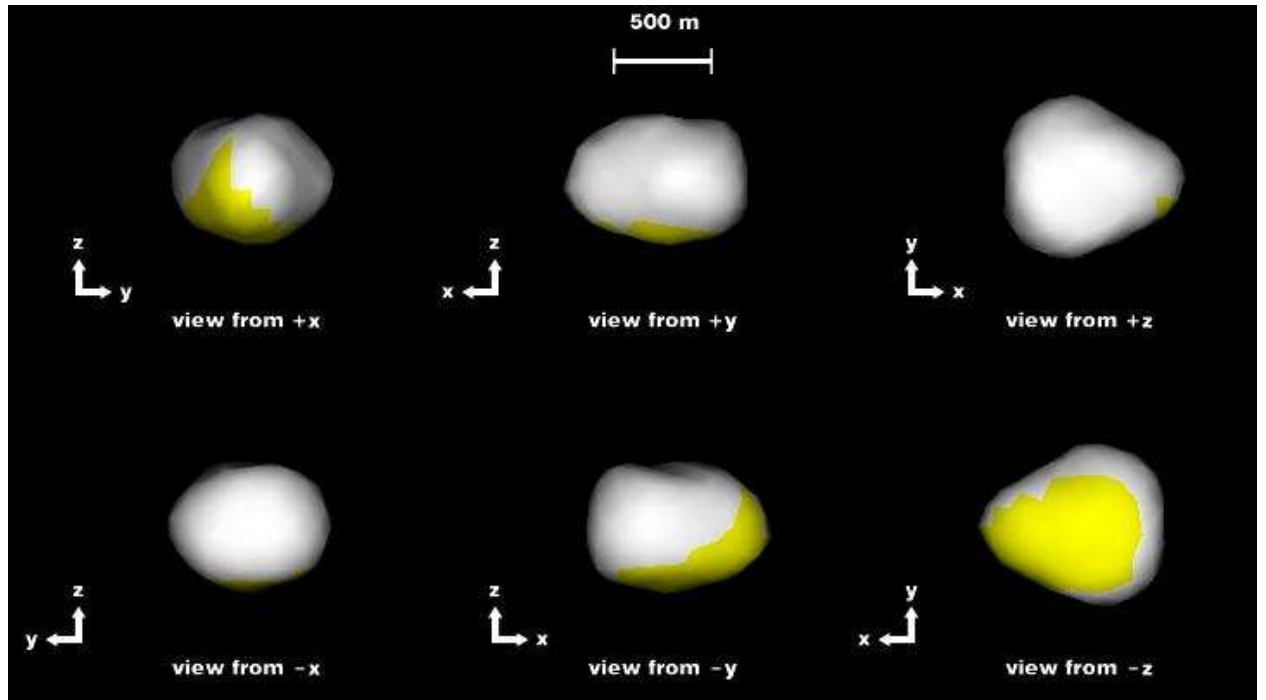
Figure 2.5: Secondary shape model as seen along the three principal axes. Top right view is along the positive spin axis. Yellow regions have radar incidence angles $> 60°$ and hence are not well constrained. The shape model has 150 vertices and 296 triangular facets. The effective surface resolution is ~ 52 m.
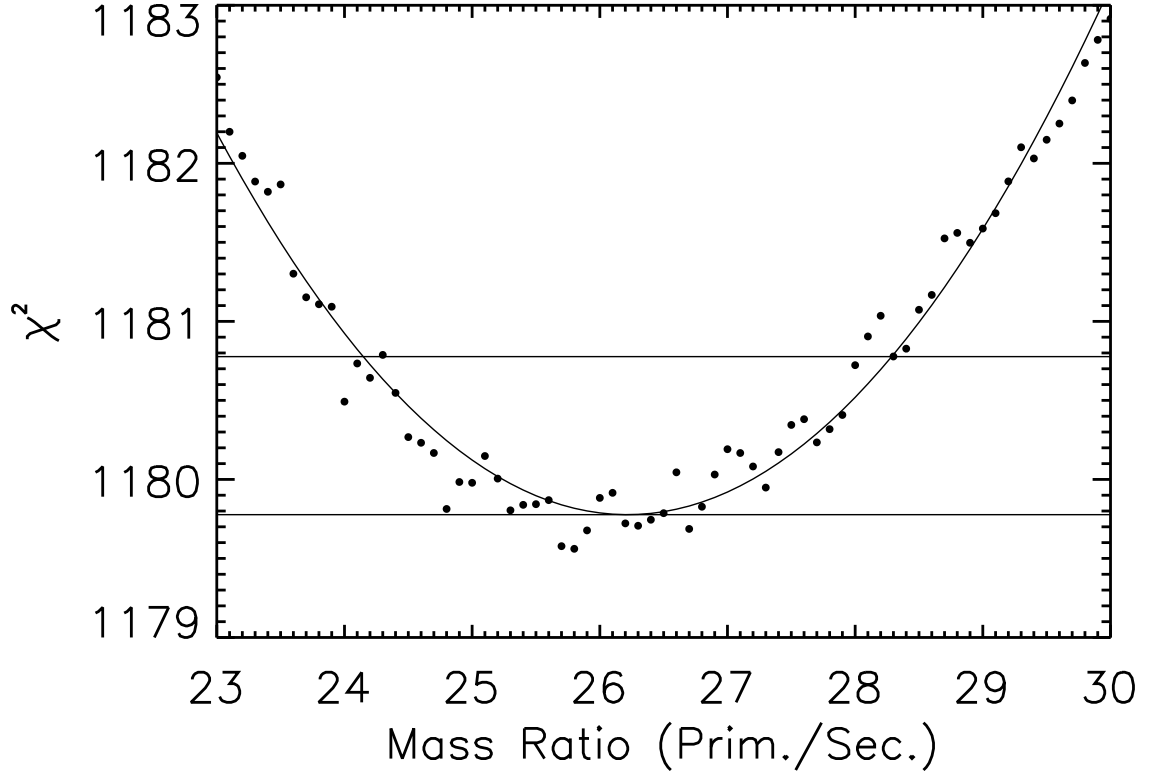
Figure 2.6: Points show χ^2 values of heliocentric orbit fits to optical and radar astrometric observations. Radar astrometry includes two-way ranges to the system COM under various mass ratio assumptions. Solid curve shows the best fit parabola to the χ^2's. The horizontal lines show the minimum χ^2 on the parabola and the χ^2 corresponding to the 1σ uncertainty, respectively. The minimum χ^2 corresponds to a primary-to-secondary mass ratio of 26.2 ± 2.
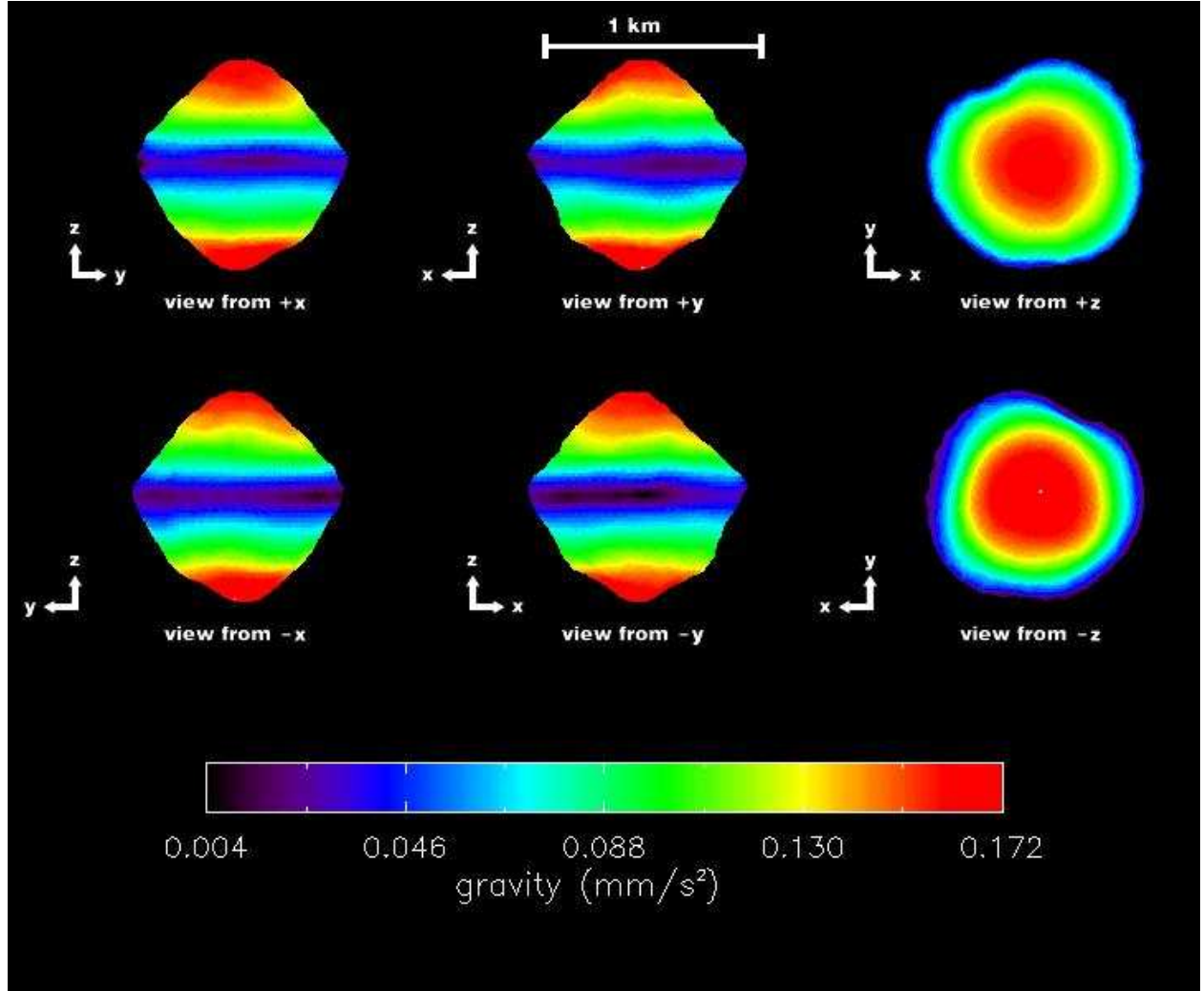
Figure 2.7: This figure shows the magnitudes of the vector sum of accelerations due to gravity and centrifugal accelerations computed at the centers of the facets of the primary shape model. We assumed a uniform density of 1491 kg m^{-3}, which was obtained in section 2.3.4, and a spin period of 2.775 hours. At the equator, these values are close to zero, indicating that the magnitude of centrifugal acceleration is almost equal to the magnitude of acceleration due to the asteroid's mass.
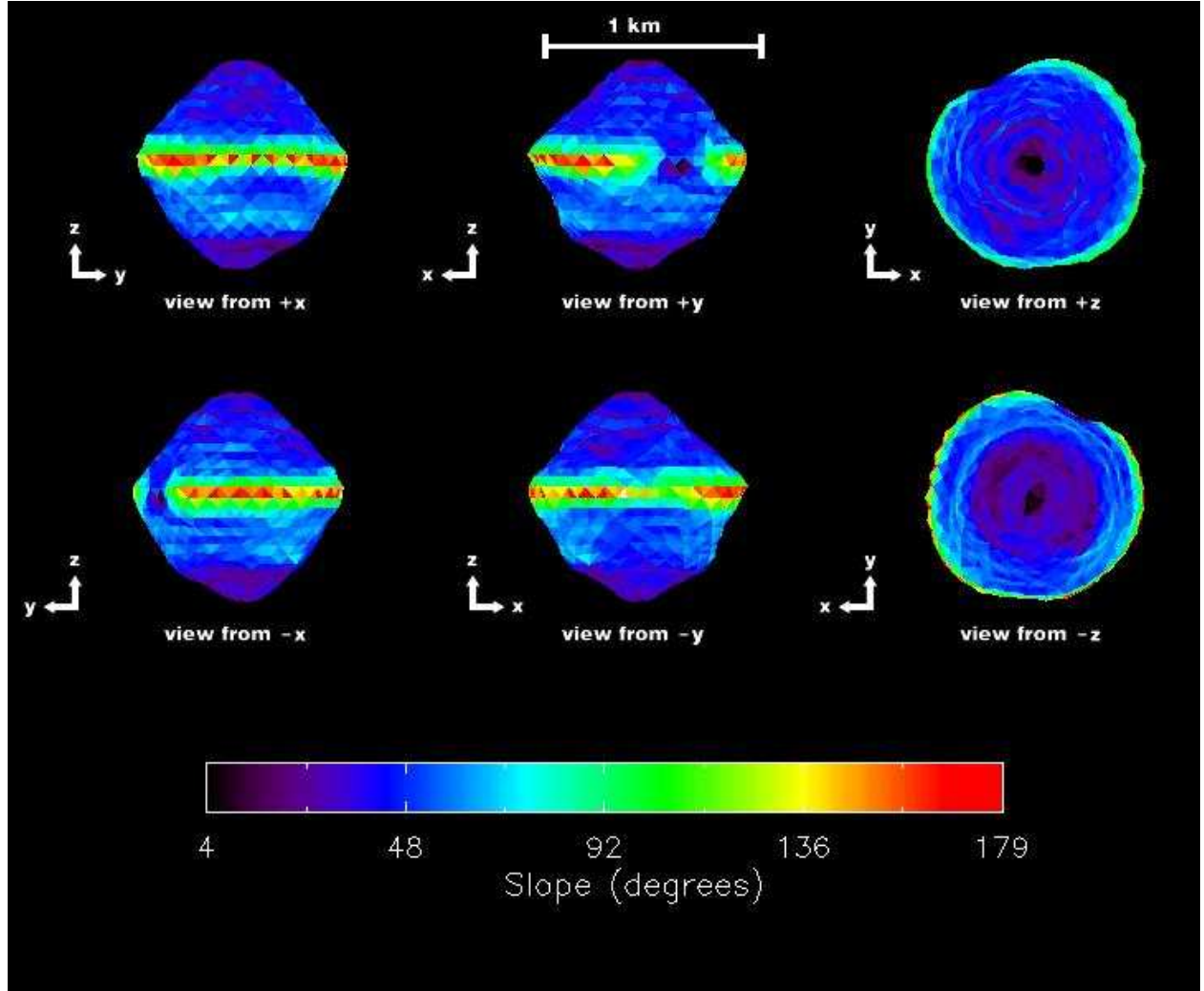
Figure 2.8: This figure shows the gravitational slopes computed at the centers of the facets of the primary shape model. We assumed a uniform density of 1491 kg m^{-3}, obtained in section 2.3.4, and a spin period of 2.775 hours. Slopes vary from $\sim 0°$ at the poles and equator to $\sim 180°$ at some regions at the equator. Most regions at mid-latitudes have slopes between 40° and 60°.

62

2.3.5 Primary Gravitational Environment

The acceleration map on the surface of the primary shape model shows that, for nominal values of mass, spin period, and shape parameters, the net acceleration on the equatorial ridge is very close to zero (Fig 2.7), which implies that the centrifugal acceleration on the ridge almost cancels out the acceleration due to the primary's mass. As we move to higher latitudes, and hence closer to the spin axis, the magnitude of the centrifugal acceleration decreases, causing the magnitude of the net acceleration to increase and reach values up to 172 μm s^{-2} at the poles. This value is about 2×10^{-5} times that on Earth.

The gravitational slopes near the poles are close to zero (Figure 2.8). Around the mid-latitudes, the slopes are higher and most regions here have values between 40° and 60°. Regions on the equatorial ridge have slopes close to 180°, implying that the magnitude of centrifugal acceleration is greater than the magnitude of acceleration due to mass. Inside the concavity on the equatorial ridge the slopes are close to 0°. These slopes provide clues to the mechanical properties of the asteroid material. The implications are discussed in section 2.4.

2.4 Discussion

2.4.1 Primary shape and gravitational environment

The primary shape is similar to shapes of some other radar-characterized asteroids such as 1999 KW4, 1994 CC, 2008 EV5, Bennu, etc. (Ostro et al., 2006; Brozović et al., 2011; Busch et al., 2011; Nolan et al., 2013, respectively). This commonly observed top-shaped structure is an indication that the asteroid has undergone reshaping, most likely due to the spin-up of the primary (e.g., Harris et al., 2009). The shape and the gravitational field provide clues about the mechanical properties of the material of the primary. Figure 2.8 shows that the gravitational slopes around the mid-latitudes are mostly between 40° and 60°. Some of these values are greater than the angle of repose of sand on Earth which has values between 30° and 50°. A possible explanation of such high angles is that cohesive van der Waals forces between the particles play an important role on the surfaces of the asteroids as proposed

by Scheeres et al. (2010). These cohesive forces could be comparable in magnitude to the ambient gravitational force (Scheeres et al., 2010), resulting in much higher effective angles of repose that the material can sustain (e.g., Rognon et al., 2008). Figure 2.8 shows that slopes at the equator of the primary are $> 90°$, implying that centrifugal force is greater than the gravitational pull at the equator. In the absence of other forces, this imbalance will cause material to escape from the primary at the equator. Cohesion between particles could balance the excess centrifugal force and prevent such an escape. Nevertheless, the regions in the mid-latitudes having the highest slopes might be devoid of fine grained material, as the material would slide off to lower potential areas. Some of the regions on the equatorial ridge with slopes close to 180° might also be paths through which material is shed off from the primary. The slope values are sensitive to the size, the density, and the spin period of the asteroid. Scaling down the asteroid by $\sim 4\%$, which is within the size uncertainty of 5%, and keeping the mass unchanged (effectively increasing its density by $\sim 16\%$) yields slopes close to zero on most regions at the equator and slopes lower than 40° on most of the surface of the asteroid. If tides and/or YORP spin down the asteroid, there will be a global decrease in the slopes. A similar spin down might have led to the overall low slopes seen on 2008 EV5 (Busch et al., 2011).

Assuming a grain density of 3000 kg m^{-3}, the observed densities of the primary and secondary can be explained by $\sim 50\%$ and $\sim 60\%$ porosity, respectively. Dilation of cohesive materials during avalanching flows seen in numerical simulations and laboratory experiments (e.g., Alexander et al., 2006; Rognon et al., 2008) could also explain the high porosity needed to match the low densities of the primary and the secondary.

The equatorial ridge has an approximately 300 m concavity on it. The concavity could just be a void left over after the asteroid attained its current shape or it could be an impact crater. Jacobson and Scheeres (2011a) hypothesized that a secondary fission event can take place during the post-fission dynamics following the binary formation process, and that one of the fragments may impact the primary. Secondary fission refers to the rotational fission of the secondary as it is torqued by spin-orbit coupling while in a chaotic rotation state (Jacobson and Scheeres, 2011a; Naidu and Margot, 2014). Gravitational pull dominates the centrifugal

force in the interior of the concavity, so ponding of fine grained material transported from higher latitudes can be expected inside the crater.

2.4.2 Mutual orbit

The eccentricity of the mutual orbit, $e \approx 0.015$, translates to a variation between the primary-secondary distance of $2ae \approx 81$ m during each orbit. While this variation is detectable in the radar data from 2008, which has a range resolution of 15 m, it is barely detectable in the radar data obtained in 2000, which has a range resolution of 75 m. Our determination of the longitude of pericenter therefore relies on the 2008 data only. Our method does not rule out substantial pericenter precession during 2000-2008. We performed numerical simulations using the method developed by Naidu and Margot (2014) to estimate pericenter precession rates under various gravitational perturbations: the non-spherical mass distribution of the primary causes pericenter precession of about $90°$/year, whereas the non-spherical mass distribution of the secondary contributes about $-15°$/year. The combined effect causes the pericenter to process by about $75°$/year in a prograde direction with respect to the mutual orbit. Additionally, the gravitational perturbations from the Sun cause the pericenter to precess by about $10°$/year. The combined effect of these three gravitational perturbations is a secular apsidal precession rate of about $85°$/year, but there are significant short-term variations in the precession rate, making detection of apsidal precession difficult. Gravitational perturbations from planets and radiative forces from the Sun complicate the dynamics further.

2.4.3 Binary YORP

Binary YORP is a radiative torque which is hypothesized to alter the mutual orbit of synchronous binary systems (Ćuk and Burns, 2005). A synchronous satellite has a fixed leading and trailing side with respect to the direction of its orbital motion, so an asymmetric re-radiation from the surface of the satellite will lead to a net torque on the mutual orbit. A potentially observable signature of such a torqued orbit is a quadratic change in the mean

anomaly of the satellite (McMahon and Scheeres, 2010). Detecting a quadratic change in mean anomaly requires measurements of the mean anomaly on a minimum of 3 widely separated epochs. Additional measurements will be required to model the complicated dynamics described in the previous section. 2000 DP107 is a prime candidate for the detection of binary YORP since it presents repeated opportunities for observations and has already been observed in 2000 and 2008 by radar and in 2000, 2008, 2011, and 2013 by optical telescopes. McMahon and Scheeres (2010) provided a mean anomaly drift rate prediction for 2000 DP107 by scaling the results obtained from the radar-derived shape model of the satellite of 1999 KW4. Those predictions can now be updated using the secondary shape model. Depending on the direction of the binary YORP torque, the mutual orbit could either expand, contract, or remain unchanged. The outcomes of these scenarios were studied in detail by Jacobson and Scheeres (2011a). An expanding mutual orbit could lead to the formation of binary pairs or an asynchronous satellite, whereas a contracting mutual orbit could create a contact binary asteroid (e.g., Taylor and Margot, 2011). A contracting binary YORP torque could also be balanced by an equal and opposite tidal torque implying a binary asteroid in a stable equilibrium as hypothesized by Jacobson and Scheeres (2011b). Future observations of this system may provide a detection of binary YORP evolution.

2.5 Conclusion

The radar observations of 2000 DP107 allowed us to produce shape models of the primary and secondary, estimate their masses and densities, compute the gravitational environment of the primary, and estimate the mutual orbit parameters. The shape model and gravitational environment of the primary provide important clues about the material properties of the asteroid. The shape model of the secondary can be used to estimate the evolution of the mutual orbit under the binary YORP torque. Future radar and photometric observations of the system may provide measurements of the evolution of the mutual orbit.

2.A Libration model

For small amplitudes of forced librations and small orbital eccentricities, the deviation of the secondary orientation from regular circular motion ($\delta\phi$) can be approximated as,

$$\delta\phi \approx A_{lib} \sin\left[\omega(t - t_0) + \pi\right], \tag{2.3}$$

where A_{lib} is the amplitude of the forced librations, ω is the forcing frequency which is equal to the mean orbital motion ($n = 2\pi/P$), and t_0 is the time of pericenter passage which we obtained from our mutual orbit determination. The additional phase of π appears because for a synchronous secondary whose natural frequency is smaller than the forcing frequency, the librational phase is expected to be 180° at pericenter (Murray and Dermott, 1999).

Bibliography

Albert W Alexander, Bodhisattwa Chaudhuri, AbdulMobeen Faqih, Fernando J Muzzio, Clive Davies, and M Silvina Tomassone. Avalanching flow of cohesive powders. *Powder Technology*, 164(1):13–21, 2006.

M. Brozović, L. A. M. Benner, P. A. Taylor, M. C. Nolan, E. S. Howell, C. Magri, D. J. Scheeres, J. D. Giorgini, J. T. Pollock, P. Pravec, A. Galád, J. Fang, J.-L. Margot, M. W. Busch, M. K. Shepard, D. E. Reichart, K. M. Ivarsen, J. B. Haislip, A. P. LaCluyze, J. Jao, M. A. Slade, K. J. Lawrence, and M. D. Hicks. Radar and optical observations and physical modeling of triple near-Earth Asteroid (136617) 1994 CC. *Icarus*, 216:241–256, November 2011. doi: 10.1016/j.icarus.2011.09.002.

M. W. Busch, S. J. Ostro, L. A. M. Benner, M. Brozovic, J. D. Giorgini, J. S. Jao, D. J. Scheeres, C. Magri, M. C. Nolan, E. S. Howell, P. A. Taylor, J.-L. Margot, and W. Brisken. Radar observations and the shape of near-Earth ASTEROID 2008 EV5. *Icarus*, 212:649–660, April 2011. doi: 10.1016/j.icarus.2011.01.013.

M. Ćuk and J. A. Burns. Effects of thermal radiation on the dynamics of binary NEAs. *Icarus*, 176:418–431, August 2005. doi: 10.1016/j.icarus.2005.02.001.

Ryu Funase, Hiroyuki Koizumi, Shinichi Nakasuka, Yasuhiro Kawakatsu, Yosuke Fukushima, Atsushi Tomiki, Yuta Kobayashi, Junichi Nakatsuka, Makoto Mita, Daisuke Kobayashi, et al. 50kg-class deep space exploration technology demonstration micro-spacecraft procyon. 2014.

B. Gladman, D. D. Quinn, P. Nicholson, and R. Rand. Synchronous Locking of Tidally Evolving Satellites. *Icarus*, 122:166–192, July 1996. doi: 10.1006/icar.1996.0117.

A. W. Harris, E. G. Fahnestock, and P. Pravec. On the shapes and spins of rubble pile asteroids. *Icarus*, 199:310–318, February 2009. doi: 10.1016/j.icarus.2008.09.012.

S. Hudson. Three-dimensional reconstruction of asteroids from radar observations. *Remote Sensing Reviews*, 8:195–203, 1993.

S. A. Jacobson and D. J. Scheeres. Dynamics of rotationally fissioned asteroids: Source of observed small asteroid systems. *Icarus*, 214:161–178, July 2011a. doi: 10.1016/j.icarus.2011.04.009.

S. A. Jacobson and D. J. Scheeres. Long-term Stable Equilibria for Synchronous Binary Asteroids. *ApJ*, 736:L19, July 2011b. doi: 10.1088/2041-8205/736/1/L19.

C. Magri, S. J. Ostro, D. J. Scheeres, M. C. Nolan, J. D. Giorgini, L. A. M. Benner, and J. L. Margot. Radar observations and a physical model of Asteroid 1580 Betulia. *Icarus*, 186:152–177, January 2007. doi: 10.1016/j.icarus.2006.08.004.

J. L. Margot, M. C. Nolan, L. A. M. Benner, S. J. Ostro, R. F. Jurgens, J. D. Giorgini, M. A. Slade, and D. B. Campbell. Binary Asteroids in the Near-Earth Object Population. *Science*, 296:1445–1448, May 2002. doi: 10.1126/science.1072094.

J. McMahon and D. Scheeres. Detailed prediction for the BYORP effect on binary near-Earth Asteroid (66391) 1999 KW4 and implications for the binary population. *Icarus*, 209:494–509, October 2010. doi: 10.1016/j.icarus.2010.05.016.

D. L. Mitchell, S. J. Ostro, R. S. Hudson, K. D. Rosema, D. B. Campbell, R. Velez, J. F. Chandler, I. I. Shapiro, J. D. Giorgini, and D. K. Yeomans. Radar Observations of Asteroids 1 Ceres, 2 Pallas, and 4 Vesta. *Icarus*, 124:113–133, November 1996. doi: 10.1006/icar.1996.0193.

C.D. Murray and S.F. Dermott. *Solar System Dynamics*. Cambridge University Press, 1999. ISBN 9780521572958. URL `http://books.google.co.uk/books?id=NY9iQgAACAAJ`.

S. P. Naidu and J.-L. Margot. Near-Earth Asteroid Satellite Spins Under Spin-Orbit Coupling. *ArXiv e-prints*, September 2014.

S. P. Naidu, J.-L. Margot, M. W. Busch, P. A. Taylor, M. C. Nolan, M. Brozovic, L. A. M. Benner, J. D. Giorgini, and C. Magri. Radar imaging and physical characterization of near-Earth Asteroid (162421) 2000 ET70. *Icarus*, 226:323–335, September 2013. doi: 10.1016/j.icarus.2013.05.025.

M. C. Nolan, C. Magri, E. S. Howell, L. A. M. Benner, J. D. Giorgini, C. W. Hergenrother, R. S. Hudson, D. S. Lauretta, J.-L. Margot, S. J. Ostro, and D. J. Scheeres. Shape model and surface properties of the OSIRIS-REx target Asteroid (101955) Bennu from radar and lightcurve observations. *Icarus*, 226:629–640, September 2013. doi: 10.1016/j.icarus.2013.05.028.

S. J. Ostro, J. L. Margot, L. A. M. Benner, J. D. Giorgini, D. J. Scheeres, E. G. Fahnestock, S. B. Broschart, J. Bellerose, M. C. Nolan, C. Magri, P. Pravec, P. Scheirich, R. Rose, R. F. Jurgens, E. M. De Jong, and S. Suzuki. Radar Imaging of Binary Near-Earth Asteroid (66391) 1999 KW4. *Science*, 314:1276–1280, November 2006. doi: 10.1126/science.1133622.

S. J. Peale. Generalized Cassini's Laws. *AJ*, 74:483, April 1969. doi: 10.1086/110825.

P. Pravec, M. Wolf, and L. Šarounová. How many binaries are there among the near-Earth asteroids? In J. Svoren, E. M. Pittich, and H. Rickman, editors, *IAU Colloq. 173: Evolution and Source Regions of Asteroids and Comets*, page 159, 1999.

P. Pravec, P. Scheirich, P. Kušnirák, L. Šarounová, S. Mottola, G. Hahn, P. Brown, G. Esquerdo, N. Kaiser, Z. Krzeminski, D. P. Pray, B. D. Warner, A. W. Harris, M. C. Nolan, E. S. Howell, L. A. M. Benner, J. L. Margot, A. Galád, W. Holliday, M. D. Hicks, Y. N. Krugly, D. Tholen, R. Whiteley, F. Marchis, D. R. Degraff, A. Grauer, S. Larson, F. P. Velichko, W. R. Cooney, R. Stephens, J. Zhu, K. Kirsch, R. Dyvig, L. Snyder, V. Reddy, S. Moore, Š. Gajdoš, J. Világi, G. Masi, D. Higgins, G. Funkhouser, B. Knight, S. Slivan, R. Behrend, M. Grenon, G. Burki, R. Roy, C. Demeautis, D. Matter, N. Waelchli, Y. Revaz, A. Klotz, M. Rieugné, P. Thierry, V. Cotrez, L. Brunetto, and G. Kober. Photometric survey of binary near-Earth asteroids. *Icarus*, 181:63–93, March 2006. doi: 10.1016/j.icarus.2005.10.014.

J.G. Proakis and M. Salehi. *Digital Communications*. McGraw-Hill, 2007. ISBN 9780072957167. URL http://books.google.com/books?id=HroiQAAACAAJ.

P. G. Rognon, J.-N. Roux, M. Naa?M, and F. Chevoir. Dense flows of cohesive granular materials. *Journal of Fluid Mechanics*, 596:21–47, 2008. doi: 10.1017/S0022112007009329.

D. J. Scheeres, C. M. Hartzell, P. Sánchez, and M. Swift. Scaling forces to asteroid surfaces: The role of cohesion. *Icarus*, 210:968–984, December 2010. doi: 10.1016/j.icarus.2010.07.009.

P. A. Taylor and J.-L. Margot. Binary asteroid systems: Tidal end states and estimates of material properties. *Icarus*, 212:661–676, April 2011. doi: 10.1016/j.icarus.2011.01.030.

R. A. Werner and D. J. Scheeres. Exterior Gravitation of a Polyhedron Derived and Compared with Harmonic and Mascon Gravitation Representations of Asteroid 4769 Castalia. *Celestial Mechanics and Dynamical Astronomy*, 65:313–344, 1997.

CHAPTER 3

Near-Earth Asteroid Satellite Spins Under Spin-Orbit Coupling

3.1 Introduction

Binary near-Earth asteroids (NEAs) are numerous in the asteroid population. Both radar and lightcurve data have shown that $\sim 16\%$ of NEAs larger than ~ 200 m diameter have satellites (Pravec et al., 1999; Margot et al., 2002; Pravec et al., 2006). It is now widely accepted that binary NEAs form by a spin-up process (Margot et al., 2002) and that the specific spin-up mechanism is the YORP torque (Rubincam, 2000). Binary NEA systems exhibit interesting post-fission and spin-orbit dynamics (e.g. Ostro et al., 2006; Scheeres et al., 2006; Fahnestock and Scheeres, 2008; McMahon and Scheeres, 2013) that profoundly affect their evolution (e.g. Jacobson and Scheeres, 2011; Fang and Margot, 2012a; Jacobson et al., 2014), but the range of dynamical regimes has not been fully explored.

In this paper, we develop a method for simulating the coupled spin and orbital motions of two rigid bodies with arbitrary mass distributions. This technique is significantly faster than a similar implementation by Fahnestock and Scheeres (2006), because in our implementation the computationally expensive volume integrals over the two bodies are computed only once before the integration, as opposed to once per time step. We use our technique to perform a survey of the dynamics of all well-characterized binary NEA systems and map the range of dynamical behaviors, including the spin configurations of asteroid satellites. These

results provide important insights for modeling the physical properties of binaries and for understanding the long term evolution of the binary systems.

The sample of well-characterized binaries includes all NEA systems with known estimates of system mass, semi-major axis, eccentricity, and component sizes. In practice, only systems observed with radar fall in this class. Over 35 binary NEAs have been observed with radar, but only about ten have sufficient data to yield mutual orbits and component size estimates. We apply our technique to these systems.

Sections 3.2 and 3.3 describe the implementation of our coupled spin-orbit integrator and cover energy and angular momentum conservation properties. Section 3.4 explains different kinds of satellite spin librations and sets up the notation used in subsequent sections. In section 3.5, we examine the spin-orbit coupling effect and compare numerical and analytical estimates of libration amplitudes. Section 3.6 introduces surface of section plots which are used to identify resonant, chaotic, and non-resonant quasi-periodic trajectories. We examine the trajectories and spin configurations of satellites in well-characterized binary and triple near-Earth asteroid systems in section 3.7 and show that large chaotic zones exist in the phase space of known asynchronous satellites. We also compute libration amplitudes for synchronous satellites. We discuss implications of the results in section 3.8.

3.2 Numerical Integration

We numerically investigate the coupled spin and orbital dynamics of two extended rigid objects under their mutual gravitational influence. We neglect the translational motion of the system barycenter and use the 6 first-order differential equations of motion (EOMs) derived by Maciejewski (1995). Here we express these EOMs in the body-fixed frame of the primary:

$$\dot{\boldsymbol{P}} = \boldsymbol{P} \times \boldsymbol{\Omega}_1 - \frac{\partial V}{\partial \boldsymbol{R}}, \qquad\qquad \dot{\boldsymbol{R}} = \boldsymbol{R} \times \boldsymbol{\Omega}_1 + \frac{\boldsymbol{P}}{m},$$

$$\dot{\boldsymbol{\Gamma}}_2 = \boldsymbol{\Gamma}_2 \times \boldsymbol{\Omega}_1 + \boldsymbol{\mu}_2, \qquad\qquad \dot{\boldsymbol{\Gamma}}_1 = \boldsymbol{\Gamma}_1 \times \boldsymbol{\Omega}_1 + \boldsymbol{\mu}_1,$$

$$\dot{S} = S\hat{\Omega}_2 - \hat{\Omega}_1 S, \qquad\qquad \dot{S}_1 = S_1\hat{\Omega}_1. \qquad (3.1)$$

Here $\boldsymbol{R}$ and $\boldsymbol{P}$ are the relative position and linear momentum vectors of the secondary with respect to the primary, respectively, $m = m_p m_s/(m_p + m_s)$ is the reduced mass of the system, where m_p and m_s are the masses of the primary and secondary, respectively, V is the mutual gravitational potential, $\boldsymbol{\mu}$'s are the torque vectors acting on the two components, $\boldsymbol{\Omega}$'s are their angular velocity vectors, and $\boldsymbol{\Gamma}$'s are their angular momentum vectors. Subscripts 1 and 2 denote quantities that refer to the primary and the secondary, respectively. Further, S and S_1 are attitude rotation matrices: the former mapping from the secondary frame to the primary frame, and the latter mapping from the primary frame to the inertial frame. A hat ($\hat{\ }$) symbol above a vector specifies an operator that maps a 3-vector (e.g., $\boldsymbol{v} = [v_x, v_y, v_z]$) to an antisymmetric 3x3 matrix, as follows:

$$\hat{v} = \begin{bmatrix} 0 & -v_z & v_y \\ v_z & 0 & -v_x \\ -v_y & v_x & 0 \end{bmatrix}. \qquad (3.2)$$

The term $\partial V/\partial \boldsymbol{R}$ is the gradient of the mutual gravitational potential, which is the gravitational force (vector) between the two components. All vectors in equations (3.1) are expressed in the body-fixed frame of the primary. However, when computing $\hat{\Omega}_2$, one must express $\boldsymbol{\Omega}_2$ in the body-fixed frame of the secondary.

The gravitational force and torques are computed at each time step according to the method detailed in Ashenberg (2007). They are functions of $\boldsymbol{R}$, S, and the inertia integrals of the two bodies. The inertia integrals encode the mass distribution information of a body

and are of the form:

$$I_{x^p y^q z^r} = \int_B x^p y^q z^r dm, \tag{3.3}$$

where dm is a mass element of body B at body-fixed coordinates (x, y, z) and the integral is a volume integral over the entire body. The body-fixed coordinate system is aligned with the principal axes and its origin is at the center of mass of B. The exponents p, q, and r are either 0 or positive integers, such that $p + q + r > 0$. We use inertia integrals up to fourth order in the integrations, where the order of an inertia integral is given by the sum of exponents, i.e., $p + q + r$. The inertia integrals depend only on the mass distribution of the object and remain constant throughout the integration, so we compute them only once before the integration. At each time step, current values of $\boldsymbol{R}$ and S from the integrator are passed as arguments to the modules that compute force and torques.

Because detailed 3D shape models of both the primary and secondary are generally not available and their density distributions are unknown, we model the primary and secondary as triaxial ellipsoids (semi-axes a, b, and c) with uniform density in this paper. These restrictions can be easily lifted as knowledge progresses. The uniform-density ellipsoid assumption simplifies the computation of inertia integrals (Boué and Laskar, 2009): they are zero for odd p, q, or r, and the non-zero integrals are simple functions of principal moments of inertia. The fourth-order inertia integrals can be found in Boué and Laskar (2009), and the non-zero second-order inertia integrals are listed below:

$$
\begin{aligned}
I_{x^2} &= \int x^2 dm = \frac{(-A + B + C)}{2}, \\
I_{y^2} &= \int y^2 dm = \frac{(A - B + C)}{2}, \\
I_{z^2} &= \int z^2 dm = \frac{(A + B - C)}{2}.
\end{aligned}
\tag{3.4}
$$

Here, $A \leq B \leq C$ are the principal moments of inertia of the object about the x, y, and z axes, respectively.

We use the Cash-Karp method (Cash and Karp, 1990) to integrate equations (3.1). It is a fifth-order Runge-Kutta integrator with adaptive stepsize control which uses an embedded

75

fourth-order Runge-Kutta formula to compute errors. We use the implementation provided by Press et al. (1992) and set the fractional error tolerance to 10^{-15}.

In all simulations, we assume a planar system, i.e., both bodies are in principal axis rotation about their z (shortest) axes and their equatorial planes are aligned with the mutual orbit at all times. We start all simulations at the pericenter of the osculating mutual orbit and with the longest axis of each body pointing towards each other. The system parameters and initial osculating mutual orbital parameters for all simulations are given in Table 3.1.

3.3   Energy and Angular Momentum Conservation

In this section, we describe results of tests designed to evaluate the energy and angular momentum conservation properties of the integrator. Figure 3.1 illustrates a representative test run with the parameters given in the first line of Table 3.1. For this test case, we used triaxial ellipsoids with principal axis half-lengths of $a = 600$, $b = 500$, and $c = 400$ m for the primary, and $a = 252$, $b = 229$, $c = 190$ m for the secondary. The initial spin periods of the primary and the secondary are 2.775 h and 32.59 h, respectively.

The total energy is conserved at a level of 10^{-2} Joules per year, which is about 10^{-11} times the mean orbital energy and less than 10^{-8} times the magnitude of the energy exchanged between the binary components and the mutual orbit.

Angular momentum is conserved at a level of 220 kg m^2 s^{-1} per year, which is less than 10^{-11} times the total angular momentum of the system ($\sim 10^{14}$ kg m^2 s^{-1}) and less than 10^{-8} times the angular momentum exchanged between the component spins and the mutual orbit.

3.4   Notation and Libration Concepts

Figure 3.2 illustrates the various angles used throughout the paper. θ is the angle between the secondary's long axis and the line of apsides of the the osculating mutual orbit, and $\dot{\theta}$ is its time rate of change. If the apsidal precession rate were zero, $\dot{\theta}$ would correspond to
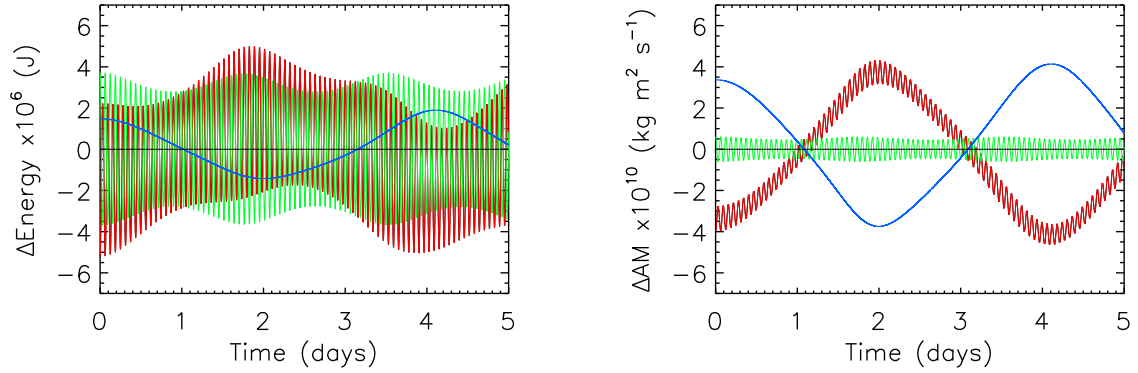
76

Figure 3.1: Energy (top) and angular momentum (bottom) variations over the course of five days for a typical binary NEA (first entry in Table 1). Lines of different colors represent quantities associated with the mutual orbit (red), the primary spin (green), the secondary spin (blue), and the sum of all three (black).

Table 3.1.   Simulation Parameters

Fig.	Object	Primary				Secondary			Mutual Orbit	
		R_p	ρ_p	c	ab	a/b	ω_0	ρ_s	a	e
		m	kg m^{-3}	m	m^2		kg m^{-3}	m		
3.1	Test	493	1581	190	57600	1.10	0.53	2618	3300	0.05
3.3	(1991 VH)[d]	600	1581	190	57600	1.50	1.07	various	3300	0.05
3.4	(1991 VH)[l]	600	1581	190	57600	1.01	0.17	2618	3300	0.05
3.5	(1991 VH)[m]	600	1581	190	57600	1.06	0.42	2618	3300	0.05
3.7	(1991 VH)	600	1581	190	57600	1.50	1.07	2618	3300	0.05
3.8	(2003 YT1)	550	2712	88	11025	1.30	0.88	3248	3930	0.18
3.9	(2004 DC)	180	1461	26	900	1.30	0.88	2000	750	0.30
3.10	(Didymos)	400	1955	65	5625	various	various	2252	1180	0.04
3.10	(2000 DP107)	400	1791	100	22500	various	various	2122	2692	0.03
3.10	(2002 CE26)	1750	966	100	22500	various	various	1454	4870	0.025
3.10	(2001 SN263#1)	1300	996	190	52900	various	various	2320	3800	0.016
3.10	(1994 CC#1)	310	2076	48	3249	various	various	8870	1730	0.002
3.10	(1999 KW4)	659	1970	190	51076	1.30	0.88	3321	2548	0.0004

Note. — Most physical and orbital characteristics of binary and triple NEAs are adopted or derived from Fang and Margot (2012a). Mass and radius uncertainties are ∼10% and ∼20%, respectively. See text for prescription for a, b, and c values. The first column reports the number of the figure illustrating the corresponding results. "Object" indicates the asteroid name or designation. The next two columns list parameters related to the primary: R_p and ρ_p are the equivalent radius and mass density of the primary. The next five columns describe parameters related to the secondary (assumed to be an ellipsoid with semi-axes a, b, and c). With our choice of simulation parameters (Section 3.7), it is convenient to tabulate the quantities c, ab, and the elongation a/b. The fourth parameter describing the secondary, ω_0, is related to the secondary elongation (Refer to section 3.4 for definition). The fifth parameter is the mass density ρ_s. The last two columns give the initial osculating semimajor axis and eccentricity of the mutual orbit. For testing purposes, we use several modified versions of binary NEA 1991 VH: [d] for various densities, [l] for low secondary elongation, [m] for moderate secondary elongation.
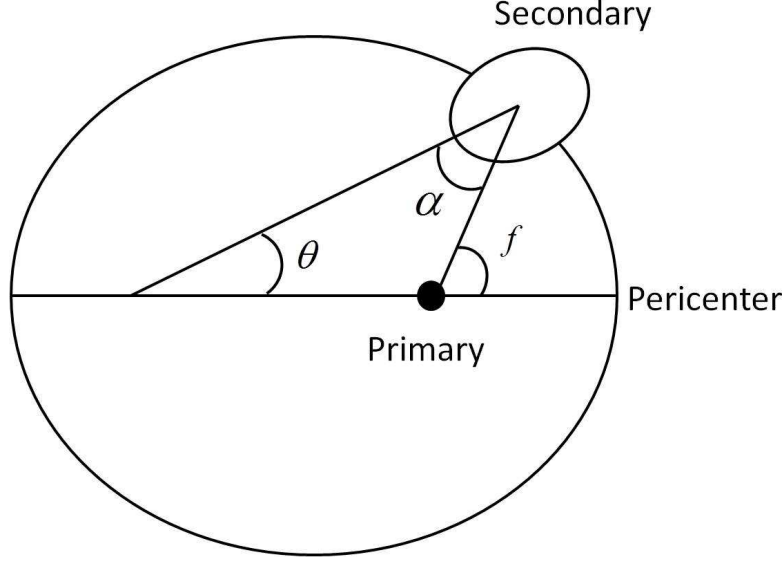
77

Figure 3.2: Illustration of the osculating mutual orbit and notation for angles.

the spin rate of the satellite. The instantaneous values at pericenter are denoted with a subscript p: θ_p, $\dot{\theta}_p$. The angle θ is related to the angle between the satellite's long axis and the primary-secondary line, α, by $\theta + \alpha = f$, where f is the true anomaly of the mutual orbit. At pericenter, $f = 0$, so $\theta_p = -\alpha$.

Oscillations of the secondary orientation with respect to the primary-to-secondary line are called *librations*. In order to illustrate librations, let us first examine a situation in which the amount of angular momentum exchanged between the spin of the secondary and the mutual orbit is negligible. In this situation, we can treat the spin and orbit to be decoupled. A common approach to analyze the spin of the secondary is to assume the secondary to be a triaxial ellipsoid on a fixed Kelperian mutual orbit about a spherical primary. The secondary spin is affected by the gravitational torques exerted by the primary(e.g., Murray and Dermott, 1999). In this situation, the angle α is the sum of *free, forced, and optical* libration angles. *Free libration* is easiest to understand in the case of a circular mutual orbit and a synchronously spinning secondary, i.e., a secondary whose average spin rate is equal to the mutual orbit mean motion. The minimum energy configuration for this system is for the long axis of the secondary to always point towards the primary, such that its instantaneous spin rate is always equal to the mean motion. If the secondary is disturbed

from this configuration, its long axis oscillates about the primary-secondary line due to torques exerted by the primary on the elongated secondary. This oscillation is called free libration and its frequency depends on the shape of the secondary and the mutual orbit parameters. Generally, free libration damps out on short timescales due to tidal friction (Murray and Dermott, 1999).

If the mutual orbit is eccentric, the secondary exhibits optical and forced librations about the primary-secondary line even if the free libration is damped out. *Optical libration* is the torque-free oscillation of the long axis of a uniformly spinning secondary about the primary-secondary line. This oscillation would occur even in the case of a spherical secondary as the orbital velocity varies over the course of the orbit. We use ϕ to represent the component of α that is due to optical librations. The amplitude of optical libration depends only on the shape of the mutual orbit and is $\sim 2e$, where e is the eccentricity of the mutual orbit (Murray and Dermott, 1999). In the case of an elongated secondary, the primary exerts a periodically reversing torque on it due to the misalignment of the secondary long axis from the primary-secondary line, which results in an oscillation of the secondary about uniform rotation called *forced libration*. We use γ to represent the component of α that is due to forced librations. Forced and optical librations have the same frequency (equal to the mean motion). They are in phase if $\omega_0 = \sqrt{3(B-A)/C} < 1$ and 180° out of phase if $\omega_0 > 1$. We use ψ to represent the sum of forced and optical librations, i.e., $\psi = \gamma + \phi$, and ψ_A to represent the libration amplitude.

For most binary near-Earth asteroid systems, a decoupled framework does not accurately capture the system dynamics. Nevertheless, even in the fully coupled problem around an axially symmetric primary, the secondary exhibits libration behavior similar to the free, forced, and optical librations of the decoupled spin problem. There are two modes of libration in the coupled spin-orbit problem, which we call the *relaxed mode* and *excited mode* of libration. The relaxed mode has the same frequency as the orbital frequency, similar to forced+optical libration in the decoupled spin problem. The excited mode of libration has a different frequency that depends on the shape of the secondary. This libration mode is similar to free libration in the decoupled spin problem. By exploring a range of initial conditions,

we can minimize the excited-mode librations so that its amplitude is close $0°$, leaving the secondary librating in the relaxed mode. The relaxed mode disappears only when the system is in an equilibrium state, i.e., when the mutual orbit is circular and the long axis of the secondary always points towards the primary.

For systems in which the exchange of angular momentum in the system is small, the coupled spin-orbit problem approaches the decoupled problem and the relaxed-mode and excited-mode librations become similar to the forced+optical and free librations, respectively. Because most of our simulations include some amount of spin-orbit coupling, we use the relaxed/excited mode terminology as opposed to the free/forced mode terminology of the decoupled problem.

3.5 Effect of Spin-Orbit Coupling on Libration

In this section, we study the effects of spin-orbit coupling on the relaxed-mode libration amplitude of the secondary. Under the assumptions of a fixed orbit around a spherical or point-mass primary, the amplitudes of forced+optical librations (ψ_A) in the decoupled case can be estimated with (e.g., Tiscareno et al., 2009):

$$\psi_A = \frac{2e}{\omega_0^2 - 1}, \tag{3.5}$$

where e is the eccentricity of the mutual orbit and $\omega_0 = \sqrt{3(B-A)/C}$ is the natural frequency of libration of the satellite normalized by the mean motion (n) of the mutual orbit. In the coupled problem, the amplitude of the librations depends on the primary-to-secondary mass ratio, which we quantify with our fully coupled spin and orbit integrator.

Figure 3.3 shows results of simulations in which we vary the primary-secondary mass ratio for a binary system based on NEA 1991 VH (row 2 of Table 3.1, nominal mass ratio ≈ 12). We vary the density of the secondary while keeping other shape parameters constant, and we use initial conditions that make the excited-mode libration amplitude $\sim 0°$. The corresponding analytical estimates (equation (3.5)) yield $\psi_A = 37.2°$ for $\omega_0 = 1.07$ and
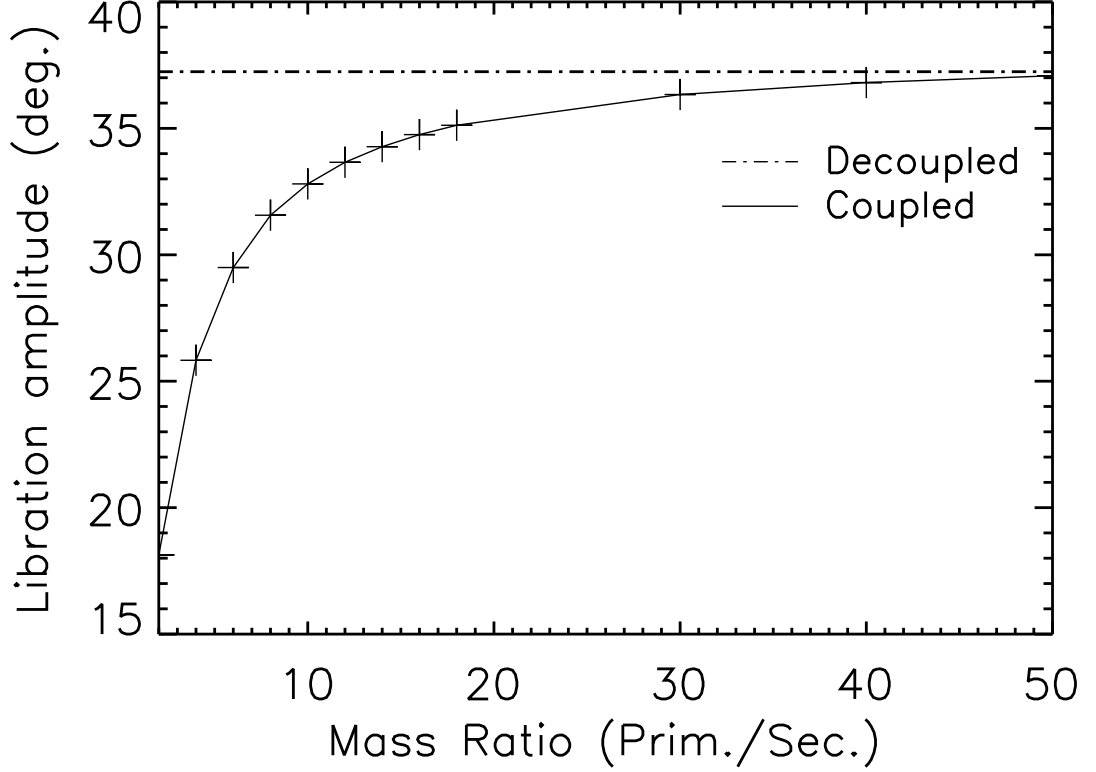
80

Figure 3.3: Influence of spin-orbit coupling on relaxed-mode libration amplitude. Plus symbols (connected by a solid line) show amplitudes of relaxed-mode libration as a function of primary-to-secondary mass ratio. Dot-dashed line shows corresponding analytical estimates of forced+optical libration computed using equation (3.5). System parameters for this simulation are based on asteroid 1991 VH and are given in the second row of Table 3.1. The elongation of the secondary, $a/b = 1.5$, corresponds to $\omega_0 = 1.07$.

$e = 0.05$. At low values of the primary-to-secondary mass ratio, the libration amplitudes are considerably smaller than the analytical estimate, suggesting that spin-orbit coupling tends to damp libration amplitudes.

3.6 Surface of Section

It is useful to visualize the dynamics with surface of section plots similar to those in Wisdom et al. (1984). At every pericenter passage of the secondary, we plot the angle between the long axis and the line of apsides of the mutual orbit, θ_p, against its time derivative, $\dot{\theta}_p$,

81

normalized by the mean motion, n. In order to identify pericenter passage, we use Keplerian elements to describe the osculating mutual orbit at each time step. These elements vary on timescales shorter than the orbital period because the orbit is not Keplerian.

It is easy to differentiate between regular and chaotic trajectories on surface of section plots: regular trajectories fall on smooth curves, whereas chaotic trajectories fill up an area of the phase space over successive visits (Wisdom et al., 1984). Figure 3.4 shows different types of trajectories of a slightly elongated secondary in this phase space. The system parameters for this plot are based on radar-derived estimates for near-Earth asteroid (NEA) 1991 VH (Margot et al., 2008; Naidu et al., 2012) and are given in row 3 of Table 3.1. The plot looks symmetric about $\theta_p = 90°$ because we use triaxial ellipsoids for the simulations, so $\theta_p = 0°$ is equivalent to $\theta_p = 180°$. Seven trajectories with different initial conditions are shown in this figure. Throughout a simulation, the secondary remains on the trajectory it started on. The red and green trajectories are regular quasi-periodic, whereas the blue trajectories are chaotic.

On a resonant (red color) trajectory, the secondary librates in a spin-orbit resonance region. For the red trajectory surrounding $\dot{\theta}_p/n = 1.5$, the secondary spins three times for every two orbits, so it is in a 3:2 spin-orbit resonance. Mercury is the only known object in a 3:2 spin-orbit resonance. For the red trajectory surrounding $\dot{\theta}_p/n = 1$, the secondary is in a 1:1 spin-orbit resonance, i.e., it spins synchronously (e.g., the Earth's moon). Similar trajectories with islands centered exclusively on $\theta_p = 0°$ and $\theta_p = 180°$ exist near half-integer values of $\dot{\theta}_p/n$ (2, 2.5, 3, etc.). The horizontal extent of the trajectory around $\theta_p = 0°$ gives the amplitude of excited-mode libration (equivalent to free libration in the decoupled spin problem). For example, on the red trajectory in the 1:1 resonance region, the secondary has an excited mode libration amplitude of $\sim 37°$. A trajectory with only relaxed-mode libration plots as a point on the y-axis, which we call the *center* of the resonance region (not shown in the figure). The relaxed-mode libration is not detectable in the horizontal dimension of the surface of section plots because we sample the spin state of the secondary at pericenter, where the relaxed-mode libration is always at 0° phase. However, the relaxed-mode libration is detectable in the vertical dimension of the surface of section plots because it contributes to

82

the angular velocity of the secondary at pericenter. The centers of the resonance regions are displaced vertically from their nominal positions in the absence of relaxed-mode libration. These offsets can be seen clearly for relaxed-mode librations with larger amplitudes (Figures 3.7 and 3.8). They are strictly due to torques on the permanent deformation of the satellite and are unrelated to the tidally induced pseudo-synchronous rotation described by, e.g., Ferraz-Mello (2013) for nearly spherical satellites on eccentric orbits.

A chaotic (blue color) trajectory marks the boundary of a resonance region and is called a separatrix. On a separatrix the secondary explores the entire range of θ_p values and the trajectory fills up a region of phase space, indicating that the trajectory is chaotic.

Secondary spin rates that are further away from the resonance regions put the secondary on a trajectory similar to one of the non-resonant quasi-periodic (green) trajectories. On these trajectories the secondary is not in a spin-orbit resonance and circulates through all θ_p values in a quasi-periodic manner. These trajectories are called quasi-periodic because they exhibit at least one non-commensurate frequency in addition to the frequency at which the motion is sampled.

Wisdom et al. (1984) assumed that the secondary spin is decoupled from the mutual orbit, a reasonable assumption for the Saturn-Hyperion system because Hyperion has negligible angular momentum compared to the mutual orbit. Under this approximation, they derive the half-widths of the resonance regions (equation (3.6), in units of the mean motion) and of the chaotic separatrix surrounding the 1:1 spin-orbit resonance (equation (3.7), in the energy domain):

$$\frac{1}{2}RW = \omega_0\sqrt{|H(p,e)|};\tag{3.6}$$

$$\frac{1}{2}SW = \frac{\Delta E}{E_0} \approx \frac{14\pi e}{\omega_0^3}e^{-(\pi/2\omega_0)}.\tag{3.7}$$

Here, H are functions tabulated in Cayley (1861) and p is the spin-orbit resonance ratio, e.g., $p = 3/2$ for a 3:2 spin-orbit resonance. ΔE represents energy variations on the chaotic
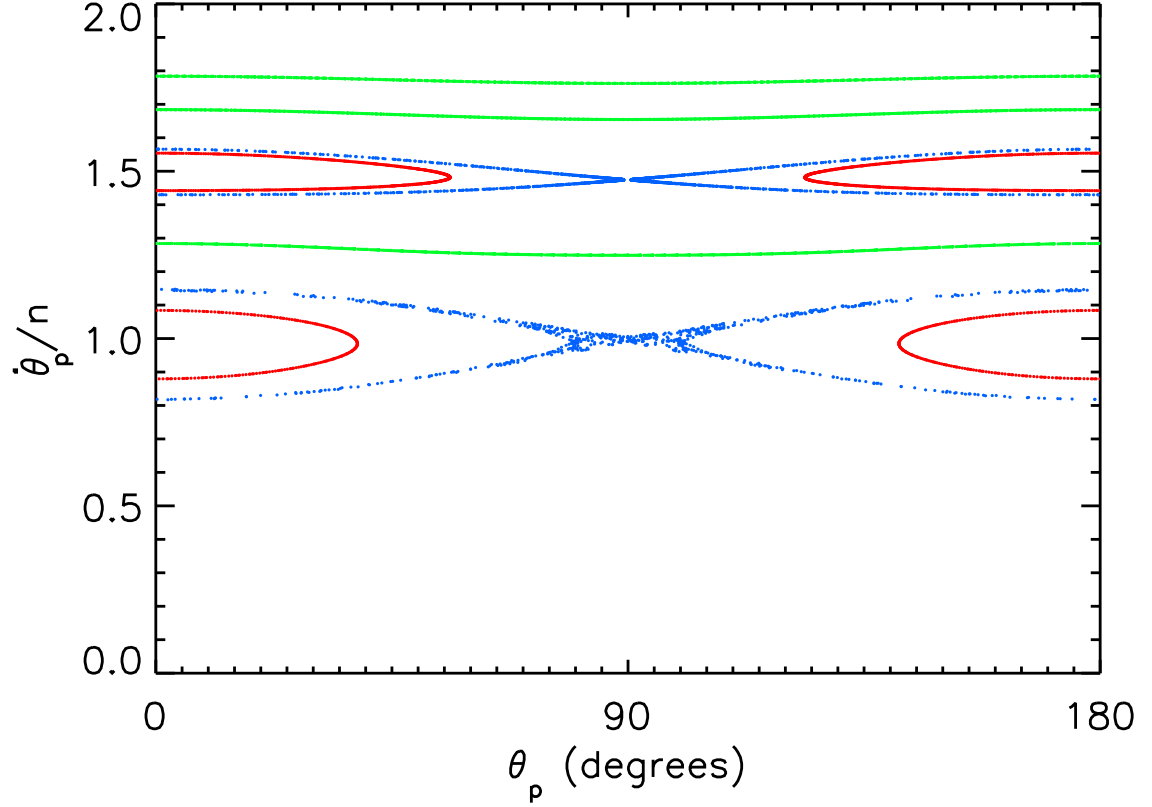
Figure 3.4: Surface of section plot for a secondary elongation $a/b = 1.01$, corresponding to $\omega_0 = 0.17$, and mutual orbit eccentricity $e = 0.05$. Other system parameters are listed in Table 3.1. Seven trajectories with initial $\dot{\theta}_p/n$ values of 1.08, 1.15, 1.28, 1.55, 1.57, 1.68, and 1.78 are plotted. Initial θ_p values are 0 in all cases. Red, blue, and green colors indicate resonant, chaotic, and non-resonant quasi-periodic trajectories, respectively.

separatrix and E_0 comes from the first integral of the averaged equation of motion of libration (Wisdom et al., 1984). It is the energy at which the libration angle begins to circulate:

$$E_0 = \frac{1}{4}n^2\omega_0^2 C, \tag{3.8}$$

where C is the moment of inertia about the spin axis. In the averaged equation of motion, the higher frequency terms that give rise to chaos are ignored, so the separatrix is regular.

The width of the resonance and of the chaotic regions grow larger with ω_0 and e. For large enough values, neighboring resonance regions overlap, resulting in a large chaotic zone surrounding the overlapping resonances. The resonance overlap criterion for the 1:1 and 3:2 spin-orbit resonances is given by (Wisdom et al., 1984):

$$\omega_0^{RO} = \frac{1}{2 + \sqrt{14e}}. \tag{3.9}$$

Overlap occurs when $\omega_0 > \omega_0^{RO}$.

These equations were derived under the assumption that the secondary spin has no feedback on the mutual orbit, and we investigate whether the analytical formulation (equation (3.9)) matches the results of our coupled integrator. For a system based on 1991 VH (Table 3.1), we varied the elongation in steps of 0.01 and determined when resonance overlap occurred. We find that it does not occur for $a/b = 1.03$ ($\omega_0 = 0.30$) but that it does occur for $a/b \geq 1.04$ ($\omega_0 \geq 0.34$). The analytical estimate, which does not take the width of the separatrix into account, places the onset of chaos at $\omega_0^{RO} = 0.35$ for $e = 0.05$. The small difference between the analytical and numerical estimates for the onset of chaos suggests that equation (3.9) provides a reasonable approximation even in the presence of spin-orbit coupling. In subsequent sections, we will confirm this finding by providing values for both estimates for a variety of orbital eccentricities. Note that Wisdom et al. (1984) also observed a small difference between analytical and numerical estimates, even in the fully decoupled case. To illustrate resonance overlap, we generate a surface of section for a value of $a/b = 1.06$ and $e = 0.05$ such that $\omega_0 = 0.42 > \omega_0^{RO} = 0.35$ (Figure 3.5). The overlap wipes out the

non-resonant quasi-periodic trajectories between the overlapping resonances and results in smaller 1:1 and 3:2 spin-orbit resonance regions and a large chaotic zone surrounding the resonances.

Substituting $e = 0$ in equation (3.9) yields $\omega_0^{RO} = 0.5$ which corresponds to $a/b \approx 1.09$. This value is low compared to typical elongations observed in asteroids (e.g., Hudson and Ostro, 1995; Hudson et al., 2000; Naidu et al., 2013). The secondary of 1999 KW4 has an elongation of 1.3 (Ostro et al., 2006). This suggests that resonance overlaps are quite likely to happen in binary near-Earth asteroids. However, for small eccentricities the width of the chaotic separatrix remains small as dictated by equation (3.7), so resonance overlaps do not result in large chaotic regions. The resonance overlap threshold of a/b as a function of e (equation (3.9)) and the width of the chaotic separatrix ($\Delta E/E_0$) as a function of e and a/b (equation (3.7)) are plotted in Figure 3.6. The figure illustrates that the size of the chaotic zone increases with eccentricity.

In the next section, we examine the surface of section plots for well-characterized binary and triple systems.

3.7   Well-Characterized binary and triple NEA Systems

We simulate the spins and orbits of well-characterized binaries and triples listed in Fang and Margot (2012a), which includes both *synchronous* ($\langle \dot{\theta}/n \rangle = 1$) and *asynchronous* ($\langle \dot{\theta}/n \rangle \neq 1$) systems, where $\langle . \rangle$ indicates values averaged over one orbit. We use our integrator to determine the minimum elongation at which resonance overlap occurs and, for synchronous satellites, the amplitude of relaxed-mode libration. We also plot surfaces of section for each system to examine the variety of dynamical regimes. When satellite elongations are not known, we assume a value of 1.3, which corresponds to that of the 1999 KW4 satellite. Equivalent radii for the components and mutual orbital parameters are obtained from Fang and Margot (2012a), unless otherwise indicated.

In all cases, we assume the primaries to be spherical and the secondaries to be triaxial ellipsoids. We need a prescription for choosing the axial dimensions such that they conform
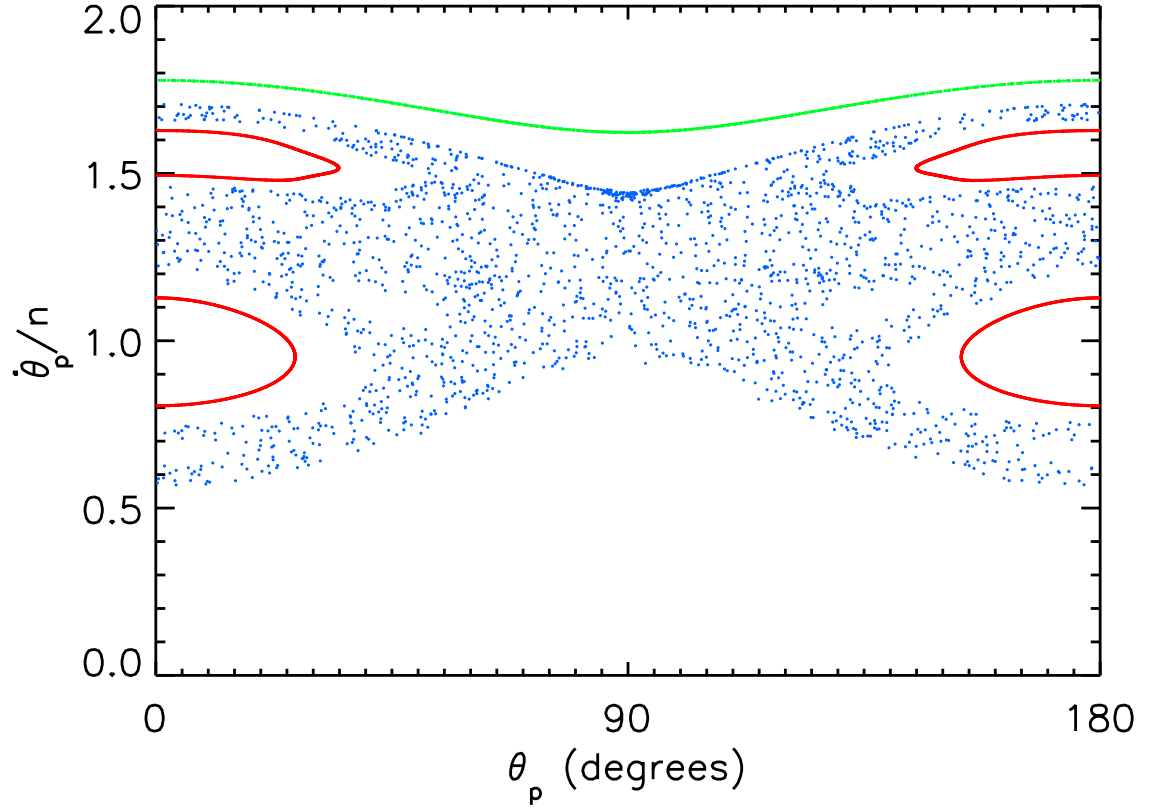
86

Figure 3.5: Surface of section plot illustrating the partial overlap of the 1:1 and 3:2 spin-orbit resonances for a secondary elongation $a/b = 1.06$, corresponding to $\omega_0 = 0.42$, and a mutual orbit eccentricity $e = 0.05$. Other system parameters are given in Table 3.1. Four trajectories with initial $\dot{\theta}_p/n$ values of 1.13, 1.63, 1.70, and 1.78 are plotted. Initial θ_p values are 0 in all cases. Color scheme as in Figure 3.4.
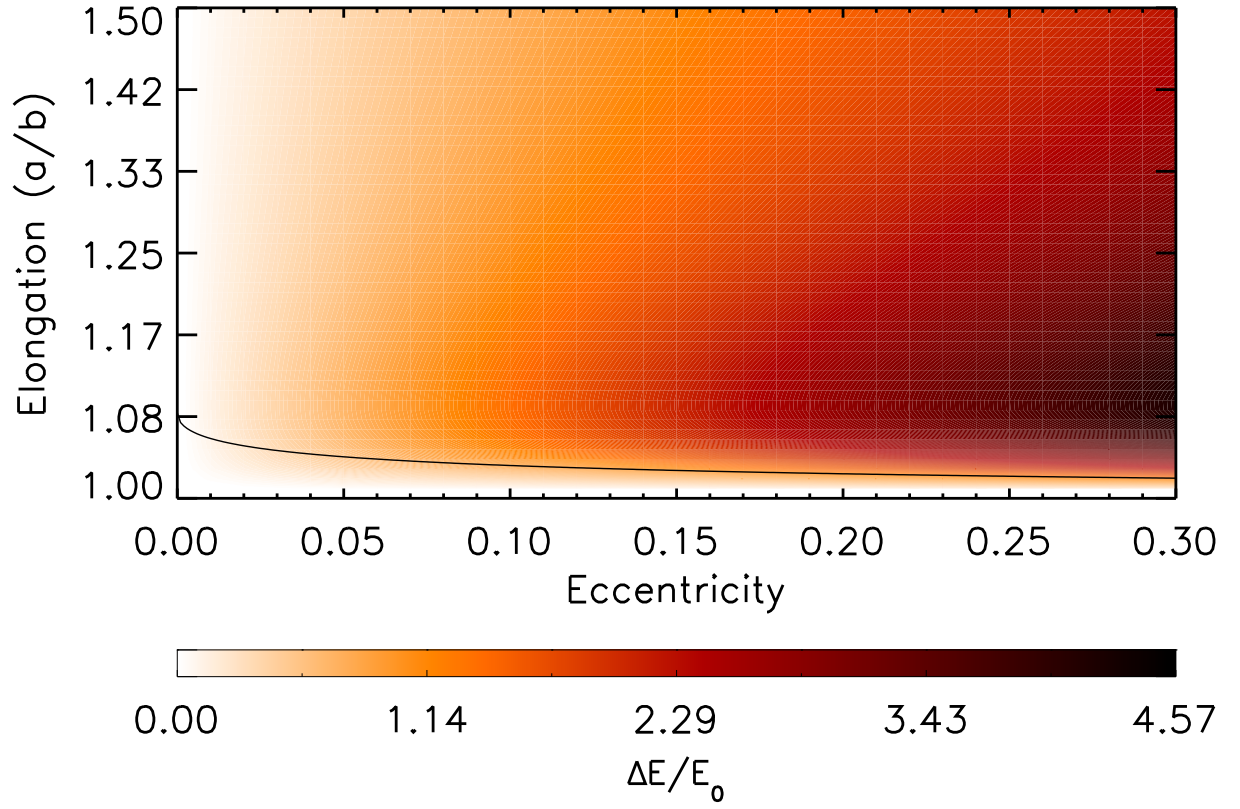
Figure 3.6: Contour plot showing the half-width of the chaotic separatrix $\Delta E/E_0$ as a function of a/b and e (equation (3.7)). According to the resonance overlap criterion of equation (3.9), overlap will occur in systems that lie above the solid line.

to the radius and mass of the secondary described in the literature. a and b are chosen to satisfy two conditions: 1) $a \times b = R_s^2$, where R_s is the radius of the secondary, and 2) a/b equals the desired elongation. c is chosen in a way that ensures $A < B < C$. The choice of c is not crucial because the dynamics are mostly sensitive to the value of $\omega_0 = \sqrt{3(B-A)/C}$ which, for a triaxial ellipsoid, is equal to $\sqrt{3(a^2 - b^2)/(a^2 + b^2)}$). The adopted density of the satellite is based on the observed mass of the satellite and on the volume of the triaxial ellipsoid. Because the choice of c is arbitrary, the densities used in the simulations are not identical to the nominal densities, but the masses used in the simulations do conform to the nominal masses. We verified the robustness of our results by running simulations with up to 20% changes in the values of c and found no appreciable difference in the surface of section plots.

3.7.1 1991 VH

As mentioned in section 3.6, the overlap of the 1:1 and 3:2 spin-orbit resonances of the 1991 VH secondary happens for $a/b > 1.04$. Radar images show that its equatorial elongation is about 1.5 (Naidu et al., 2012). Figure 3.7 shows a surface of section plot for $e = 0.05$ and $a/b = 1.5$ (other parameters are listed in Table 3.1). At these values, the chaotic zone completely wipes out the 3:2 spin-orbit resonance but a large stable 1:1 spin-orbit resonance region still exists. The center of the sychronous region (as defined in section 3.6) is on the y-axis in Figure 3.7, in the region bounded by the smaller red trajectory close to $\dot{\theta}_p/n = 0.5$. It is shifted down from $\dot{\theta}_p/n = 1$ due to relaxed-mode libration which makes a non-zero contribution to $\dot{\theta}$ at pericenter. We measure the relaxed-mode libration amplitude at the resonance center to be about 35°.

The synchronous region is surrounded by a chaotic zone. This has implications for synchronous capture that are discussed in section 3.8. If the secondary gets captured in the synchronous region, tides are expected to damp the excited-mode libration of the secondary, driving its trajectory towards the center of the synchronous region, where it exhibits only relaxed-mode libration. Since the spin is coupled to the orbit, energy removed from the

89

secondary spin will gradually change the orbit, the surface of section map, and the relaxed-mode libration amplitude and frequency. Throughout this evolution, the secondary remains in the same dynamical regime close to the center of the synchronous region. The next higher order stable resonance is the 2:1 resonance, however probability of capture into this resonance is low ($\sim 10^{-3}$ using equation 5.110 of Murray and Dermott (1999)). Similar to the synchronous region, the 2:1 resonance region is shifted vertically from $\dot{\theta}_p/n = 2$. The shift in this case is upwards because the instantaneous satellite spin rate at pericenter is greater than its orbit-averaged value of $2n$.

Preliminary measurements of the Doppler extents (or bandwidths) of the secondary in radar images (Margot et al., 2008; Naidu et al., 2012) are consistent with chaotic behavior, but because of the large amplitude libration at the resonance center and corresponding spin rate variations (Section 3.8.2), we cannot entirely rule out the possibility of synchronous spin.

3.7.2   2003 YT1

This system's component sizes are $R_p \approx 550$ m and $R_s \approx 105$ m, so the primary is similar to that of 1991 VH but the secondary is a few times smaller. The orbit ($a/R_p \sim 7$) is somewhat wider than that of 1991 VH ($a/R_p \sim 5.5$), and it is also more eccentric ($e = 0.18$ vs. $e = 0.05$). The smaller secondary and wider mutual orbit mean that spin and orbit are less coupled in this system than in 1991 VH. Substituting $e = 0.18$ in equation (3.9), we get a theoretical threshold for resonance overlap $\omega_0^{RO} = 0.30$, which corresponds to $a/b = 1.03$. Using our simulations we find that the resonance overlap threshold lies between $\omega_0 = 0.24$ ($a/b = 1.02$) and $\omega_0 = 0.30$ ($a/b = 1.03$). The elongation of the satellite is unknown. For our simulations (Figure 3.8), we chose an elongation of 1.3.

The 1:1 spin-orbit resonance region is not as prominent in this plot as it is in Figure 3.7 due to the higher eccentricity. Despite the higher eccentricity, the y-axis location of the synchronous region center is similar to that of 1991 VH, because of the smaller satellite elongation. The chaotic region is much bigger than that of 1991 VH and extends to $\dot{\theta}_p/n \approx 3$.
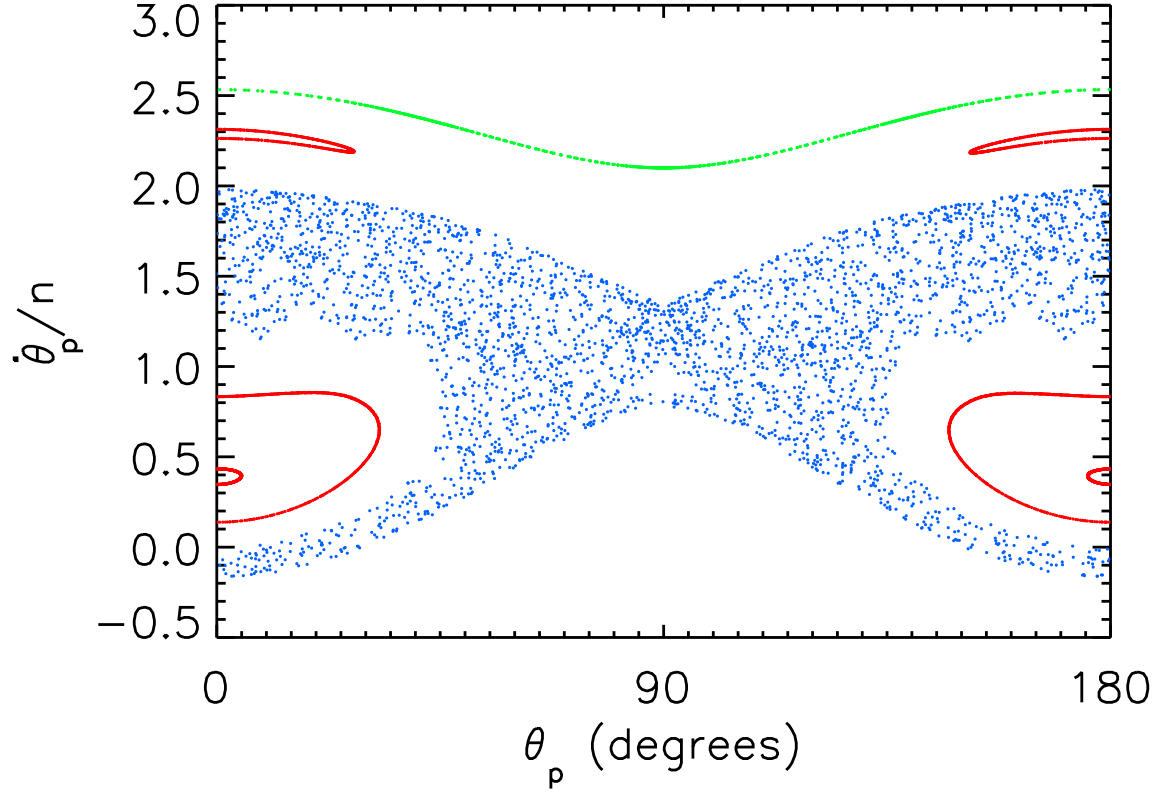
Figure 3.7: Surface of section plot for the 1991 VH secondary using the radar-derived secondary elongation $a/b = 1.5$, corresponding to $\omega_0 = 1.07$, and the mutual orbit eccentricity $e = 0.05$. Other system parameters are given in Table 3.1. Five trajectories with initial $\dot{\theta}_p/n$ values of 0.43, 0.83, 1.63, 2.31, and 2.53 are plotted. Initial θ_p values are 0 in all cases. Color scheme is the same as in figure 3.4.
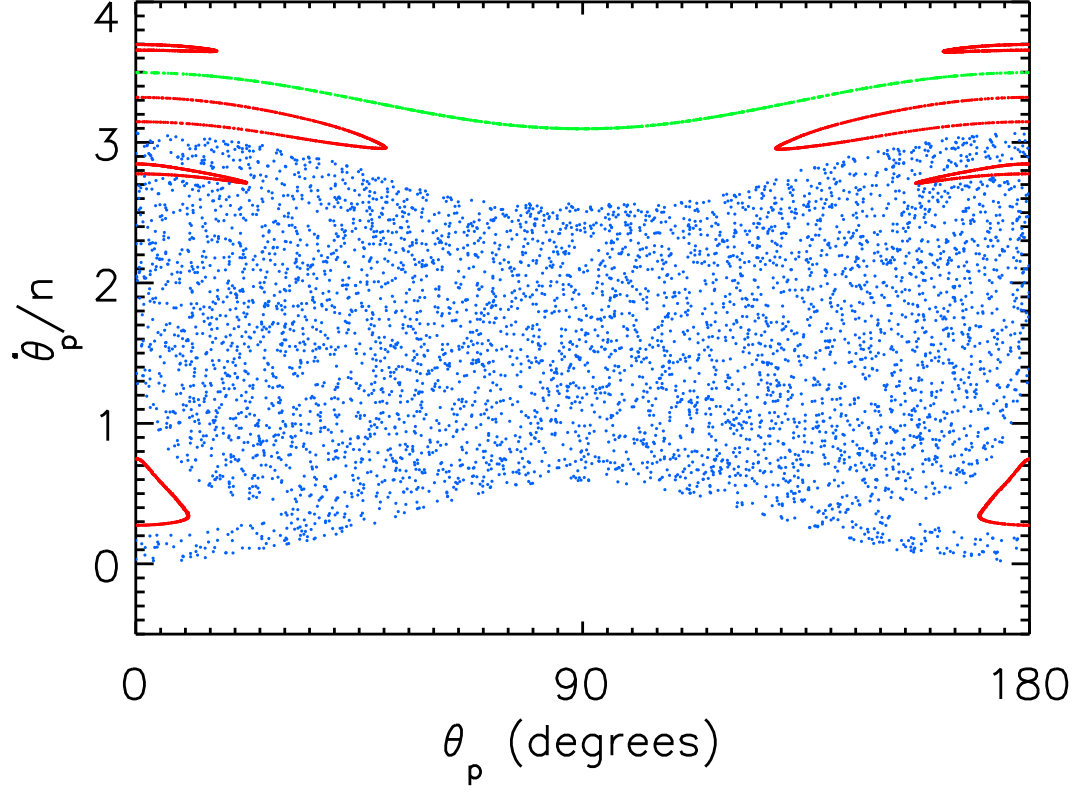
Figure 3.8: Surface of section plot for the 2003 YT1 secondary assuming the secondary elongation $a/b = 1.3$, corresponding to $\omega_0 = 0.88$, and the mutual orbit eccentricity $e = 0.18$. Other system parameters are given in Table 3.1. Six trajectories with initial $\dot{\theta}_p/n$ values of 0.75, 1.29, 2.85, 3.15, 3.5, and 3.69 are plotted. Initial θ_p values are 0 in all cases. Color scheme is the same as in Figure 3.4.

The first higher order stable resonance is the 5:2 spin-orbit resonance. This resonance region is shifted upwards from $\dot{\theta}_p/n = 2.5$, similar to the upward shift of the 2:1 resonance region of 1991 VH. The amplitude of the relaxed-mode libration measured at the center of the synchronous region is about 45°.

3.7.3 2004 DC

2004 DC has the smallest primary ($R_p \approx 180$ m), secondary ($R_s \approx 30$ m), and mutual orbit semimajor axis (750 m) in our sample, but it has the most eccentric mutual orbit ($e \approx 0.3$) (Table 3.1). The resonance overlap criterion (equation 3.9) gives $\omega_0^{RO} = 0.25$,
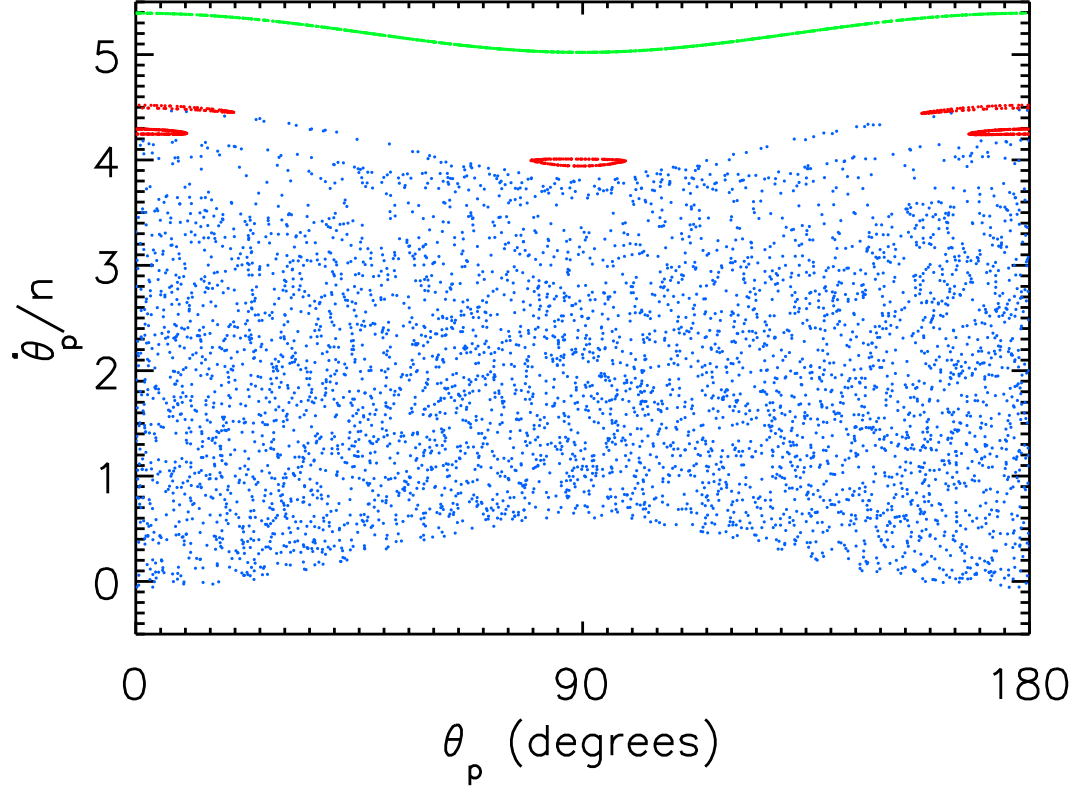
Figure 3.9: Surface of section plot for the 2004 DC secondary assuming the secondary elongation $a/b = 1.3$, corresponding to $\omega_0 = 0.88$, and the mutual orbit eccentricity $e = 0.3$. Other system parameters are given in Table 3.1. Four trajectories with initial $\dot{\theta}_p/n$ values of 1.39, 4.29, 4.49, and 5.39 are plotted. Initial θ_p values are 0 in all cases. Color scheme is the same as in Figure 3.4.

which corresponds to an elongation of $a/b = 1.02$. Using our simulations we find that the resonance overlap threshold lies between $a/b = 1.01$ ($\omega_0 = 0.17$) and 1.02 ($\omega_0 = 0.24$), roughly consistent with the analytical estimate. The shape of the secondary is not known, however its appearance in the radar images suggest that $a/b \leq 1.3$ (Patrick Taylor, personal communication). Figure 3.9 shows the surface of section plot for a secondary having an elongation of 1.3 (system parameters in Table 3.1). The chaotic region is so large that even the 1:1 resonance region disappears and the lowest-order stable resonance region is the 4:1 spin-orbit resonance. In fact the synchronous island is absent for all values of satellite elongations ≥ 1.1.

3.7.4 Synchronous Satellites

Radar data show that the satellites of 2000 DP107, 2002 CE26, 2001 SN263 (Gamma), 1999 KW4, and 1994 CC (Beta) are synchronous (Margot et al., 2002; Shepard et al., 2006; Nolan et al., 2008; Ostro et al., 2006; Brozović et al., 2011, respectively). Didymos may also be synchronous (Benner et al., 2010); for our purposes we assume that it is. We use radar-derived mutual orbital parameters, component radii, and component masses for simulating these systems. These parameters are given in Table 3.1. For satellites whose elongations are not well known, we perform simulations using a/b=1.01, 1.05, 1.1, 1.2, and 1.3. Each simulation is performed with initial conditions that put the trajectory at the center of the synchronous island. We identify the center of the synchronous island by varying the values of initial $\dot{\theta}$ until the horizontal extent of the trajectory on the surface of section becomes ∼0. As mentioned in section 3.7.1, the excited-mode libration amplitude is zero at the center of the synchronous island, which is what is expected for a tidally evolved satellite. In this case, the satellite exhibits only the relaxed-mode libration, which we measure as the angle between the long axis of the secondary and the line joining the primary and secondary centers of masses (In the decoupled terminology, this is the optical+forced libration). The libration amplitudes, i.e., the maximum values of the libration angles, are plotted as a function of elongation in Figure 3.10. The analytical estimates of the libration amplitudes, assuming the decoupled spin-orbit problem, are given by equation (3.5).

Since shape and spin state modeling are tied to each other (e.g., Ostro et al., 2006; Naidu et al., 2013), calculations such as those shown in Figure 3.10 are useful for shape modeling of asteroid satellites. These estimates are also useful for modeling binary YORP torques (Ćuk and Burns, 2005) on synchronous satellites. If a system exhibits excited-mode libration in addition to the relaxed-mode libration, the two librations will add up and create a beating pattern. Because the amplitudes and frequencies of excited-mode libration can span a wide range of values, 3D reconstruction and binary YORP modeling of dynamically excited satellites is complicated.
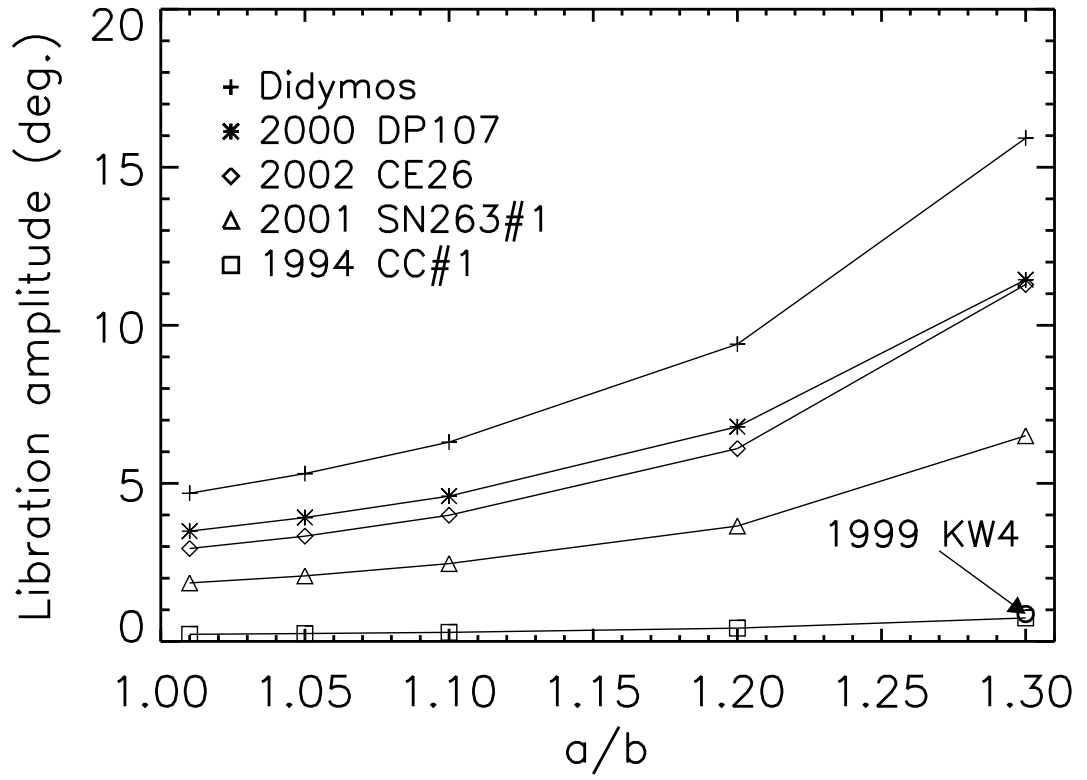
94

Figure 3.10: Numerical estimates of relaxed-mode libration amplitude as a function of satellite elongation for synchronous satellites among well-characterized binary and triple systems. For 1999 KW4, we plot a single point corresponding to the known elongation of the satellite.

3.8 Implications

3.8.1 Presence of chaotic regions and synchronous capture

In section 3.7, we showed that resonance overlap is likely to occur for asynchronous satellites in our sample and that large chaotic zones are expected in their phase spaces. This behavior can be expected in other, similar systems. Let us consider the evolution of a satellite formed with a high initial spin rate such that its trajectory in phase space is in or above the chaotic zone, the situation expected for most satellites in the formation model of Jacobson and Scheeres (2011). It is possible for YORP to increase the spin rate of the satellite, but we focus on the spin-down evolution under the influence of tidal and YORP forces. Satellites that start above the chaotic region will most likely encounter the chaotic zone on their way to the 1:1 spin-orbit resonance region. In the chaotic zone, the satellite is acted upon by tides, YORP, and torques on its permanent shape, which cause the chaotic spin. Since the spin of the satellite is coupled to the mutual orbit, angular momentum removed or added to the secondary spin by tides and YORP will also affect the mutual orbit and cause the surface of section map of the secondary to vary. However, for binary NEAs, the angular momentum of the mutual orbit is much greater than that of the secondary spin, so the effect is expected to be small. We neglect this effect for the following discussion and assume the surface of section map to be roughly constant during the evolution of the secondary spin in the chaotic zone.

If the chaotic separatrix around the 1:1 spin-orbit resonance region is extremely thin, as is the case for satellites having almost spherical shapes, then the torques on the permanent shape will be small, allowing tides or YORP to easily drive the satellite spin across the separatrix and into the synchronous region. For satellites having larger chaotic zones, like the asynchronous satellites in section 3.7, tides or YORP cannot simply sweep the satellite across the chaotic region because torques on the permanent shape can increase as well as decrease the spin rate of the satellite in a random manner. The synchronous capture process is essentially stochastic in nature. For capture to occur, the satellite has to spend enough time near the boundary of the synchronous region for tides or YORP to torque the satellite

96

into resonance. Such a process was discussed by Wisdom et al. (1984). The details of this capture process are not known and are difficult to model, however the probability of this happening will depend on the relative magnitude of $\Delta E/E_0$ compared to the energy dissipated due to tides ($\delta E_{\rm tides}/E_0$) or YORP ($\delta E_{\rm YORP}/E_0$).

Simulations and equation 3.7 show that values of chaotic spin energy variations ($\Delta E/E_0$) for the asynchronous satellites are within an order of magnitude of 1. We estimate the magnitude of tidal dissipation in one orbit using the following equation from Murray and Dermott (1999):

$$\delta E_{\rm tides} = \pi \frac{3}{2} \frac{k_2}{Q} \frac{n^4}{G} R_s^5. \tag{3.10}$$

Here k_2 is the love number, Q is the tidal dissipation factor, n is the mean motion, G is the gravitational constant, and R_s is the radius of the secondary. We approximate energy dissipation due to YORP in one orbit by multiplying the YORP torque given in Steinberg and Sari (2011) by the satellite rotation over one orbit, 4π assuming 2 satellite rotations per orbit:

$$\delta E_{\rm YORP} = \frac{2\pi R_s^3 L_\odot f_Y}{3cd^2\sqrt{1-e_\odot^2}}. \tag{3.11}$$

Here $L_\odot$ is the solar luminosity, f_Y is the YORP torque efficiency, c is the speed of light, d and $e_\odot$ are the semimajor axis and eccentricity of the heliocentric orbit, respectively. In order to compare the tidal and YORP energy dissipation with $\Delta E/E_0$, we normalize $\delta E_{\rm tides}$ and $\delta E_{\rm YORP}$ using E_0 from equation 3.8.

For computing $\delta E_{\rm tides}$ we assume $Q = 100$ and estimate k_2 values using three different models. In the rubble pile model of Goldreich and Sari (2009), $k_2 = 10^{-5}R_s$, where R_s is in km. Using the system parameters from Table 3.1, we determine $\delta E_{\rm tides}/E_0$ for all the asynchronous satellites to be between 10^{-9} and 10^{-8}. Assuming the monolith model of Goldreich and Sari (2009) for the secondary yields lower values of $\delta E_{\rm tides}$ because a monolith is more rigid than a rubble pile of the same size and has a lower value of k_2. **?** derived a different relation between love number and radius, $k_2 = 2.5 \times 10^{-5}R_s^{-1}$, by assuming that orbits of observed synchronous asteroid satellites are in an equilibrium state such that tidal torques balance binary YORP torques. Subsituting k_2 values from this relation in

equation (3.10) yields $\delta E_{\text{tides}}/E_0$ between 10^{-7} and 10^{-5}. We compute δE_{YORP} by assuming $f_y = 5 \times 10^{-4}$, the estimated value for asteroid YORP (Taylor et al., 2007; Lowry et al., 2007). $\delta E_{\text{YORP}}/E_0$ values for 1991 VH, 2003 YT1, and 2004 DC are 5×10^{-7}, 3×10^{-6}, and 2×10^{-5}, respectively.

Unknown values of Q, k_2, and f_y introduce uncertainties of a few orders of magnitude in δE_{tides} and δE_{YORP} but these energy dissipation values are several orders of magnitudes smaller than $\Delta E/E_0$, suggesting that chaotic variations in energy dominate tidal and YORP dissipations in these systems. This may substantially delay spin synchronization and, therefore, BYORP-type evolution.

If the timescale for synchronous capture is long, then tides may damp the mutual orbit eccentricity significantly before spin synchronization. This will reduce the size of the chaotic zone as dictated by equation 3.7 and make it easier for tides or YORP to torque the secondary into the synchronous region. Tidal damping of eccentricity is not a very effective process and timescales may be quite long. Fang and Margot (2012a) estimated timescales in the range 10^7 to 10^{10} years for the asynchronous satellites, but these may be in error because the underlying formalism by ? assumes synchronous rotators. It is likely that energy dissipates faster in the case of satellites that are torqued and tidally deformed in a chaotic manner, but the nature and characteristic timescale of the eccentricity evolution remain poorly known. Complicating the picture is the fact that other mechanisms such as solar perturbations (Scheeres et al., 2006) or planetary flybys (Farinella, 1992; Fang and Margot, 2012b) may also be effective at damping or exciting eccentricities. Although there is uncertainty related to the eccentricity-damping timescale, BYORP-type evolution cannot take place until the spin period is synchronized to the orbital period. Asteroid binaries may enjoy extended lives because their chaotically spinning secondaries prevent BYORP evolution.

3.8.2 Interpretation of observational data

Our results have implications for radar and lightcurve data interpretation. In radar observations (images and spectra), the Doppler extent (or bandwidth) of an object is proportional to

its apparent, instantaneous spin rate (inversely proportional to its spin period). Lightcurves show variations in the object's brightness as it spins. If the object is spinning at a constant rate, the brightness variations will be approximately periodic. The primary periodicity in the lightcurve (e.g., Pravec et al., 2006) is often used as a proxy for the object's spin rate, even though the signal is affected by changes in relative positions between the Sun, the object, and the observer. We showed in section 3.7 that asteroid satellite spin rates can be time-variable. When the lightcurve data are of sufficient quality and when $R_s/R_p \gtrsim 0.2$, it is sometimes possible to distinguish the signal of the secondary from that of the primary. In radar data, where the secondary is typically easily detectable, the spinning satellite will exhibit approximately periodic bandwidth variations. However, in both cases, a variable spin rate severely complicates the analysis. Understanding the time-varying nature of the satellite spin is important when analyzing radar and lightcurve data.

Figure 3.11 shows spin rate as a function of time for four trajectories of 1991 VH. The top panel shows a trajectory at the center of the synchronous island. Even though it would plot as a point on a surface of section, the satellite spin rate exhibits a large oscillation at the orbital rate with an amplitude slightly greater than the mean motion, n. As mentioned in section 3.6, this oscillation is the relaxed-mode libration of the satellite.

The second panel in Figure 3.11 shows a chaotic trajectory. The spin rate variations span a similar, but slightly larger, range of values than that in the synchronous case. If observations (radar or photometric) were sparse, it would be difficult or even impossible to ascertain whether a trajectory was periodic or chaotic. With a sufficient number of data points sampled at a sufficiently fast cadence, one could examine the distribution of spin rate values to identify the type of trajectory, as the distributions for resonant and chaotic trajectories are different. Spin rate variations on the synchronous trajectory resemble a sinusoid, so the distribution of spin rates looks approximately bimodal. The spin rate distribution of the satellite in the chaotic region cannot be generalized and depends on specific system parameters.

The third and fourth panels show the 3:2 resonant trajectory (red) and the quasi-periodic (green) trajectory of Figure 3.7, respectively. In these cases, the variations are much smaller
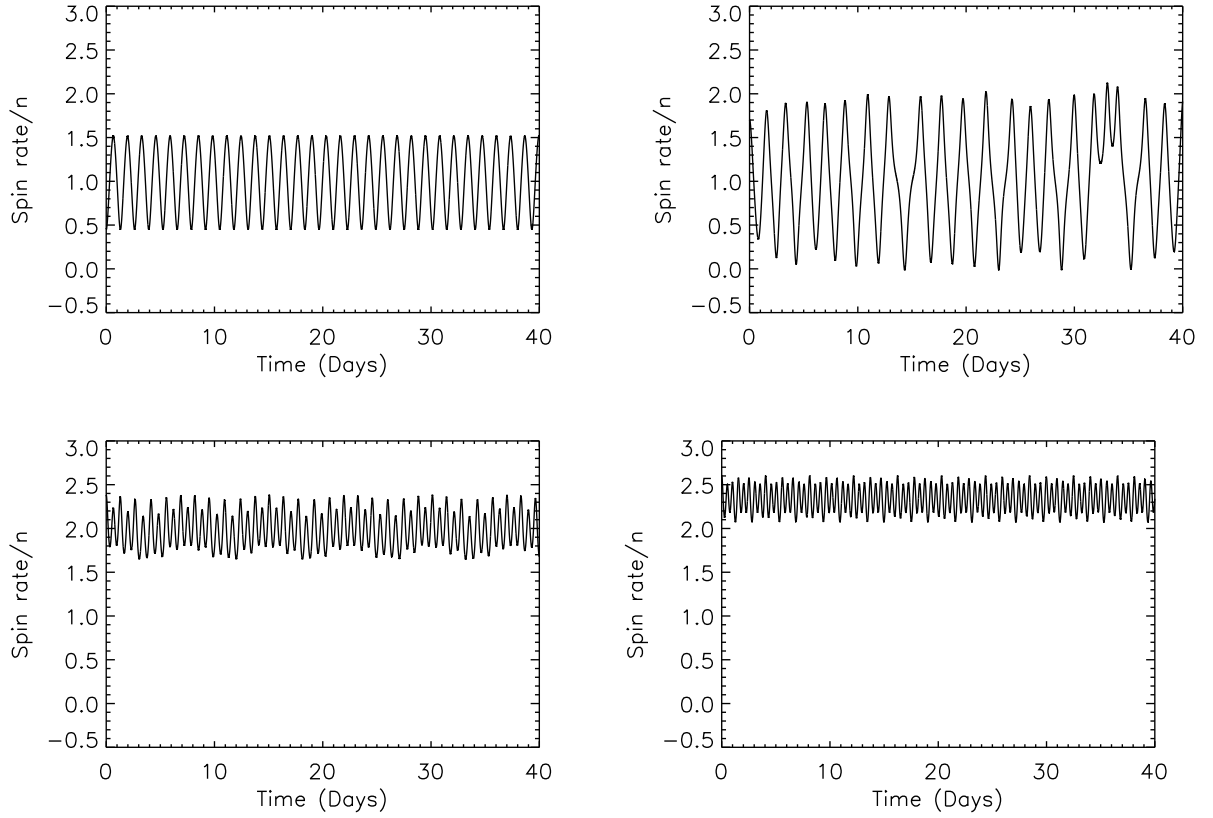
Figure 3.11: Satellite spin rate variations for 4 possible trajectories of 1991 VH. From top to bottom, the initial values of satellite spin rate, normalized by n, are 0.45, 1.70, 2.38,2.60.

than the previous two trajectories. These rotational regimes are easier to identify because large-scale chaotic variations are not present.

In radar data analysis, modeling the spin state and shape of objects are tied to each other (e.g., Ostro et al., 2006; Naidu et al., 2013). Incorrect spin state assumptions may yield incorrect shape models. Our results indicate that in some cases it will be impossible to identify the spin state of the satellite, whereas in other cases an appropriate rotational model will provide a good fit to the data. A simple model of uniform rotation may not be sufficient, as libration amplitudes can cause displacements that exceed the image resolution. We recommend using a model that includes librations for the 3D reconstruction of asteroid satellites with even moderate eccentricity and elongation.

3.9 Conclusions

We examined the rotational regimes of asteroid satellites using surfaces of section. The trajectories can be broadly classified as resonant, non-resonant quasi-periodic, and chaotic. In order to identify the specific type of spin behavior, a dense time sampling of the satellite spin state is necessary (section 3.8.2), however such datasets are seldom available. Even densely sampled lightcurves, for instance, do not yield measurements of the instantaneous spin state due to the necessity of observing ∼1 full period to estimate the spin period. In section 3.8.2, we showed that even synchronous satellites can undergo large variations in spin rates, potentially masquerading as asynchronous satellites. Careful analysis of the data along with coupled spin-orbit simulations can be used to correctly identify the spin behavior. Identifying the spin configurations is essential for obtaining accurate physical models of the satellites.

The spin configurations of satellites play a crucial role in the secular evolution of binary/triple systems under the influence of forces such as tides and binary YORP. For example, the binary YORP torque acts only on satellites whose spin periods are integer multiples of their orbital periods (Ćuk and Burns, 2005) and some estimates suggest that this torque could disrupt binary systems in just a few tens of thousands of years (Ćuk and Nesvorný, 2010; McMahon and Scheeres, 2010). Thus understanding the process of spin synchronization is essential for understanding the evolution of binaries. In section 3.8.1, we showed that satellites may have significantly longer spin synchronization timescales than those estimated by considering tidal and/or YORP forces only. This would increase the fraction of asynchronous binaries in the observed population beyond what one would expect on the basis of tidal despinning timescales. The corresponding delay in the onset of binary YORP implies that the lifetimes of binary asteroids can be significantly longer than the few tens of thousands of years suggested by binary YORP models.

3.10 Future Work

We examined the results of spin-orbit coupling in the planar case. However, Wisdom et al. (1984), using 3D simulations, showed that seemingly stable configurations in planar simulations can be attitude unstable. Future work will involve studying inclined/oblique binary systems in order to test the attitude stability of satellites in various regions of phase space. Our integrator can also be used for studying the secular evolution of binary asteroids. This will require implemention of radiation pressure and tidal forces.

Acknowledgments

Bibliography

J. Ashenberg. Mutual gravitational potential and torque of solid bodies via inertia integrals. *Celestial Mechanics and Dynamical Astronomy*, 99:149–159, October 2007. doi: 10.1007/s10569-007-9092-7.

L. A. M. Benner, J. Margot, M. C. Nolan, J. D. Giorgini, M. Brozovic, D. J. Scheeres, C. Magri, and S. J. Ostro. Radar Imaging and a Physical Model of Binary Asteroid 65803 Didymos. In *AAS/Division for Planetary Sciences Meeting Abstracts #42*, volume 42 of *Bulletin of the American Astronomical Society*, page 1056, October 2010.

G. Boué and J. Laskar. Spin axis evolution of two interacting bodies. *Icarus*, 201:750–767, June 2009. doi: 10.1016/j.icarus.2009.02.001.

M. Brozović, L. A. M. Benner, P. A. Taylor, M. C. Nolan, E. S. Howell, C. Magri, D. J. Scheeres, J. D. Giorgini, J. T. Pollock, P. Pravec, A. Galád, J. Fang, J.-L. Margot, M. W. Busch, M. K. Shepard, D. E. Reichart, K. M. Ivarsen, J. B. Haislip, A. P. LaCluyze, J. Jao, M. A. Slade, K. J. Lawrence, and M. D. Hicks. Radar and optical observations and physical modeling of triple near-Earth Asteroid (136617) 1994 CC. *Icarus*, 216:241–256, November 2011. doi: 10.1016/j.icarus.2011.09.002.

J. R. Cash and Alan H. Karp. A variable order runge-kutta method for initial value problems with rapidly varying right-hand sides. *ACM Trans. Math. Softw.*, 16 (3):201–222, September 1990. ISSN 0098-3500. doi: 10.1145/79505.79507. URL `http://doi.acm.org/10.1145/79505.79507`.

A. Cayley. Tables of the Developments of Functions in the Theory of Elliptic Motion. *MmRAS*, 29:191, 1861.

M. Ćuk and J. A. Burns. Effects of thermal radiation on the dynamics of binary NEAs. *Icarus*, 176:418–431, August 2005. doi: 10.1016/j.icarus.2005.02.001.

M. Ćuk and D. Nesvorný. Orbital evolution of small binary asteroids. *Icarus*, 207:732–743, June 2010. doi: 10.1016/j.icarus.2009.12.005.

E. G. Fahnestock and D. J. Scheeres. Simulation of the full two rigid body problem using polyhedral mutual potential and potential derivatives approach. *Celestial Mechanics and Dynamical Astronomy*, 96:317–339, November 2006. doi: 10.1007/s10569-006-9045-6.

E. G. Fahnestock and D. J. Scheeres. Simulation and analysis of the dynamics of binary near-Earth Asteroid (66391) 1999 KW4. *Icarus*, 194:410–435, April 2008. doi: 10.1016/j.icarus.2007.11.007.

J. Fang and J.-L. Margot. Near-Earth Binaries and Triples: Origin and Evolution of Spin-Orbital Properties. *AJ*, 143:24, January 2012a. doi: 10.1088/0004-6256/143/1/24.

J. Fang and J. L. Margot. Binary Asteroid Encounters with Terrestrial Planets: Timescales and Effects. *AJ*, 143:25, 2012b.

P. Farinella. Evolution of earth-crossing binary asteroids due to gravitational encounters with the earth. *Icarus*, 96:284–+, 1992.

S. Ferraz-Mello. Tidal synchronization of close-in satellites and exoplanets. A rheophysical approach. *Celestial Mechanics and Dynamical Astronomy*, 116:109–140, 2013.

P. Goldreich and R. Sari. Tidal Evolution of Rubble Piles. *ApJ*, 691:54–60, January 2009. doi: 10.1088/0004-637X/691/1/54.

R. S. Hudson and S. J. Ostro. Shape and Non-Principal Axis Spin State of Asteroid 4179 Toutatis. *Science*, 270:84–86, October 1995. doi: 10.1126/science.270.5233.84.

R. S. Hudson, S. J. Ostro, R. F. Jurgens, K. D. Rosema, J. D. Giorgini, R. Winkler, R. Rose, D. Choate, R. A. Cormier, C. R. Franck, R. Frye, D. Howard, D. Kelley, R. Littlefair, M. A. Slade, L. A. M. Benner, M. L. Thomas, D. L. Mitchell, P. W. Chodas, D. K. Yeomans, D. J. Scheeres, P. Palmer, A. Zaitsev, Y. Koyama, A. Nakamura, A. W. Harris, and M. N. Meshkov. Radar Observations and Physical Model of Asteroid 6489 Golevka. *Icarus*, 148:37–51, November 2000. doi: 10.1006/icar.2000.6483.

S. A. Jacobson and D. J. Scheeres. Dynamics of rotationally fissioned asteroids: Source of observed small asteroid systems. *Icarus*, 214:161–178, July 2011. doi: 10.1016/j.icarus.2011.04.009.

S. A. Jacobson, D. J. Scheeres, and J. McMahon. Formation of the Wide Asynchronous Binary Asteroid Population. *ApJ*, 780:60, January 2014. doi: 10.1088/0004-637X/780/1/60.

S. C. Lowry, A. Fitzsimmons, P. Pravec, D. Vokrouhlický, H. Boehnhardt, P. A. Taylor, J.-L. Margot, A. Galád, M. Irwin, J. Irwin, and P. Kusnirák. Direct Detection of the Asteroidal YORP Effect. *Science*, 316:272–, April 2007. doi: 10.1126/science.1139040.

A. J. Maciejewski. Reduction, Relative Equilibria and Potential in the Two Rigid Bodies Problem. *Celestial Mechanics and Dynamical Astronomy*, 63:1–28, March 1995. doi: 10.1007/BF00691912.

J. L. Margot, M. C. Nolan, L. A. M. Benner, S. J. Ostro, R. F. Jurgens, J. D. Giorgini, M. A. Slade, and D. B. Campbell. Binary Asteroids in the Near-Earth Object Population. *Science*, 296:1445–1448, May 2002. doi: 10.1126/science.1072094.

J.-L. Margot, P. A. Taylor, M. C. Nolan, E. S. Howell, S. J. Ostro, L. A. M. Benner, J. D. Giorgini, C. Magri, and L. M. Carter. Detailed Characterization Of Asteroid (35107) 1991 VH. In *AAS/Division for Planetary Sciences Meeting Abstracts #40*, volume 40 of *Bulletin of the American Astronomical Society*, page 433, September 2008.

J. McMahon and D. Scheeres. Detailed prediction for the BYORP effect on binary near-Earth Asteroid (66391) 1999 KW4 and implications for the binary population. *Icarus*, 209:494–509, October 2010. doi: 10.1016/j.icarus.2010.05.016.

J. W. McMahon and D. J. Scheeres. Dynamic limits on planar libration-orbit coupling around an oblate primary. *Celestial Mechanics and Dynamical Astronomy*, 115:365–396, April 2013. doi: 10.1007/s10569-012-9469-0.

C.D. Murray and S.F. Dermott. *Solar System Dynamics*. Cambridge University Press, 1999. ISBN 9780521572958. URL `http://books.google.co.uk/books?id=NY9iQgAACAAJ`.

S. P. Naidu, J. L. Margot, M. W. Busch, P. A. Taylor, M. C. Nolan, E. S. Howell, J. D. Giorgini, L. A. M. Benner, M. Brozovic, and C. Magri. Dynamics of Binary Near-Earth Asteroid System (35107) 1991 VH. In *AAS/Division of Dynamical Astronomy Meeting*, volume 43 of *AAS/Division of Dynamical Astronomy Meeting*, page 07.07, May 2012.

S. P. Naidu, J.-L. Margot, M. W. Busch, P. A. Taylor, M. C. Nolan, M. Brozovic, L. A. M. Benner, J. D. Giorgini, and C. Magri. Radar imaging and physical characterization of near-Earth Asteroid (162421) 2000 ET70. *Icarus*, 226:323–335, September 2013. doi: 10.1016/j.icarus.2013.05.025.

M. C. Nolan, E. S. Howell, T. M. Becker, C. Magri, J. D. Giorgini, and J. L. Margot. Arecibo Radar Observations of 2001 SN$_{263}$: A Near-Earth Triple Asteroid System. In *AAS/Division for Planetary Sciences Meeting Abstracts #40*, volume 40 of *Bulletin of the American Astronomical Society*, page 432, September 2008.

S. J. Ostro, J.-L. Margot, L. A. M. Benner, J. D. Giorgini, D. J. Scheeres, E. G. Fahnestock, S. B. Broschart, J. Bellerose, M. C. Nolan, C. Magri, P. Pravec, P. Scheirich, R. Rose, R. F. Jurgens, E. M. De Jong, and S. Suzuki. Radar Imaging of Binary Near-Earth Asteroid (66391) 1999 KW4. *Science*, 314:1276–1280, November 2006. doi: 10.1126/science.1133622.

P. Pravec, M. Wolf, and L. Šarounová. How many binaries are there among the near-Earth asteroids? In J. Svoren, E. M. Pittich, and H. Rickman, editors, *IAU Colloq. 173: Evolution and Source Regions of Asteroids and Comets*, page 159, 1999.

P. Pravec, P. Scheirich, P. Kušnirák, L. Šarounová, S. Mottola, G. Hahn, P. Brown, G. Esquerdo, N. Kaiser, Z. Krzeminski, D. P. Pray, B. D. Warner, A. W. Harris, M. C. Nolan, E. S. Howell, L. A. M. Benner, J.-L. Margot, A. Galád, W. Holliday, M. D. Hicks, Y. N. Krugly, D. Tholen, R. Whiteley, F. Marchis, D. R. DeGraff, A. Grauer, S. Larson, F. P. Velichko, W. R. Cooney, R. Stephens, J. Zhu, K. Kirsch, R. Dyvig, L. Snyder, V. Reddy, S. Moore, Š. Gajdoš, J. Világi, G. Masi, D. Higgins, G. Funkhouser, B. Knight, S. Slivan, R. Behrend, M. Grenon, G. Burki, R. Roy, C. Demeautis, D. Matter, N. Waelchli,

Y. Revaz, A. Klotz, M. Rieugné, P. Thierry, V. Cotrez, L. Brunetto, and G. Kober. Photometric survey of binary near-Earth asteroids. *Icarus*, 181:63–93, March 2006. doi: 10.1016/j.icarus.2005.10.014.

William H. Press, Saul A. Teukolsky, William T. Vetterling, and Brian P. Flannery. *Numerical Recipes in C (2Nd Ed.): The Art of Scientific Computing*. Cambridge University Press, New York, NY, USA, 1992. ISBN 0-521-43108-5.

D. P. Rubincam. Radiative Spin-up and Spin-down of Small Asteroids. *Icarus*, 148:2–11, November 2000. doi: 10.1006/icar.2000.6485.

D. J. Scheeres, E. G. Fahnestock, S. J. Ostro, J.-L. Margot, L. A. M. Benner, S. B. Broschart, J. Bellerose, J. D. Giorgini, M. C. Nolan, C. Magri, P. Pravec, P. Scheirich, R. Rose, R. F. Jurgens, E. M. De Jong, and S. Suzuki. Dynamical Configuration of Binary Near-Earth Asteroid (66391) 1999 KW4. *Science*, 314:1280–1283, November 2006. doi: 10.1126/science.1133599.

M. K. Shepard, J.-L. Margot, C. Magri, M. C. Nolan, J. Schlieder, B. Estes, S. J. Bus, E. L. Volquardsen, A. S. Rivkin, L. A. M. Benner, J. D. Giorgini, S. J. Ostro, and M. W. Busch. Radar and infrared observations of binary near-Earth Asteroid 2002 CE26. *Icarus*, 184: 198–210, September 2006. doi: 10.1016/j.icarus.2006.04.019.

E. Steinberg and R. Sari. Binary YORP Effect and Evolution of Binary Asteroids. *AJ*, 141: 55, February 2011. doi: 10.1088/0004-6256/141/2/55.

P. A. Taylor, J.-L. Margot, D. Vokrouhlický, D. J. Scheeres, P. Pravec, S. C. Lowry, A. Fitzsimmons, M. C. Nolan, S. J. Ostro, L. A. M. Benner, J. D. Giorgini, and C. Magri. Spin Rate of Asteroid (54509) 2000 PH5 Increasing Due to the YORP Effect. *Science*, 316:274–, April 2007. doi: 10.1126/science.1139038.

M. S. Tiscareno, P. C. Thomas, and J. A. Burns. The rotation of Janus and Epimetheus. *Icarus*, 204:254–261, November 2009. doi: 10.1016/j.icarus.2009.06.023.

J. Wisdom, S. J. Peale, and F. Mignard. The chaotic rotation of Hyperion. *Icarus*, 58: 137–152, May 1984. doi: 10.1016/0019-1035(84)90032-0.